University of Kentucky
UKnowledge

Theses and Dissertations--Civil Engineering | Civil Engineering

2013

TWO-DIMENSIONAL HYDRODYNAMIC MODELING OF TWO-PHASE FLOW FOR UNDERSTANDING GEYSER PHENOMENA IN URBAN STORMWATER SYSTEM

Zhiyu S. Shao
University of Kentucky, zshao2@g.uky.edu

Recommended Citation
Shao, Zhiyu S., "TWO-DIMENSIONAL HYDRODYNAMIC MODELING OF TWO-PHASE FLOW FOR UNDERSTANDING GEYSER PHENOMENA IN URBAN STORMWATER SYSTEM" (2013). *Theses and Dissertations--Civil Engineering*. 5.
http://uknowledge.uky.edu/ce_etds/5

This Doctoral Dissertation is brought to you for free and open access by the Civil Engineering at UKnowledge. It has been accepted for inclusion in Theses and Dissertations--Civil Engineering by an authorized administrator of UKnowledge. For more information, please contact UKnowledge@lsv.uky.edu.

www.manaraa.com

STUDENT AGREEMENT:

I represent that my thesis or dissertation and abstract are my original work. Proper attribution has been given to all outside sources. I understand that I am solely responsible for obtaining any needed copyright permissions. I have obtained and attached hereto needed written permission statements(s) from the owner(s) of each third-party copyrighted matter to be included in my work, allowing electronic distribution (if such use is not permitted by the fair use doctrine).

I hereby grant to The University of Kentucky and its agents the non-exclusive license to archive and make accessible my work in whole or in part in all forms of media, now or hereafter known. I agree that the document mentioned above may be made available immediately for worldwide access unless a preapproved embargo applies.

I retain all other ownership rights to the copyright of my work. I also retain the right to use in future works (such as articles or books) all or part of my work. I understand that I am free to register the copyright to my work.

REVIEW, APPROVAL AND ACCEPTANCE

The document mentioned above has been reviewed and accepted by the student's advisor, on behalf of the advisory committee, and by the Director of Graduate Studies (DGS), on behalf of the program; we verify that this is the final, approved version of the student's dissertation including all changes required by the advisory committee. The undersigned agree to abide by the statements above.

Zhiyu S. Shao, Student

Dr. Scott A. Yost, Major Professor

Dr. Kamyar C. Mahboub, Director of Graduate Studies

www.manaraa.com

TWO-DIMENSIONAL HYDRODYNAMIC MODELING OF TWO-PHASE FLOW FOR UNDERSTANDING GEYSER PHENOMENA IN URBAN STORMWATER SYSTEM

DISSERTATION

A dissertation submitted in partial fulfillment of the
requirements for the degree of Doctor of Philosophy in the
College of Engineering
at the University of Kentucky

By

Zhiyu Shannon Shao
Lexington, Kentucky
Director: Dr. Scott A. Yost, Associate Professor of
Civil Engineering
Lexington, Kentucky

2013
Copyright © Zhiyu Shannon Shao 2013

www.manaraa.com

ABSTRACT OF DISSERTATION

TWO-DIMENSIONAL HYDRODYNAMIC MODELING OF TWO-PHASE FLOW FOR UNDERSTANDING GEYSER PHENOMENA IN URBAN STORMWATER SYSTEM

During intense rain events a stormwater system can fill rapidly and undergo a transition from open channel flow to pressurized flow. This transition can create large discrete pockets of trapped air in the system. These pockets are pressurized in the horizontal reaches of the system and then are released through vertical vents. In extreme cases, the transition and release of air pockets can create a geyser feature.

The current models are inadequate for simulating mixed flows with complicated air-water interactions, such as geysers. Additionally, the simulation of air escaping in the vertical dropshaft is greatly simplified, or completely ignored, in the existing models.

In this work a two-phase numerical model solving the Navier-Stokes equations is developed to investigate the key factors that form geysers. A projection method is used to solve the Navier-Stokes Equation. An advanced two-phase flow model, Volume of Fluid (VOF), is implemented in the Navier-Stokes solver to capture and advance the interface.

This model has been validated with standard two-phase flow test problems that involve significant interface topology changes, air entrainment and violent free surface motion. The results demonstrate the capability of handling complicated two-phase interactions. The numerical results are compared with experimental data and theoretical solutions. The comparisons consistently show satisfactory performance of the model.

The model is applied to a real stormwater system and accurately simulates the pressurization process in a horizontal channel. The two-phase model is applied to simulate air pockets rising and release motion in a vertical riser. The numerical model demonstrates the dominant factors that contribute to geyser formation, including air pocket size, pressurization of main pipe and surcharged state in the vertical riser. It captures the key dynamics of two-phase flow in the vertical riser, consistent with experimental results, suggesting that the code has an excellent potential of extending its use to practical applications.

www.manaraa.com

Key Words: mixed flow, multi-phase flow, Navier-Stokes equation, projection methods, VOF

Zhiyu S. Shao

Student's Signature

03/18/2013

Date

www.manaraa.com

TWO-DIMENSIONAL HYDRODYNAMIC MODELING OF TWO-PHASE FLOW FOR UNDERSTANDING GEYSER PHENOMENA IN URBAN STORMWATER SYSTEM

By

Zhiyu Shannon Shao

Scott A. Yost

Director of Dissertation

Kamyar C. Mahboub

Director of Graduate Studies

03/18/2013

www.manaraa.com

I would like to dedicate this dissertation to my family, especially…

my parents
and
my son, Ryan Xuanyuan Gong

www.manaraa.com

ACKNOWLEDGEMENTS

I want to express my sincere gratitude to Dr. Scott A. Yost and Dr. James M. McDonough for providing me with advice, direction and guidance in the course of pursuing this work. The directions I received from them often led to critical thoughts and motivations to further improve my work, and more importantly, correct the mistakes I have made. Dr. Yost has been an excellent academic advisor and mentor in all the years. He had never once given up on me and has been working patiently, teaching and encouraging me in every aspect of my life. Without the encouragement and friendship from Dr. Yost, this PhD work will not be possible. He is without any doubt one of the most influential people in my life.

I also thank Dr. Scott F. Bradford for the many discussions about multi-phase flows in this work. The discussions have been very beneficial and helpful. I would also like to acknowledge Dr. Tate Tsang and Dr. Jimmy Fox for their encouragements and advice during the course of this work, and their service on my committee for this dissertation.

Furthermore, I would like to thank my family members, especially my parents and my husband for their unconditional love and support. I want to thank our son, Ryan Xuanyuan, my greatest sources of joy and hope.

I would like to take this opportunity to thank my friend and colleague Tien Mun Yee for his help, encouragement and friendship.

www.manaraa.com

TABLE OF CONTENTS

www.manaraa.com

www.manaraa.com

www.manaraa.com

LIST OF TABLES

www.manaraa.com

LIST OF FIGURES

www.manaraa.com

www.manaraa.com

www.manaraa.com

NOMENCLATURE

A	Flow area
B	Body force
β	Shuman Filter parameter
c	wave speed
C_r	Courant number
D	Diameter (Distance)
D_{fs}	Free surface displacement
D^*_{fs}	Free surface displacement normalized by pressure head
f	Volume fraction
Fr	Froude number
g	Acceleration due to gravity
H	Flow height (depth)
L	Length
O	On the order of
Q	Flow rate
p	Pressure
P_{atm}	Atmosphere pressure = 1.01×10^5 pa
RE	Reynolds number
$\boldsymbol{U}$	Velocity vector
t	Time
u, v	Velocities in x and y direction of the Cartesian coordinate
$\bar{u}, \bar{v}$	Velocities (u, v) averaged horizontally
$\tilde{u}, \tilde{v}$	Velocities (u, v) averaged vertically

www.manaraa.com

V	volume
w	Surge front speed
x, y	Cartesian coordinate variables
y_{fs}^{*}	Free surface height normalized by pressure head
y_{fs}	Free surface height
$\delta x, \delta y$	Grid size in x and y direction, respectively
δt	Time step size
ϕ	Pseudo pressure
μ	Dynamic viscosity
$\tilde{\tilde{\mu}}$	Dynamic viscosity averaged at the cell vertex
ω	SOR iteration parameter Omega
ρ_g	Density of air
ρ_l	Density of liquid
$\tilde{\rho}$	Density averaged vertically
$\bar{\rho}$	Density averaged horizontally
$\tilde{\tilde{\rho}}$	Density averaged at the cell vertex
θ	angle

www.manaraa.com

ABBREVIATIONS

CFD Computational fluid dynamics

CFL Courant-Friedrichs-Lewy stability condition

FCT Flux Correct Transport

GCT Grid Convergence Test

LES Large eddy simulation

LHS Left hand side of an equation

MAC Marker-and-Cell method

MOC Method of characteristics

PLIC Piecewise Linear Interface Construction

PDE Partial differential equation

PPE Pressure Poisson equation

QUICK Quadratic Upstream Interpolation for Convective Kinematics

RHS Right hand side of an equation

SWE Shallow Water Equations

VOF Volume of fluid method

N-S Navier-Stokes equations

www.manaraa.com

CHAPTER 1 INTRODUCTION

1.1. Geyser feature

An urban stormwater collection system is designed to convey flow by gravity during design storm events. In normal gravity flow condition, a free surface is present at the top of the flow, with the pressure at the free surface atmosphere pressure. The design storms for an urban drainage system typically have a return period between 5 to 25 years. However, storms with return periods higher than the design storm result in peak flows that are higher than the design flowrate. When the peak flowrate exceeds the capacity of the stormwater system, flow can transition from gravity flow to pressurized flow, called pressurization. Due to a rapid increase of inflow, a pressure surge can form at the upstream boundary of the pipe and advances downstream. Other changes at the boundaries, such as failure of a lifting pump station, sudden closure of a downstream gate or blockage of downstream pipe section could also lead to pressurization in the system.

A stormwater system that flows under pressure, called a surcharged system, is undesirable in stormwater design and management because it creates risks (i.e., flooding, overtopping) to the stormwater infrastructures. The pressure wave and pressure fluctuation induced by the flow transition impact the integrity of pipes and joints. If the pressure head within the pipe is higher than the ground level elevation, water could overflow from the manhole and cause flooding to the adjacent areas. An additional concern is the potential public health risks as the overflow from the manhole can be a source of pollution, bacteria and other toxic substances. Under extreme conditions, flow transition could leads to a phenomenon called "geyser", characterized by a mixture of air and water shooting out of manholes.

Geyser features have been observed in several combined or separate storm sewer systems. In a paper by Guo and Song (1991), a picture shows a geyser shooting from storm water sewer in St Paul, Minnesota in 1987. He also showed a manhole cover blowout induced by a geyser in a highway storm sewer system in Minneapolis, Minnesota in 1982. Similar incidence in Hamilton, Ontario was reported by Hamam (1982) and Wang et al. (2003) where a welded manhole cover on a ten-foot trunk sewer was blown out due to pressurized flow during a major storm. Zhou

www.manaraa.com

(2002) also reported a severe surcharge in a combined sewer system during an extreme (300-year return period) storm event in Edmond, Alberta, Canada in 1995. He mentioned that the surcharged pressure was high enough in some section of the pipe to overflow from the manhole and cause flooding. Recently, CBC Canada reported that in Montreal, Canada on July 18th, 2011a powerful geyser, occurring after a flash storm, blew off a manhole and swept away a car nearby (CBC News 2011), as shown in Fig. 1.1.

Figure 1. 1 Geysers from storm sewer (Left: CBC News 2011; Right: Apittoda 2011).

1.2. Existing studies

Since the original identification of geyser features, a lot of studies have been performed in this area, including field, experimental and numerical studies, with the goal of understanding the physics behind the geyser formation. Nevertheless, it was not until very recent that some of the key factors in geyser formation were understood.

1.2.1.Experimental Study

The geyser feature is the result of several factors, and is still an on-going research topic. As flow transitions from free surface flow to pressurized flow, a surge wave starts forming and propagating along the pipe. The surge wave plays a key role in geyser formation. On one side, the surge front traps air pockets by blocking the flow area. As the front propagates along the pipe, it compresses the trapped air pocket. When the air pocket reaches a ventilation point, such as a

www.manaraa.com

manhole or a dropshaft, the air escapes from the system, accompanied by a mixture of air and water. The escape of the air causes pressure fluctuations in the system, similar to a water hammer effect. Moreover, when the surge waves reach pipe boundaries, the sudden change of pressure induces a water hammer type of pressure fluctuations.

In the past, it was believed that geysers were caused by pressure spikes generated in the pipe during a flow transition. A sudden change of velocities induce water hammer type of pressure spikes. It was believed that the pressure spikes could lift the manhole cover and "push" water out of the manhole. As a result, the early studies on geysers were focusing on capturing the pressure spikes caused by the water hammer surge wave, such as Song et al. (1983), Cardle et al. (1989), Guo and Song (1990).

In some of those early experiments, the researchers noticed that the air phase has a significant impact on the flow pattern during the flow transition process. More specifically, the escaping of air pockets in a pressurized system could cause significant instability to the flow system.

As early as the sixties, Holley (1969) noticed that the sudden release of air bubbles from a ventilation location created a temporary unsteadiness in the system and caused the pressure to fluctuate. He stated that the pressure fluctuations were further amplified into larger surges as the flow passed through the successive pipe sections. Similar patterns of pressure fluctuations created by air pocket escaping at the ventilation locations have been reported by Albertson and Andrews (1971), Yevjevich (1975), Yen (1978) and Valentin (1981). They described that the release of air pockets from a pressurized system initiates surge waves similar to water hammer surge waves.

Shulgin (1975) observed an "air shock" phenomenon in his experiments where air was present in the pipe during a flow transition. He stated that the air pockets carried along in the flow can cause hydraulic shocks. As the air pockets move along the pipe, they do not pose significant impacts on the flow conditions. It is not until the air pockets reach a boundary open to the atmosphere that they start disturbing the flow. In such a case, the escape rate of the air is much higher than the rate of the water. With the consequent pressure drop in the air pocket, the steady-state flow condition within the pipe is disturbed and becomes unstable.

Cardle et al. (1989) also reported a high frequency pressure spikes when the air was forced out by a propagating surge front. They observed high frequency pressure oscillations during a transition case, which they believed were caused by air-water interface instability and air entrainment.

www.manaraa.com

Hamam and McCorquodale (1982) studied the air-water interface instability problem and pointed out that the most severe pressure oscillations are expected at or near maximum gravity flow condition where the pipe almost flows full.

In a later flow transition study experiments performed by Li and McCorquodale (1999), the impacts of a compressed air pocket within a pressurized pipe were further investigated in details. In their experiments they compared pressure fluctuations from water hammer effects and from the release of a compressed air pocket. They noticed that the pressure oscillations caused by the water hammer tend to have higher spikes. But both cases could produce pressure spikes higher than the pipe crown. They also pointed out that once some of the air-water mixture was forced out; the pressure inside of the air pocket was reduced below a threshold pressure and did not allow further air escape. As a result, the remaining air went through another compression and release cycle until all the trapped air was expelled. Zhou et al. (2002) did further investigations on this subject. In their experiments, the size of the ventilation device varies so that the responses of the pressurized system from the air release could be compared. They noticed that when the ventilation size was small, the trapped air pocket acted as an air cushion and absorbed some pressure fluctuations. When the ventilation device size was large, a water hammer type of pressure oscillation was observed. If the orifice size was intermittent, a combination of both types of pressure oscillations was present.

Burrow (1995) performed a series analytical study on air pockets in a single pressurized pipe and concluded that the air pocket could severely magnify surge peaks during a pump shutdown, especially in a single air pocket that has a small size.

De Martino et al. (2008) also noticed high pressure surges induced by the expulsion of a trapped air pocket through an orifice at the downstream end of a pressurized pipe. The resulting pressure oscillation patterns were divided into two distinct stages including an initial phase of low-frequency pressure oscillation from the air release, and the following sudden pressure spikes from water hammer effects as the water column reaches the orifice.

From the above, it appears that the escape of these air pockets causes significant instability to the flow system. However, the trapped air was not the focus of a geyser study until very recently. In recent years, a series of experiments performed by others (Lewis 2011; Wright 2009, 2011a, 2011b; Vasconcelos 2003a, 2003b, 2005) revealed several key factors that trigger geysers including trapped air and compressed air pockets. Their studies successfully predicted several

www.manaraa.com

geyser events. They stated that the pressure fluctuations due to air compression in the stormwater pipe could be significant. These pressure fluctuations have higher magnitude than the actual pressure surge wave in a pressurization process. These pressure fluctuations also show short durations that match the observed occurrence frequency of the geysers. They also stated that the size of the vertical ventilation pipe is the predominant factor when it comes to the magnitude of the geyser. Other parameters such as the initial water depth and the initial pressure within the air pocket have less impact on the geyser magnitude. Their experiments showed that geysers occurred even when the pressure head within the pipe is below ground elevation, which is contrary to the traditional assumption regarding geysers.

1.2.2. Field Study

Wright et al. (2009) performed a field study for a geyser occurrence in Minneapolis, Minnesota. They analyzed the time series data in a stormwater tunnel at the time of the geyser event. They found that the pressure within the main pipe was not sufficient enough to push water out of vertical shaft at the time of the geyser. They concluded that it was the compressed air pockets in the stormwater system that caused the geyser event. In their study, they also observed that the release of the compressed air pocket led to a reduced pressure in the main pipe.

1.2.3. Numerical Study

From the experimental findings of geyser, it appears that flow transition is the first step in a geyser formation. The existing numerical models used to study geyser were originally developed to simulate transient flows or mixed flows. There are great interests in simulating mixed flows in the numerical modeling field. However, the numerical study of geysers lags behind the experimental and field studies. The main reason is due to the limited knowledge of the physics behind a geyser.

As mentioned in previous section, the early studies were focusing on capturing the pressure spikes induced by the flow transient. Numerical models, often referred as “mixed-flow” models, were developed to study the flow transient phenomenon in the stormwater system. Details of the difference numerical models for mixed-flows are present in Chapter 2. A mixed-flow state is such that both open channel flow and pressured flow are present in one system. The existing mixed-flow models typically solve two-dimensional Shallow Water Equation in combination with one-

www.manaraa.com

dimensional surge equations for the main pipe and a separate set of lumped–mass one-dimensional continuity and momentum equations for the vertical dropshaft or manhole.

The Shallow Water Equation is widely used in Civil Engineering area to describe open channel flows. The Shallow Water Equation is derived from the Navier-Stokes Equations by assuming no accelerations in the vertical direction, resulting in a hydrostatic pressure distribution. They are not applicable for pressurized flow. However, by defining a term "pressure wave speed", Shallow Water Equation has been used to describe pressurized flow as well. This is how pressurized flow was solved in most of the existing Shallow Water Equation based numerical models.

Problem could rise when Shallow Water Equation is applied to violent flow field. When Hieu et al. (2004) was studying wave breaking cases, he noticed that pressure distribution in the vicinity of wave breakup is significantly different than a hydrostatic distribution. This discrepancy is mainly caused by the smaller composite density due to vertical movements of water phase and the presence of air bubbles at the wave breaking areas.

Furthermore, the compressed air pocket, which is the key in geyser formation, is greatly simplified or totally ignored in the existing mixed flow numerical models.

Over time the so-called two-phase models have been developed to include dynamics of the air phase in mixed-flows. However, these models do not truly simulate both phases. The existing two-phase numerical models developed for mixed-flows typically treat the water and air phase as a rigid column with no details resolved within the column. The interaction of the two phases is often simplified by a one-dimensional lumped-mass momentum equation.

The interactions between water and air become even more complex in geysers as they are characterized by a mixture of air and water, and momentum exchange occurs constantly. The air-water interaction is crucial in a geyser simulation and should be modeled using a full two-phase flow model.

A complete review of the existing numerical models for mixed flows is presented in Chapter 2. The review shows there are significant limitations in the existing numerical models. These limitations become more prominent when it comes to simulating the complex interactions between the water and air phases in geyser events.

www.manaraa.com

To better understand the complicated two-phase interactions in the flow transitions, more effort is needed to develop a comprehensive numerical model that could capture the full dynamics in both phases.

Multiphase flow models, solving the full Navier-Stokes Equations, have been developed and widely used in mechanic engineering, manufacturing, and aerospace. However, they are rarely used in civil engineering as models based on the Shallow Water Equations are preferred. There are historical reasons for this, namely, the size of civil engineering problems often makes the computational solutions of the Navier-Stokes equations prohibitively expensive. Whereas solving the Shallow Water Equation is much cheaper. However, computing resources and technology has evolved significantly in the past two decades with the development of more powerful supercomputers and more efficient algorithms for the Navier-Stokes Equation. With the improved computing power, it is practical to develop a true two-phase model solving the full Navier-Stokes Equations to study mixed flows in stormwater system.

1.3. Motivations

This study attempts to bridge the gap between experimental studies and the existing mixed flow numerical models with trapped air effects, laying the ground for future numerical simulations of operation, mitigation and design of storm water system with complicated air-water interactions, such as geysers. This is done by developing a comprehensive two-phase numerical model that solves the Navier-Stokes Equations. This study is intended to investigate the mechanism of geysers numerically, to simulate the effects of air pockets in geyser formation, and to capture the key dynamics of the geyser features.

A key difference between this study and the other existing numerical models is that a comprehensive two-phase model based on Navier-Stokes Equations is developed. This study is important from both an engineering design prospective as well as a regulatory prospective.

A full dynamic two-phase model could also be a useful tool for stormwater system mitigation. A full dynamic model provides details of the flow in the system when it comes to predicting potential surcharges and providing guidance for future designs. Sound engineering design is to prevent surcharges and geyser features from occurring in the system because of the severe consequences. Hence, for new stormwater system design, it is crucial to evaluate the potential flow transition conditions that could lead to surcharges and/or geysers, and thus minimize the impacts in the design phase. Additionally, for existing stormwater system, if the surcharge occurs

www.manaraa.com

frequently and poses a problem, a mitigation alternative could to be developed to alleviate the surcharge conditions based on the feedbacks from a full dynamic numerical model.

1.4. Physical Scenarios

Following the recent experimental and field findings by other researchers (Lewis 2011; Vasconcelos 2003a, 2003b, 2005; Wright 2009, 2011a,2011b), the type of geysers generated by compressed air pockets through a partially-filled manhole is simulated in this work.

As the compressed air pockets escape from the manhole, they lift the water column within the manhole to above ground level and cause geysers. In this study, it was assumed that the manhole is partially filled with water prior the arrival of the compressed air pockets. However, geyser could occur even the manhole is completely dry initially and there is no air pocket escape. Vasconcelos (2005) explained that the compressed air pockets could cause a geyser by pushing the pressurization surge front, that contains a large amount of air entrainment and air bubbles, out of the manhole. However, as stated by Vasconcelos (2005), the type of geyser caused by a large air pocket escaping through a partially water-filled ventilation tower most likely has the highest strength and often causes more damages than other geysers.

Based on previous experimental, field and numerical findings, the formation of geyser due to the compressed air pocket escape could be described as follows:

i. Positive surge starts forming at the boundary due to an increased inflow or a reduced downstream capacity. The surge propagates into the free surface flow regime. Surge direction could be upstream, downstream or both depending on which side of pipe capacity is exceeded first.

ii. Air is blocked within the pipe and starts forming discrete air pockets due to interface instability effects, and/or surge waves propagation in the pipe. The traveling directions of the trapped air pockets depend on the velocity of the flow. The trapped air pockets could become compressed by the pressurization front in the pipe.

iii. When the pressure surge wave reaches the boundary, the whole pipe flows under pressure. The pressure wave reaches the boundary and then reflects back. This is

www.manaraa.com

similar to a water hammer and causes pressure fluctuations in the pipe. The air pockets are further compressed by the bouncing pressure waves.

iv. The compressed air pockets travel to ventilation locations such as a dropshaft and escape from the system. The escape of the air pockets introduces significant instability and causes more pressure fluctuations in the flow system. The escape of the air pocket is also accompanied by a lifted water column. If the air-water mixture is elevated above the ground surface elevation, it becomes a geyser.

In a geyser occurrence, the dynamics within the main pipe predominantly determines the strength of geyser. However, as indicated by previous experimental results, the release of air pocket would have an impact in the main pipe as well.

www.manaraa.com

CHAPTER 2 LITERATURE REVIEW

The formation of a geyser involves three essential components, including open channel flow regime, pressured flow regime and compressed air pockets. Therefore the numerical simulation of a geyser feature should simulate both open channel and pressured flows. Numerical models that simulate both open channel flow and pressurized flow are referred as "mixed-flow" or "transient flow" models. The term "transient" here refers to the transitions of flows with a significant velocity and pressure change, such as a surge wave or a water hammer wave. The term "mixed-flow" here simply means a mixed flow regime, namely, open channel and pressure flows.

As mentioned in Chapter 1, the existing mixed-flow models typically solve the two-dimensional Shallow Water Equation in combination with the one-dimensional surge equations for the main pipe, and a separate set of lumped–mass one-dimensional continuity and momentum equations for the vertical dropshaft. The one-dimensional surge equations are also a set of lumped–mass continuity and momentum equations. The typical solution procedure for a stormwater pipe with a dropshaft system is to first solve the mixed-flow in the pipe to obtain velocity, pressure distribution and the location of the surge front, and then solve the flows in the dropshaft using a separate set of lumped–mass continuity, momentum and energy equations. However, not all the existing mixed-flow models solve the flows in the vertical dropshaft. Even though a few numerical models do include the dropshaft in the simulation, the simulation is greatly simplified.

The existing mixed-flow numerical models typically fall into three categories: Priessmann Slot, Shock Fitting and Rigid Column methods. There are a few other studies that do fall into the general family of these methods, and will be discussed later.

The Shallow Water Equation, also known as St-Venant Equation, was derived from the Navier-Stokes Equations by assuming that there are no accelerations in the vertical direction, resulting in a hydrostatic pressure distribution in the flow. Note that there are only two variables left to be solved including the velocity and the depth for a two-dimensional free surface problem. The two-dimensional Shallow Water Equation can be written as:

$$\frac{\delta y}{\delta t} + v\frac{\delta y}{\delta x} + \frac{c^2}{g}\frac{\delta v}{\delta x} = 0 \tag{2.1}$$

$$\frac{\delta v}{\delta t} + v\frac{\delta v}{\delta x} + g\frac{\delta y}{\delta x} + g(s_f - s_0) = 0, \tag{2.2}$$

www.manaraa.com

where c represents the gravity wave speed and can be calculated from: $c = \sqrt{gA/B}$, where A is the flow area and B is the top width of the flow area.

The equations for pressured flow have a similar form as for the open channel flow. The equations for pressurized flow can be written as follows.

$$\frac{\delta y}{\delta t} + v\frac{\delta y}{\delta x} + \frac{a^2}{g}\frac{\delta v}{\delta x} = 0 \tag{2.3}$$

$$\frac{\delta v}{\delta t} + v\frac{\delta v}{\delta x} + g\frac{\delta y}{\delta x} + g\left(s_f - s_0\right) = 0 \tag{2.4}$$

where a represents the pressure wave speed and y is the piezometric head measured from the pipe invert.

The open channel equations (Eqs. 2.1 and 2.2) are non-linear partial differential equations, which are not straightforward to solve. By defining a characteristic curve, these equations could be converted into a set of ordinary differential equations, so-called characteristic form. The characteristic form of the Shallow Water Equations is

$$\frac{dy}{dt} \pm \frac{c^2}{g}\frac{dv}{dt} \pm c\left(s_f - s_0\right) = 0 \tag{2.5}$$

$$\frac{dx}{dt} = v \pm c \tag{2.6}$$

where "+" sign represents the C^+ characteristic curve and "–" is for the C^- characteristic curve. The two characteristic curves are defined by Eq. 2.6. Equations 2.5 and 2.6 are ordinary differential equations and can be solved fairly quickly. To solve this set of differential equations, an integration of time is carried out along the C^+ and C^- characteristic curves. This solution procedure is well known as the Method of characteristics (MOC).

In an analogous manner, a similar set of characteristic curves could be defined for the pressurized flow. The resulted characteristic equations for the pressurized flow have the same form as Eqs. 2.5 and 2.6, with one exception. In the pressured flow equations, the gravity wave speed c is replaced by the pressure wave speed a.

Because of the similarity of the governing equations for open channel and pressurized flows, the initial attempt of solving a mixed-flow problem is to solve one set of equations throughout the whole domain by ignoring the dynamics at the interface. However, flow transition between a free

www.manaraa.com

surface flow and a pressured flow poses numerical difficulties. Problems arise when the open channel flow transitions to a pressured flow as the top width *B* becomes to zero and leads to an infinite wave speed *c*. In such a case, the Shallow Water Equation does not hold for the pressured flows. One way to overcome this challenge is to introduce a hypothetical slot with a finite top width to represent the pressure wave speed *a*. Then the numerical algorithm for Shallow Water Equation could be carried out throughout the whole domain for both open channel and pressurized flow regimes.

2.1. Priessmann Slot Method

In the Priessmann Slot method the pressurized flow was replaced by an equivalent free surface flow by adding a hypothetic narrow slot at the top of the pipe. Priessmann and Cunge (1961) first proposed this approach for the mixed flow simulation. The width of the slot is determined in a way such that the resulted gravity wave celerity, *c*, is equal to the pressure wave celerity, *a*, for the pipe. Hence, the solution procedure could be carried out throughout the whole domain without distinguishing the flow regime. Cunge and Wegner (1964, 1980) applied the Priessmann Slot method to solve mixed flows in a closed conduit. Ji, (1998) applied this method to a stormwater network and solved the governing equations implicitly.

The mixed-flow is featured by a surge front that separates the free surface and pressured flow regimes. At the surge front, the pressure head is discontinuous; velocity and pressure vary noticeably across the surge front. The governing equations for the open channel flow and pressurized flow are partial differential equations with advection terms. They could be solved with conventional finite difference, finite element or finite volume methods. However, when these methods are implemented in advective problems with discontinuities, undesirable numerical oscillations often appear near the discontinuity. The numerical oscillations originate from discretizations that are carried out across the interface. To eliminate the unwanted numerical oscillations, shock capture schemes such as Total Variation Diminishing (TVD) (Harten 1983), Flux Predictor (Braschi and Gallati 1992) and ROE type Riemann solvers (Arora and ROE 1997) have been adopted in the Priessmann Slot method. These shock capture schemes typically use information from a predominantly upstream side to discretize the advective term.

Garcia-Navarro et al. (1994) used an implicit Total Variation Diminishing (TVD) method with the Priessmann Slot approach to treat the discontinuity. In his study, the flux crossing the

www.manaraa.com

interface was calculated based on the advection speed obtained from the eigenvalues of the equations.

Capart et al. (1997) used an upwind Pavia Flux Predictor scheme in their Priessmann Slot model. The flux across the interface was estimated from the upwind direction using the two characteristic curves at the interface.

Vasconcelos et al. (2009) used a ROE-type Riemann solver, which is a first order upwind scheme, and a finite volume method in his Priessmann Slot model. To calculate the flux across the discontinuity, a Roe average was taken across the interface to reduce the oscillations.

León et al. (2008, 2009) improved the Priessmann Slot approach by introducing a gradual transition section between the pipe and the slot so that the model could simulate a gradual interface transition in the slow inflow filling cases. They also used a second-order Godunov-type scheme with a slope limiter to handle the discontinuity.

One problem with the original Priessmann Slot approach is that it does not support negative pressure simulations. Priessmann Slot method assumes that whenever the piezometer head is below the crown of the pipe, a free surface would form. Song et al. (1983) pointed out that this assumption is not realistic because the physical pipes could support negative pressures. The formation of a free surface could only occur at a drop inlet, a surge relief or an overflow structure where a vent exists and allows air flow in. To overcome this problem, Vasconcelos (2006) made modifications to the momentum equation by implementing a two-component pressure strategy. In the two-component pressure approach, the pressure term in the Shallow Water Equation was split into two parts including a hydrostatic pressure and a pressure originated from surge. The second part is defined as pressure head change and could be calculated from the change of cross section area based on elastic wall assumption. In this way, the negative pressure could be counted as part of the computation.

The Priessmann Slot approach is simple in concepts and easy to implement to existing Shallow Water Equation based models. It predicts the increased pressure in a pressurization process in simple stormwater systems quite well. Hence this method has received wide popularity in the commercial computation software including XP-SWMM and EPA-SWMM, both having been used widely in engineering design and practices.

www.manaraa.com

The main drawback of Priessmann Slot approach is that no hydrodynamics at the interface are reflected in the simulation. Air-water interaction is either completely ignored or significantly simplified. Improvements have been made to this method so that it could include the effects of air pocket within the pipe. Arai and Yamamoto (2003) applied an approach to traditional Priessmann Slot method to simulate an air pocket trapped in the flow. However, complicated dynamics in air-water interaction, such as interface instability, air entrainment and the dynamics in a dropshaft, pose a challenge to this method.

2.2. Shock Fitting Method

Wiggert (1972) developed a different approach, called shock fitting, to handle the discontinuity in the mixed-flow problem. Unlike the shock capturing schemes, the shock fitting method is not a discretization strategy. In this method, the discontinuity is directly "tracked" and treated as an internal boundary. In this way, the two flow regimes are isolated at the discontinuity and solved separately. Individual solution procedure for the open channel flow and the pressurized flow can be implemented in each regime.

At the internal boundary there are six unknown variables, including the flow velocity and depth at both sides of the surge, surge front speed and surge location. In addition to the aforementioned governing equations for open channel flow and pressurized flow regimes (Eqs. 2.1-2.4), two additional equations could be developed for the surge front based on mass and momentum conservation. The additional equations are one-dimensional lumped-mass equation, called surge equations. In surge equations, the pressure distribution is assumed to be hydrostatic. The surge equations can be written as

$$A_1(v_1 - w) = A_2(v_2 - w) \tag{2.7}$$

$$g(A_2\bar{y}_2 - A_1\bar{y}_1) = A_1(v_1 - w)(v_1 - v_2) \tag{2.8}$$

where

w is the interface (surge front) propagation speed

$\bar{y}_1$ and $\bar{y}_2$ are the gravity centroid of flow area *1* and *2*, respectively

v_1 is the velocity of flow area *1*

www.manaraa.com

v_2 is the velocity of flow area *2*

Using these two surge equations in combination with the governing equations for the open channel and the pressured flow (Eqs. 2-3 through 2.6), the speed and height of a surge front can be solved. The location of the surge front can be determined following the solution of the surge front speed.

In the original shock fitting study by Wiggert (1972), the Method of Characteristic was used to solve the open channel flow while the pressurized flow was treated as a plug flow or a rigid column. Song (1983) modified this method by solving both free surface flow and pressure flow equation using the Method of Characteristic. Cardle and Song (1988) included a Bernoulli equation in their shock fitting method and studied the pressurization and depressurization process in mixed flows. Guo and Song (1990) applied the shock fitting method to the Tunnel and Reservoir Plan (TARP) network in Chicago. Miyashiro and Yoda (1983) studied an underground drainage system using shock fitting method.

Wang (2003) applied the shock fitting method to mixed-flow problems with trapped air pockets. He modified the momentum equation for the surge front so that it includes the pressure force from a compressed air pocket. The pressure variation within the air pocket was calculated from ideal gas law.

Musandjifuamba (2003) expanded the shock fitting methods into three levels with different complexity that could be used in a complicated system with hydrodynamic features, such as supercritical flow, hydraulic bore and rapid flow changes.

Zhang and Vairavamoorthy (2006a and 2006b) applied a method similar to a shock fitting when they studied the trapped air effects in a pressurized system. They used the shock fitting method to track the internal boundary. They divided a pipe into three lumped-parameter line segments including filling, blocking and trapped air segments instead of finite control cells. This approach, called Method of Line, is similar to a rigid column method.

In the original shock fitting method, it was assumed that an almost vertical front, similar to a moving bore, exists between the two flow regimes. However, this does not hold, especially during a gradually filling process. As shown by Vasconcelos (2005), in the smaller inflow cases, the pipe filling bore does not have a sharp vertical front. Instead, it has a long and round front with an

www.manaraa.com

almost horizontal opening present on the top of the water phase. To overcome this limitation, Politano (2007) improved the shock fitting method by calculating the angle of the surge front.

Shock-fitting models are also called fully dynamic models because it captures some of the air-water dynamics at the interface. Despite the notable improvements, this method is still unsatisfactory when it comes to simulate the interactions between water and air phases. To apply mass and momentum conservation equations at the surge front, a well-defined surge front has to be present, which is not always the case. Other key dynamic features, such as air entrainment and interface instability, cannot be simulated by this method.

An additional concern is the estimation of the pressure wave speed, which is one of the key parameters in the shock fitting method. Pressure wave speed for pure water or pure air could be easily obtained and remain constant. However, pressure wave speed for mixed air-water phases is very hard to estimate because this value is a function of the percentage of air in the mixture. Estimation of the pressure wave speed directly affects the location of surge front.

2.3. Rigid Column Method

When dealing with the effects of air trapping and air compression within the system, the aforementioned two methods seem inadequate. Rigid Column Method is often referred to as a "two-phase" model when it comes to the mixed-flow simulation. The Rigid Column Method was originally developed by Hamam and McCorquodale (1982) to capture entrapped air effects in stormwater system. In their study, they simulated a single air pocket within a pipe.

Unlike Priessmann Slot or Shock fitting method, Rigid Column Method does not solve the Shallow Water Equation or the pressured flow equations. Rigid Column Method solves a set of one-dimensional lumped-mass continuity and momentum equations in an ordinary differential equation form. In the Rigid Column Method the pipe was typically divided into three sections including two surcharged full flow sections and a partially full flow section in which an air pocket is present at the top of the water layer. The system is demonstrated in Fig. 2.1. Each section is treated as a rigid column and moves with a uniform speed. By applying mass and momentum conservation laws to each rigid column, the pressure and velocity at the interface could be calculated. Rigid Column is a one-dimensional lumped-mass method. Therefore, detailed velocity and pressure distribution along the pipe are not available.

www.manaraa.com

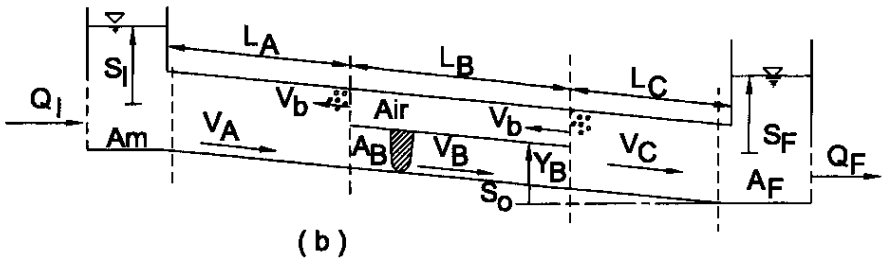

Figure 2.1 Model segments in rigid column method (Li and McCorquodale, 1999)

(with permission from ASCE, J. of Hydraulic Engineering)

In the original Rigid Column method, it was assumed that a stationary air bubble is trapped between the water columns and that the air bubble moves along with the flows. Later, the air-water interaction was modeled using Helmz instability theory by Hamam and McCorquodale (1982). Their study showed that the interface becomes unstable and significant air entrainment is involved if the relative velocity between air and water surpassed a critical threshold value.

Li and McCorquodale (1999) expanded the original Rigid Column Method to capture the movement of an air pocket trapped in a mixed flow. The air pocket is assumed moving upstream and is released at the upstream manhole once the threshold pressure is reached. By implementing mass and momentum conservation laws to the upstream and downstream manhole, their model simulated the air release scenarios in the manhole. However, the assumption in the air escape simulation is that the air pocket remains a regular shape in the rising process, which is a great simplification of the real physics.

Zhou et al. (2002) applied the rigid column method to simulate pressure fluctuations induced by the air release from a hypothetical orifice at the end of a pipe. This is a well-known hydraulic feature called “air slam” in transient flow. Zhou’s work shed some light on how the air escape impacts a pressured flow system. The numerical results indicate that a rapid release of air from a pressurized system could induce high pressure spikes. They included water hammer, orifice flow and energy equations in the model. The pressure fluctuation from the release of air pocket was described by a theoretical equation developed by Martin (1976) when he studied the pressure oscillation subject to instantaneous valve opening.

www.manaraa.com

Following Zhou's work, Liu et al. (2011) developed a rigid-plug elastic-water model based on the rigid column concept to study pressure fluctuations induced by trapped air in a filling process.

Rigid water column method is straightforward for implementation. The Rigid Column Method does have some two-phase model features as it integrates both water and air phases into the simulation. It also includes the pressure caused by compressed air pockets within the momentum equation. Hence the retardation impact from the compressed air pockets is reflected.

Despite the improvements from the Rigid Column method on capturing compressed air effects, this method is still not satisfactory for geyser simulations. It has the same shortcomings of the other two methods, namely, the simulation of the air water interactions is very limited. Simulation of dynamics within the air-phase is completely ignored in this model. Additionally, it has the same limitation as a shock fitting method as a well-defined surge front has to be present between the air and water phases.

In addition to this, rigid water column assumes the velocity within the controlled column is uniform and the release of air is unrestricted, which are questionable for violent flow, especially the film flow in the vertical dropshaft during geysers.

2.4. Other Numerical Models

Several other methods have been applied to study transient flows and the pressure fluctuation induced by compressed air in a closed pipe. de Martino et al. (2008) studied high pressure surges induced by the expulsion of a trapped air pocket through a downstream orifice. Chaiko et al. (2002) did a water hammer analysis in a pipe line with an entrapped air pocket present in the flow. Kioni (2002) studied the velocity and pressure field of a water hammer feature caused by rapid closure of a downstream valve by solving the Navier-Stokes equation.

Very few numerical models were developed for the dropshaft simulation. Existing numerical simulation in the dropshaft is one-dimensional, and greatly simplifies the air-water flow pattern. In the existing models, it is typically assumed that the air pocket is continuous and occupies the whole cross section area.

The vertical rising of a finite continuous air pocket in a stagnant water column has been studied experimentally (Davies and Taylor 1950; Batchelor 1967; Baumbach et al. 2005). Theoretical rising speeds of the air pocket have been derived based on one-dimensional mass and momentum

www.manaraa.com

equations, film flow, and slug flow theory for different types of air pockets (Davies and Taylor 1950; Batchelor 1967; Wallis 1969). The rising of a Taylor bubble in stagnant liquid in a vertical tube has been studied numerically by Bugg et al. (1998) and Bugg and Saad (2002). In their work they solved the two-dimensional Navier-Stokes equations with a Volume of Fluid two-phase model to track the rising motion of a Taylor bubble. A Piecewise Constant method was used in the interface reconstruction in their Volume of Fluid model. However, these studies are performed in still water column and not in a geyser context.

Hamam and McCorquodale (1982) included a one-dimensional lumped-mass momentum equation in their model to simulate the surface rising in a dropshaft due to increased pressures from flow transition.

Guo and Song (1991) studied the hydrodynamics in the dropshaft under transient condition. They used a Priessmann slot method to solve the transient flow in the main pipe. However, in their work, the flow in the dropshaft is a single-phase flow. The drops shaft is filled with water and there is no air pocket present. They used the one-dimensional mass and momentum equation in combination with an energy equation to describe the flow in the dropshaft. They studied the pressure fluctuations in the dropshaft induced by the minor disturbance from the main pipe by performing a Perturbation analysis.

Li and McCorquodale (1999) studied the pressure fluctuation pattern in the main pipe due to air escape at the manhole. They used a rigid column method to study the flow transition in the main pipe and treat the air pocket as a deformable control volume. They applied the one-dimensional mass and momentum equations at the two sides of the air pocket control volume and calculated the acceleration rate of the rising air pocket.

León et al. (2010) investigated the boundary conditions at junctions and drop-shafts in the mixed flow cases.

Following a similar approach by Li and McCorquodale (1999), Lewis (2011) studied the rising motion of an air pocket in the dropshaft by treating the air pocket as a deformable control volume and applying the one-dimensional mass and momentum equations. In their work, they counted the reduced water column height due to the film flow around the rising air pocket in the dropshaft. The air pocket is assumed to be continuous and has a round nose shape. They also assumed that the surrounding film flow is laminar and the flowrate could be calculated based on laminar film flow theory. The thickness of the laminar film has to be assumed when applied the film theory.

www.manaraa.com

2.5. Limitations of Existing Numerical Models

It appears that the existing numerical models might be suitable for mixed flow simulation but are not adequate to simulate the complicated dynamics found in geysers. Although several existing models included air phase and air-water interactions in the simulation, the key features present in a geyser, such as the motion of an air-water mixture in the vertical dropshaft, have not be part of any of the existing models.

The governing equations used by the existing numerical models for mixed flows are questionable, especially when they are applied to geyser simulations. The Shallow Water Equations are developed to simulate open channel flow instead of pressurized flow. Moreover, the assumptions behind the development of Shallow Water Equation do not hold in violent air-water mixed flow, especially in the proximity of entrapped air pocket boundaries, as discussed in Chapter 1. In addition to these, the common limitation shared by the existing numerical models is that they typically assume a distinct surge front to start the computation. As indicated by the work of Baines (1991), the shape of the nose and trailing edge of an air pocket are very different and often irregular in flow transitions. The accuracy of existing numerical models is limited by the simplification.

Song at al. (1983) stated that the pressurization is a dynamic shock phenomenon and should be treated with a fully dynamic model. Vasconcelos (2009) also concluded that complicated hydraulic features such as the air counter-flow could not be modeled with the existing methods.

Another major limitation of the existing models is that the simulation of air escape in the vertical dropshaft was never modeled by a fully dynamic model. Only a few attempts have been reported simulating the upward air pocket rising motion. However, they proved to be fairly primitive and greatly simplify the physics.

In the existing models for the vertical dropshaft, it is typically assumed that there is no restriction for air to move upwards in the vertical dropshaft. However, the flow in the vertical dropshaft is a complicated two-phase flow with air pocket pushing up and water flowing down around creating an upwelling motion of an air-water mixture. The shear stress between the two phases tends to slow down the air pocket movement.

Another simplification in the existing numerical models for the dropshaft is the approach used to simulate the vertical rising motion of air pockets. In the existing models, it is assumed that the air

www.manaraa.com

pocket is continuous and occupies the whole cross section area. The air pocket is typically treated as a slug flow (Hamam and McCorquodale 1982; Guo and Song 1991). As a result, the momentum equations are only applied at the top and bottom of the air pocket under the assumption that momentum exchange only occur at these two locations. However, when the air pocket breaks up and mixes with the surrounding water during the rising, the assumption is completely invalid. Momentum exchange plays an important role in the escape of the air pocket. In the geyser occurrence, water is pushed out from the manhole. The loss of resistance further accelerates the upward air motion and cause significant fluctuations in the system. This complicated flow could only be simulated by a true two-phase Navier-Stokes model.

Navier-Stokes Equation based numerical modeling of two-phase flow has gone through significant developments due to the increased computational power and advanced numerical algorithms. This allows the numerical investigation of the complex interaction between water and air phases, especially in the vertical dropshaft. Solution of the incompressible Navier-Stokes Equation with a two-phase flow model provides a fuller picture of the dynamics in the air-water mixture flow, the key mechanism in geysers.

2.6. Two-phase Flow Model Solving Navier-Stokes Equation

A two-phase flow model is often referred to as an interface model as there is an interface that distinguishes the two phases. A notable feature of this type of flow is the moving boundary, namely, the interface. Simulation of the interface flow poses to be a unique numerical problem as the exact interface shape and location are only known at the beginning of the simulation. It must be calculated as part of the solution procedure to advance the computation. Interface flow is one of the most commonly observed flows in nature, such as coastal waves, flood waves and open channel flows. Different models have been developed to simulate this type of flows.

Harlow and Welch (1965) first tackled the interface flow problem by using a Marker and Cell method (MAC). The original Marker and Cell method was introduced as an approach to decouple pressure and velocity in solving Navier-Stokes Equations for the time-dependent incompressible flow with a free surface. In the original Marker and Cell method, Lagrangian massless markers were placed in the flow field. These markers were advected with the local fluid field. By tracking the movement of those markers, the location and shape of the free surface could be determined. Since the first Marker and Cell was introduced, variations have been developed to improve the free surface calculation. Surface Marker and Cell (SMMC) was

www.manaraa.com

introduced by Chen et al. (1997). In this method, the markers were only placed along the interface to reduce the total arithmetic of tracking makers throughout the flow domain. The Marker and Cell type of two-phase models are straightforward and easy to implement. But they have great limitations when it comes to complicated interface topology changes such as interface breaking up, merging and overturning.

The introduction of Volume of Fluid (VOF) by Hirt and Nichols (1981) represented a milestone in the multiphase flow simulation field. In the Volume of Fluids method, the term "volume fraction" *f* is introduced where the volume faction is a scalar and its value varies from zero to one. The value of *f* represents the volume fraction of the heavier fluid phase. A value of zero stands for an "empty" cell and a value of one stands for a "full" cell. A value between zero and one represents an interface cell. VOF method tracks the volume fraction in each cell rather than the interface itself. For incompressible flows, fluid volume is a conservative value. A transport equation for volume fraction can be written based on volume conservation to describe the evolution of the volume. An interface can be "reconstructed" based on the discrete volume fraction values and advanced with local velocity field to a new time step.

In the original VOF, the interface reconstruction scheme was a Donor and Acceptor method, which is a "simple line interface calculation" (SLIC) method with low order of accuracy (Noh and Woodward 1976). The SLIC interface reconstruction approach, also referred to as piecewise constant method, employs a piecewise constant function to approximate the interface within each computational cell. Piecewise constant types of methods assume that the interface is a line aligned with one of the mesh coordinates. This type of methods is considered to be zeroth-order accuracy when it comes to representing the physical interface.

New methods have been developed to better represent the interface and advect the interface with higher accuracy. These methods include the piecewise linear method (PLIC) by Youngs (1982), Flux Line Segment Volume Of Fluid by Mashayek and Ashgriz (1993), Flux Correct Transport (FCT) by Rudman (1997) and Segment Lagrangian-Volume Of Fluid (SL-VOF) by Guignard et al. (2001).

Within all the interface reconstruction approaches, the piecewise linear method (PLIC) introduced by Youngs (1982) enjoyed the most success and widespread use because it is accurate and robust. The PLIC method approximates the interface with a sloped line segment cutting through each cell with an angle. The angle of the line is estimated based on the discrete volume fraction values

www.manaraa.com

from the neighboring cells. The interceptor of the line is determined by the volume fraction within the cell. The PLIC type of methods is considered 1st order accuracy when it comes to representing the actual interface. As demonstrated by Rudman (1997) and Benson (2002), Youngs' PLIC consistently shows best overall performance when it was compared with Donor and Acceptor method, Flux Correct Transport and other commonly used methods for two-dimensional benchmark study cases. The work by Pilliod and Puckett's (2004) also confirmed Youngs' PLIC reconstruction approach produces the best results in all first-order interface reconstruction methods.

Recent improvements to the original Youngs' PLIC were made by Pilliod and Puckett (2004). In their work, they used a least-square fitting approach to estimate the line slope. This interface approximation is 2nd-order accuracy. In addition to this, an even more accurate interface advancing scheme based on Young's PLIC was developed by Yamada and Takikawa (1999), Harvie and Fletcher (2000) and Scardovelli and Zalski (2003).

The VOF two-phase model accurately represents interface and handles different interface topology. Surface breakup and merging, which are a great challenge to many other two-phase models, are handled naturally in VOF method. This flexibility of treating different interface topology makes VOF method very attractive in free surface flow simulation field. The VOF methods have been used widely in simulating hydrodynamics of waves (Queutey and Visonneau 2007), sloshing tank (Akyildiz and Unal 2006; Ming and Duan 2010) and wave breaking (Guignard et al., 2001). VOF has been applied to simulate large scale open channel flow problems in civil engineering as well. Representative research work includes natural channel flow simulation by Pezzinga (1994), multi-phase flow over a weir and air injection by Liovic et al. (2002), 3D curved channel flow simulation by Lu et al. (2004), violent free surface flow simulation by Löhner et al. (2006, 2007) and supercritical and subcritical dividing channel flow by Li and Zeng (2010). VOF has been used in three-dimensional flow simulation as well, such as studies performed by Gueyffier et al. (1999), Popinet (1999), Meier et al. (2002) and Martinez et al. (2006).

Another notable feature of the VOF method is that VOF is a conservative method and it conserves mass precisely.

The VOF method has been adopted by the popular commercial computational fluid dynamics codes such as SOLA-VOF and its descendants NASA-VOF3D, RIPPLE, FLOW3D and

www.manaraa.com

FLUENT to model multiphase flows. These commercial software packages have been widely used in two-phase flow production studies, such as combustion, ink injection, bubble and wave simulations.

Based on a similar concept as VOF, Osher and Sethian (1988) introduced Level Set method for multiphase flow simulation. In Level Set method, a Level Set function is defined as a distant from the interface with the interface defined as the zero level set. Therefore, if the value of a level set function is known, the location of the interface can be determined. The Level Set function has smoothing characteristics across the interface which makes curvature and surface tension computation straightforward. A transportation equation is written for the Level Set function. However, the Level Set function itself is not a conservative variable, therefore it does not satisfy any conservation equation. It has been known that the mass loss could occur in the Level Set method. To overcome this problem, new initialization and mass correction schemes have been proposed to enforce the mass conservation (Zhang et al., 2010). However, iteration is required and therefore increases the computation cost. The implementation of level set method into existing algorithms for the Navier-Stokes Equations is difficult, while the implementation of VOF to an existing code is straightforward. Multiphase models using Level Set method include works by Sussman et al. (1994), Yue et al. (2003), Lin et al. (2005), Wang et al. (2011) and Kaliakatsos and Tsangaris (2000).

Recent research trends combine the Level Set and Volume of Fluid method (CLSVOF) in the simulation of multiphase flow. In a CLSVOF method, Level Set is used to calculate the surface curvature and surface tension while the VOF is used to correct the mass loss produced in Level Set method. Research has been done in this area by Popinet and Zaleski (1999), Meier et al. (2002), Martinez et al. (2006), Sussman (2000), Sussman and Pucket (2003) and Sussman (2003), and Park et al. (2009). This method has been applied in some Civil Engineering problems, such as simulating channel flow over a broad crest weir and a sharp crest weir by Lv et al. (2011) and bubble flows in a rectangular channel by Ohta et al. (2012).

A few studies for closed conduit flow problems solving the two-phase Navier-Stokes Equations have been carried out for specific problems. Sekavcnik et al. (2006) studied viscous-compressible fluid through a pipe system induced by a transient disturbance at the pipe intake using a commercial ANSYS-CFX Navier-Stokes code. Evstigneev (2008) solved the three-dimensional Navier-Stokes Equations to simulate the flows in a water intake device at Zagorskaya Hydraulic Power Plant in Russia, in which the interface was captured by using a combination of Level Set

www.manaraa.com

and Volume of Fluid method. de Sampaio et al. (2008) modeled a fully developed stratified gas–liquid two-phase flow with a smooth interface in a horizontal circular pipe by solving RANS Navier-Stokes equation. Stockstill and Berger (2009) simulated a navigation lock system that contains both free-surface and pressurized conduit flow by solving the three-dimensional Navier-Stokes Equations in a moving mesh.

Tai and Chung (2011) developed a two-phase Navier-Stokes model with some transient flow features when they studied air-water laminar flow in a circular pipe. In their simulation the pipe was initially empty. The pipe is connected to a tank at one end that supplies both liquid and gas flows through a valve. The valve is then open suddenly to introduce a high inflow to the system similar to a rapid filling process. They studied the motion of the interface front, velocity, and pressure distribution with the pipe. They used a sharp interface method (SIM) coupled with a cut-cell scheme and marker points to track the moving interface. The governing equations for each phase are solved separately and the fluxes at the interface were calculated so that they match between the two phases.

2.7. Knowledge Gap

As discussed in section 2.5, the existing numerical models are suitable for simple mixed flow simulation but are not adequate to simulate two-phase flows with complex air-water interactions. A summary of the limitations of existing numerical models are:

i. The simulation of air escape in the vertical dropshaft was greatly simplified or completely ignored in the existing models. The limited numerical study on dropshaft is a one-dimensional lumped-mass model and not able to reflect the complicated dynamics in the dropshaft.

ii. The simulation of air phase is very limited in the existing numerical models. Air phase in the main pipe is mostly described by a one-dimensional lumped-mass momentum equation.

iii. The existing numerical models for mixed-flows typically assume a distinct interface between air and water phases, which is not always true for a lot of mixed flows, especially geysers, as they are characterized by a mixture of water and air.

www.manaraa.com

iv. It is questionable whether the Shallow Water Equation is applicable in violent flow simulations such as geysers.

2.8. Contributions of This Study

Due to the aforementioned problems, the existing numerical models are not adequate to simulate a geyser feature. One way to capture the full dynamics in both phases, especially the dynamics in the vertical dropshaft, is to develop a true two-phase numerical model that solves the incomprehensive Navier-Stokes Equations.

The intention of this study is to develop a two-phase numerical model solving the Navier-Stokes Equations to study flows transition in stormwater sewer system with the capability of simulating geysers. This study attempts to fill the gap between experimental studies and the existing numerical models on mixed-flow with trapped air effects.

www.manaraa.com

CHAPTER 3 GOVERNING EQUATIONS AND FREE SURFACE MODEL

3.1. System of Governing Equations

3.1.1. Navier-Stokes Equation

The Navier-Stokes (NS) Equation can be written in different forms depending on the type of flow problems or the solution procedures. In the study of multi-phase or multi-fluid flows, the Navier-Stokes Equations are written in a variable density form. It should be mentioned that although air is compressible from the physical property perspective, it can considered as an incompressible flow, and is treated that way in this numerical model. As stated by Panton (2005), incompressible fluid is a thermodynamic term while incompressible flow is a fluid mechanics term. In this study, the density of both water and air remains constant within each phase, and throughout the whole computation. The density is not a function of temperature. The density value only changes at the interface. In such as case, the flow in the air phase can be treated as an incompressible flow and described using the incompressible Navier-Stokes Equation. The two-dimensional incompressible Navier-Stokes Equations can be written in a conservative form as

$$\frac{\partial \rho}{\partial t} + \nabla \cdot (\rho U) = 0 \tag{3.1.1}$$

$$\frac{\partial \rho U}{\partial t} + \nabla \cdot (\rho UU) = -\nabla P + \nabla \cdot \tau + \rho B \tag{3.1.2}$$

where

U - velocity vector (u,v)

p - pressure

B - body force

ρ – density

μ – viscosity

When Eqs. 3.1.1 and 3.1.2 are used for the whole computational domain in the presence of two phases, it is called a one-equation system. This is to distinguish it from a two-equation system in

www.manaraa.com

which the two phases are separated at the internal boundaries and each phase is described by its own Navier-Stokes Equation. In a two-equation system, the fluxes across the internal boundaries need to be calculated and matched to conserve mass and momentum. Significant extrapolations will be needed near the interface as part of the internal boundary implementation. Errors or unphysical approximations could result from the extrapolation process. In a one-equation system, the internal boundary is implicitly included in the Navier-Stokes Equation. This eliminates the difficulties of implementing the internal boundary condition at the interface.

However, there is a downside with the one-equation system. In the solution of the Navier-Stokes equations (Eqs 3.1.1 and 3.1.2) instabilities could arise as the density variation between the two phases becomes significant. For instance, in the simulation of free-surface flows that involve water and air, the density across the interface varies by several orders of magnitude. This sharp density jump poses as a numerical discontinuity and introduces stiffness into the Navier-Stokes Equation matrix. As can be shown, the large density in one phase results in a large off-diagonal coefficient. Hence, the diagonal dominance of the solution matrix is difficult to maintain when the density increases by 1000 times from air to water. The solution procedure can quickly become unstable. Instabilities have been observed in this study when Eqs. 3.1.2 and 3.1.2 are solved for some two-phase flow problems. The instability gets even worse as Reynolds Number goes up. When Reynolds number is large, the solution procedure deteriorates quickly to a point that it is not practical to numerically simulate the flows.

To overcome this problem caused by the density jump, a few attempts have been made by previous researchers using shock-capturing methods to solve the above conservative form Navier-Stokes Equations. Rudman (1998) implemented a Flux Correct Transport (FCT) oscillation-free method to solve Eqs. 3.1.1 and 3.1.2. In the FCT method, a stringent flux limiter and a very fine mesh were used to keep the solution stable. Despite the implementation of the FCT technique, his model was only applied to simulate air-water interface flows with very low Reynolds numbers.

From the above, it seems that it is not practical to solve the one-equation system for an air-water mixed flow. However, this problem can be overcome by solving density-varied Navier-Stokes Equations in a non-conservative form. It has been shown (Drikakis and Rider 2005) that as long as two conditions are satisfied, the non-conservative form of Navier-Stokes Equations are appropriate to use for a two-fluid flow problem, more specifically, a two-fluid problem with large density variation. One condition is that the density in each phase is not related to temperature. The other condition is that the interface is tracked during the solution procedure and therefore the

www.manaraa.com

density in the whole domain can be updated during the computation. The first condition is easy to satisfy in this study since it is assumed that the whole system is under an adiabatic process and the temperature remains constant. The second condition indicates a density transport equation must be solved simultaneously with the Navier-Stokes Equation. The density transport equation can be written as

$$\frac{\partial \rho}{\partial t} + \nabla \cdot (\rho U) = 0 \tag{3.1.3}$$

The non-conservative Navier-Stokes Equations are obtained by taking density out of the differential terms. Therefore, Eqs 3.1.1 and 3.1.2 could be re-written as

$$\nabla \cdot U = 0 \tag{3.1.4}$$

$$\frac{\partial U}{\partial t} + \nabla \cdot (UU) = -\frac{1}{\rho}\nabla p + \frac{1}{\rho}\nabla \cdot (\mu(\nabla U + \nabla U^T)) + B \tag{3.1.5}$$

Equations 3.1.3 through 3.1.5 are called the quasi-conservative form of variable-density Navier-Stokes Equations. This quasi-conservative form of the Navier-Stokes Equations has been widely used in free-surface flow simulations such as coastal waves, flows around ships, flows with bubbles and ink injections. In this study, the quasi-conservative form of Navier-Stokes Equations is used to describe all physical problems and solved in the following velocity variable format

$$\frac{\partial u}{\partial x} + \frac{\partial v}{\partial y} = 0 \tag{3.1.6}$$

$$\frac{\partial u}{\partial t} + \frac{\partial (uu)}{\partial x} + \frac{\partial (vu)}{\partial y} = -\frac{1}{\rho}\frac{\partial p}{\partial x} + \frac{1}{\rho}\left(\frac{\partial}{\partial x}\mu\left(\frac{\partial u}{\partial x} + \frac{\partial u}{\partial x}\right) + \frac{\partial}{\partial y}\mu\left(\frac{\partial v}{\partial x} + \frac{\partial u}{\partial y}\right)\right) + B_x \tag{3.1.7}$$

$$\frac{\partial v}{\partial t} + \frac{\partial (uv)}{\partial x} + \frac{\partial (vv)}{\partial y} = -\frac{1}{\rho}\frac{\partial p}{\partial y} + \frac{1}{\rho}\left(\frac{\partial}{\partial x}\mu\left(\frac{\partial v}{\partial x} + \frac{\partial u}{\partial y}\right) + \frac{\partial}{\partial y}\mu\left(\frac{\partial v}{\partial y} + \frac{\partial v}{\partial y}\right)\right) + B_y \tag{3.1.8}$$

3.1.2. VOF Equation

As mentioned above, to apply the incompressible Navier-Stokes Equations to a two-phase flow problem, a density transport equation (Eq. 3.1.3) must be solved as part of the solution procedure. In this work, this equation is solved using a Volume of Fluid (VOF) two-phase model. In the VOF method, the density and viscosity are represented by a scalar variable

www.manaraa.com

called volume fraction, f_{ij}, representing the volume fraction of the heavier fluid phase (i.e., water) in each computational cell. The volume fraction f has the following properties, namely,

$$0 \leq f_{i,j} \leq 1$$

with

$$f_{ij} = \begin{cases} 1, full\ cell\ (\ or\ water\ cell) \\ (0,1), interface\ cell \\ 0, empty\ cell\ (or\ air\ cell) \end{cases}$$

The interface cell between the two phases can be determined once the volume fraction is known. The density and viscosity within each cell are computed through a simple volume average over the cell, namely,

$$\rho_{ij} = (1 - f_{ij})\rho_{ij}^{water} + f_{ij}\rho_{ij}^{air} \tag{3.1.9}$$

$$\mu_{ij} = (1 - f_{ij})\mu_{ij}^{water} + f_{ij}\mu_{ij}^{air} \tag{3.1.10}$$

For the incompressible flow, conservation of volumne leads to conservation of mass. As a result, the volume fraction is a conservative quantity and satisfies the conservation law. The conservation law for a volume fraction can be written as

$$\frac{df}{dt} = 0 \tag{3.1.11}$$

$$=> \frac{\partial f}{\partial t} + u\frac{\partial f}{\partial x} + v\frac{\partial f}{\partial y} = 0 \tag{3.1.12}$$

Therefore, following the solution of the volume fraction, the density and viscosity field can be advanced using Eqs. 3.1.9 and 3.1.10.

3.1.3. Ideal Gas Equation

In this work, an air pocket will go through compression/expansion process as the pressure within the air pocket varies. It is assumed that the change of the air pocket volume is a pseudo-adiabatic process. The Ideal Gas Law in Eq. 3.1.13 is used to describe the relationship of pressure and volume

$$pV = nRT \tag{3.1.13}$$

www.manaraa.com

Here p is absolute pressure, n is amount in moles, R is the specific gas constant, T is absolute temperature, and V is volume. If the temperature remains constant, the above equation can be simplified to

$$p_1 V_1 = p_2 V_2 \tag{3.1.14}$$

Here p_1 and V_1 represent absolute pressure and volume, respectively, before the compression/expansion, while $p2$ and V_2 represent the pressure and volume after the compression/expansion.

3.2. Numerical Approach for Solving the Navier-Stokes Equations

3.2.1. Projection Method

In this work, the two-dimensional Navier-Stokes equations (Eqs. 3.1.6 - 3.1.8) are solved explicitly using a 1st-order projection method. The projection method is a fractional-step method in which Navier-Stokes Equations are solved in several steps through an operator split scheme. This method was original developed by Chorin (1966, 1967) and has been widely used to solve the incompressible Navier-Stokes equations. Solution of the Navier-Stokes equations used to be troublesome because the continuity equation does not explicitly contain a pressure term, creating zeros along the diagonal of the solution matrix. The fundamental idea of a projection method is to split the momentum equation into two parts to decouple the velocity and pressure calculations (McDonough, 2007, 2008). The first step of a projection method is to solve a modified momentum equation in the absence of pressure to obtain an "auxiliary" or "intermediate" velocity field that does not satisfy the divergence-free constraint. The second step is to convert the remaining momentum equation to a Pressure Poisson Equation (PPE) by implementing the divergence-free condition. The pressure field is solved from the Pressure Poisson Equation. The last step of a projection method is to "correct" or "project" the auxiliary velocity field to a divergence-free velocity field using the calculated pressure.

Specifically, in the projection method the momentum equation is split into two equations shown in Eqs. 3.2.1 and 3.2.2 (McDonough, 2007). Equation 3.2.1 contains all the terms from the original momentum equation except the pressure gradient term. Equation 3.2.2 contains only the pressure gradient term that is left out from the first equation.

www.manaraa.com

$$\frac{\hat{U}-U}{\delta t} + \nabla \cdot (UU) = \frac{1}{\rho}\nabla \cdot (\mu(\nabla U + \nabla U^T)) + B \tag{3.2.1}$$

and

$$\frac{U^{n+1}-\hat{U}}{\delta t} = -\frac{1}{\rho}\nabla p \tag{3.2.2}$$

Combining Eq. 3.2.1 and Eq. 3.2.2 exactly produces the original momentum equation. Equation 3.2.1 is a Burgers' type of equation and is solved using an explicit method. However, the resulted velocity filed does not satisfy the incompressibility constraint (continuity equation, Eq. 3.1.4). Hence the velocity is often referred as "auxiliary velocity" or "intermediate velocity", and denoted by $\hat{U}$.

To solve the second equation, a divergence operator is applied first, namely,

$$\nabla \cdot \frac{U^{n+1}-\hat{U}}{\delta t} = -\nabla \cdot \frac{1}{\rho}\nabla p \tag{3.2.3}$$

Assuming the velocity field at time step *n+1* satisfies the continuity equation, this yields

$$\nabla \cdot U^{n+1} = 0 \tag{3.2.4}$$

Hence, the U^{n+1} term could be eliminated from Eq. 3.2.3. The resulted equation is a Poisson equation that is known as the Pressure Poisson Equation (PPE)

$$-\nabla \cdot \frac{1}{\rho}\nabla p = \frac{\nabla \cdot \hat{U}}{\delta t} \tag{3.2.5}$$

However, it should to be noted that the pressure computed from the above Pressure Poisson Equation above is not a true physical pressure, but more like a velocity potential (McDonough, 2007). Hence it is more appropriate to refer this pressure as a "pseudo-pressure", and denote it as ∅. The Poisson equation for the pseudo-pressure is re-written as

$$-\Delta\phi = \frac{\nabla \cdot \hat{U}}{\delta t} \tag{3.2.6}$$

It has been shown (Kim and Moin,1985) that the pseudo-pressure differs from the true physical pressure *p* by $O(\delta t/RE)$, namely,

$$p = \phi + O\left(\frac{\delta t}{RE}\right) \tag{3.2.7}$$

www.manaraa.com

where δt is the time step and *RE* is the Reynolds number.

A true Pressure Poisson Equation can be derived in a similar approach used in the pseudo Pressure Poisson Equation construction. The computation of true pressure is based on the divergence-free velocity field following the projection step. The derivation of the true Pressure Poisson Equation can be found in the work of McDonough (2007). However, solving a Pressure Poisson Equation is time consuming. The additional algorithm for solving the true Pressure Poisson Equation would increase the total computational effort for Navier-Stokes Equations significantly. In addition to the extra computation, the solution of a true Pressure Poisson Equation becomes unstable or does not converge when discontinuities develops in the velocity field (i.e. shocks, jumps). In this work, unless stated otherwise, the pressure is referred to a pseudo-pressure instead of a real physical pressure.

The last step of a projection method is to "Project" or "Correct" the "auxiliary velocity" into a divergence-free velocity filed using a Leray projector (Foias et al. 2001; McDonough 2007). The projected velocity field satisfies the incompressibility constraint. The projection procedure can be written as

$$U^{n+1} = \widehat{U} - \frac{\delta t}{\rho}\nabla\phi \tag{3.2.8}$$

In this work, the Navier-Stokes Equations are solved explicitly using a finite volume method. The Finite Volume method is a conservative method because the flux exchanges are calculated at the face of each control cell. As the flux exits one control cell, it enters the neighbor cell. This automatically conserves any quantity that is transferred across the face in each control cell locally, as well as globally.

One of the limitations of an explicit time integration method is the time step is limited by the Courant number to ensure numerical stability. Here the Courant number is defined as

$$C_r = max(\frac{u\delta t}{\delta x}, \frac{v\delta t}{\delta y}) \tag{3.2.9}$$

The time step is chosen so that the Courant number is less than one.

www.manaraa.com

3.2.2.Staggered Method

A staggered grid is used in the Projection method for all the computations. A staggered grid structure is naturally consistent with the divergence-free constraint and is less prone to a "checker board" solution (McDonough 2008). In a staggered grid system, the horizontal velocity, *u*, and the vertical velocity, *v*, are defined at the east and north faces of a computational cell, respectively, as illustrated in Fig. 3.1. The scalar variables such as pressure, volume fraction, body force, density and viscosity are defined at the cell center. The flow variables, grid stencil and grid cell index for *x*- and *y*- momentum equations, Pressure Poisson Equation and VOF equation are shown in Fig. 3.1.

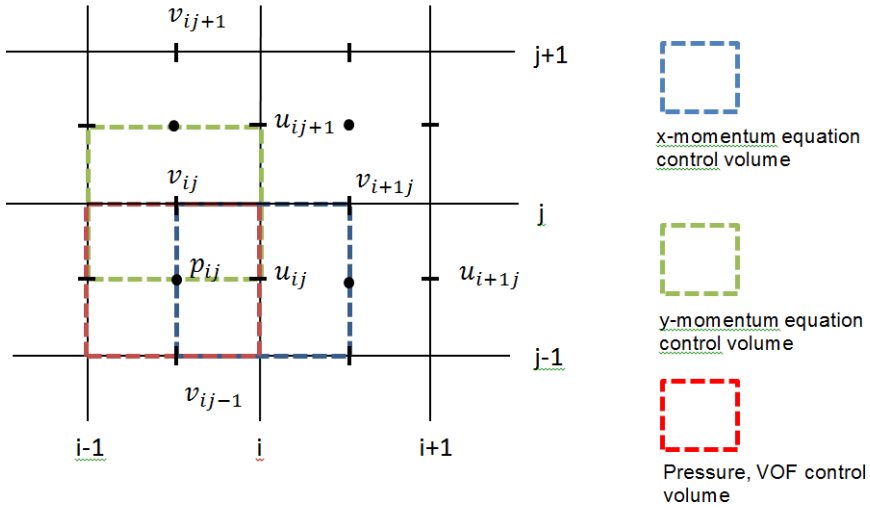

Figure 3.1 Grid cell indexing.

Often, in the discretization of momentum and Pressure Poisson equations values needed for the discretization do not fall exactly at the originally defined location. In those circumstances, a linear interpolation is applied to obtain those values. In this work, for simplicity, all the averages across the horizontal directions are denoted by a bar "$\bar{}$" at the top of the variables while all the averages across the vertical directions are denoted by a tilda "$\tilde{}$". At places where both

www.manaraa.com

horizontal and vertical averages were taken, the average is denoted by both bar and tilda "$\tilde{-}$". The averaging conventions for velocities are shown as follows.

$$\bar{u}_{i,j} = \frac{u_{i,j}+u_{i-1,j}}{2}$$

$$\tilde{u}_{i,j} = \frac{u_{i,j}+u_{i,j+1}}{2}$$

$$\bar{v}_{i,j} = \frac{v_{i,j}+v_{i+1,j}}{2}$$

$$\tilde{v}_{i,j} = \frac{v_{i,j}+v_{i,j-1}}{2} \qquad (3.2.10)$$

The same notation is used for density and viscosity as well. This indexing system is illustrated in Fig. 3.2.

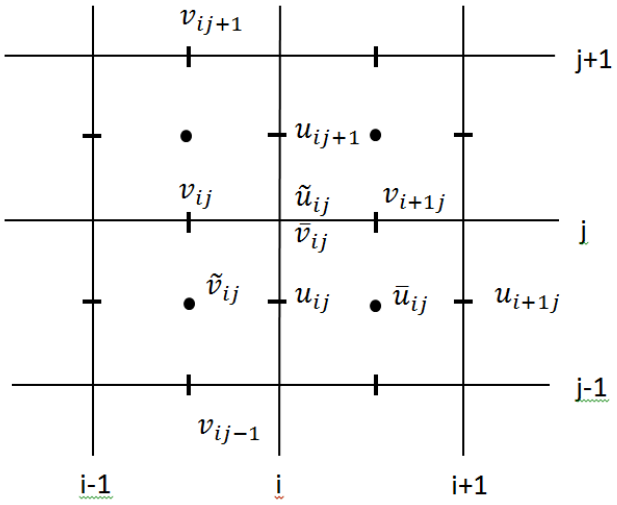

Figure 3.2 Interpolated variable value and grid cell notation.

Another concern with the two-phase flow with large density variations is the averaging of density and viscosity across the interface when there is a significant jump in density and viscosity across the interface. A simple linear average of these properties across the interface is not physically based and often leads to overshoot velocity in the lighter, or less viscous fluid region (Rudman,

www.manaraa.com

1998). This requires an accurate representation of the composite density and viscosity for the interface. Hence, a VOF-based average for density and a harmonic average for the viscosity are adopted in this work to average these properties across the discontinuity. Details of these averaging methods are discussed in section 3.4.

3.2.3. Momentum Equation

The first step of the projection method is to solve a momentum equation, in the absence of pressure, to determine an intermediate velocity field $(\hat{u}, \hat{v})$. Discretization of the momentum equation without pressure is shown in equation 3.2.11. A detail discussion of the discretization process follows.

In general, a 2nd-order accuracy central differencing is used to discretize the spatial differential terms with one exception, the advective term. The advective term is discretized using a 2nd-order upwind scheme, namely, the Quadratic Upstream Interpolation for Convective Kinematics (QUICK) scheme. However, velocities can experience significant changes across the discontinuity in flows with shock fronts, as in the case of a hydraulic jump or a hydraulic bore.

It is well known that the discretization across discontinuities often produces spurious oscillations in the vicinity of the discontinuities in advection-dominant flows. This is often observed in the high-order discretization methods such as 2nd-order central difference methods, Lax-Wendroff methods or MacCormack methods. The oscillations originating from the numerical methods are undesirable because they are purely numerical instead of physical. Moreover, significant oscillations can destabilize the solution procedure. To overcome this problem, the advective terms are usually handled by using an upwind, or shock-capturing, scheme, particularly in cases where discontinuities exist. The simplest upwind scheme is the First Order Upwind (FOU) scheme where a 1st-order forward or backward discretization is taken at the discontinuity based on the upstream direction of the flow. However, it is well known that the 1st-order upwind scheme is very diffusive. Other higher-order upwind methods have been developed, such as QUICK scheme, which poses to be at least 2nd-order accuracy.

Shock-capturing algorithms were developed to handle this particular numerical difficulty. Modern shock capture methods are proved to be efficient, conservative and robust when it comes to handling the discontinuities in flows. The shock capture schemes either search for the locally smoothest stencil and use that stencil to calculate the numerical fluxes or "correct" a low-order diffusive oscillation-free solution to a higher order. As a result, the shock capture schemes

www.manaraa.com

produce a high resolution solution free of oscillations. Representatives of the shock capturing schemes include Flux Correct Transport (Boris and Book 1973; Boris et al. 1975; Zalesak 1979), Essential-Non-Oscillation (ENO) (Shu and Osher 1988) and weighted Essential-Non-Oscillation (WENO) (Liu et al., 1994). Flux Corrected Transport has been used successfully to solve Shallow Water Equation for open channel flows with discontinuities, such as dam break waves and hydraulic bores, by Yost and Rao (1999). In this study, a Flux Correct Transport (FCT) mechanism is used to treat the advective terms when a discontinuity might develop in the flow. Otherwise, the 2nd-order QUICK scheme is used for the advective term discretization. To implement FCT, a First Order Upwind (FOU) solution is corrected by a 2nd order QUICK scheme solution to reach an oscillation-free solution near discontinuities while still maintaining high-order accuracy. Details of the implementation of the FCT scheme for the advective terms are included in section 3.7.

The Navier-Stokes Equations are discretized using a finite volume method. Fig. 3.3 shows the control volume used in velocity *u* computation (*x*- momentum equation). The fluxes are calculated at the four faces of a control cell, namely, east, west, north and south, as shown in Fig 3.3.

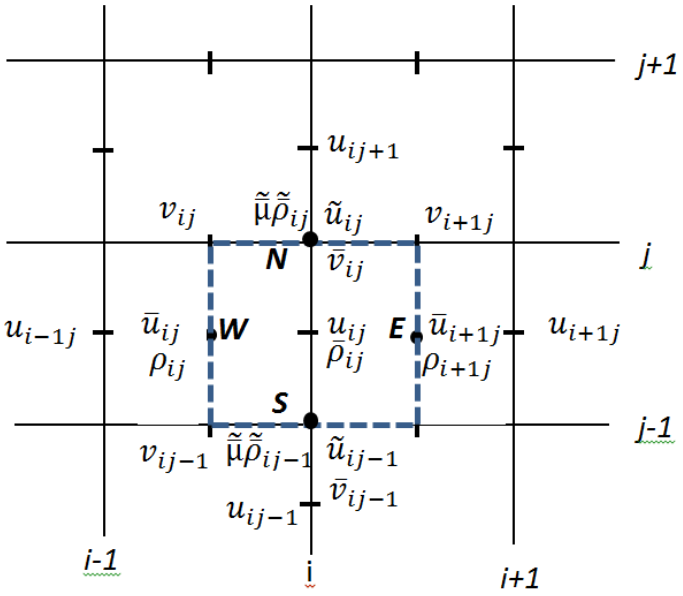

Figure 3.3 *x*-momentum equation discretization (velocity *u* control volume).

www.manaraa.com

The advective terms of the x-momentum equation are discretized as

$$\frac{\partial(uu)}{\partial x}+\frac{\partial(vu)}{\partial y}\Big|_{i,j}=\frac{(uu)_E-(uu)_W}{\delta x}\Big|_{i,j}+\frac{(vu)_N-(vu)_S}{\delta y}\Big|_{i,j} \tag{3.2.11}$$

where $(uu)_E$,$(uu)_W$,$(vu)_N$ and $(vu)_S$ are the momentum fluxes cross the east, west, north and south faces, respectively. Applying a 2nd order accuracy central differencing, the momentum fluxes are calculated as

$$(uu)_E=\bar{u}_{i+1,j}\bar{u}_{i+1,j}$$

$$(uu)_W=\bar{u}_{i,j}\bar{u}_{i,j}$$

$$(vu)_N=\bar{v}_{i,j}\tilde{u}_{i,j}$$

$$(vu)_S=\bar{v}_{i,j-1}\tilde{u}_{i,j-1} \tag{3.2.12}$$

The discretization of advective terms for the *y*–momentum equation is performed in a similar fashion.

When it comes to the discretization of the viscosity term, a few words of cautions exist. It should be noted that the viscous terms in the variable-density Navier-Stokes Equations are written in a stress divergence form. This is to allow viscosity to vary between phases. The divergence operator is taken at the *u*- and *v*- control cell center. The discretization of the divergence operator requires a viscosity values at the *u- and v-* control cell faces, denoted as μ and $\tilde{\mu}$. Viscous terms are discretized based on a central differencing scheme. This requires the inner derivative of the viscous term to be calculated at the control volume faces and the outer divergence to be calculated at the control volume center, i.e. *(i,j).* This is demonstrated below in the discretization of the viscous term in the *x*- momentum equation.

For the *u*– control cell, the viscosity term is discretized as

$$\frac{1}{\rho}\frac{\partial}{\partial x}\left(\mu\left(\frac{\partial u}{\partial x}+\frac{\partial u}{\partial x}\right)\right)+\frac{1}{\rho}\frac{\partial}{\partial y}\left(\mu\left(\frac{\partial v}{\partial x}+\frac{\partial u}{\partial y}\right)\right)$$

www.manaraa.com

$$= \frac{1}{\bar{\rho}_{ij}} \left(\frac{\mu_E \left(\frac{\partial u}{\partial x} + \frac{\partial u}{\partial x} \right)_E - \mu_w \left(\frac{\partial u}{\partial x} + \frac{\partial u}{\partial x} \right)_w}{\delta x} + \frac{\mu_N \left(\frac{\partial v}{\partial x} + \frac{\partial u}{\partial y} \right)_N - \mu_S \left(\frac{\partial v}{\partial x} + \frac{\partial u}{\partial y} \right)_S}{\delta y} \right)$$

(3.2.13)

where μ_E, μ_W, μ_N, μ_S are the composite viscosity at the east, west, north and south faces of the u control cell, respectively, and $\left(\frac{\partial u}{\partial x} + \frac{\partial u}{\partial x} \right)_E$, $\left(\frac{\partial u}{\partial x} + \frac{\partial u}{\partial x} \right)_W$, $\left(\frac{\partial v}{\partial x} + \frac{\partial u}{\partial y} \right)_N$ and $\left(\frac{\partial v}{\partial x} + \frac{\partial u}{\partial y} \right)_S$ are the flux that cross the east, west, north and south faces, respectively, as shown in Fig. 3.3. The averaged viscosity can be written using the index notation defined in section 3.2.2, namely

$$\mu_E = \mu_{i+1,j};\ \mu_W = \mu_{i,j};\ \mu_N = \tilde{\tilde{\mu}}_{i,j};\ \mu_S = \tilde{\tilde{\mu}}_{i,j-1} \tag{3.2.14}$$

The fluxes at each faces are calculated using a 2nd order central differencing as

$$\left(\frac{\partial u}{\partial x} + \frac{\partial u}{\partial x} \right)_E = 2 \frac{u_{i+1,j} - u_{i,j}}{\delta x}$$

$$\left(\frac{\partial u}{\partial x} + \frac{\partial u}{\partial x} \right)_W = 2 \frac{u_{i,j} - u_{i-1,j}}{\delta x}$$

$$\left(\frac{\partial v}{\partial x} + \frac{\partial u}{\partial y} \right)_N = \frac{v_{i+1,j} - v_{i,j}}{\delta x} + \frac{u_{i,j+1} - u_{i,j}}{\delta y}$$

$$\left(\frac{\partial v}{\partial x} + \frac{\partial u}{\partial y} \right)_S = \frac{v_{i+1,j-1} - v_{i,j-1}}{\delta x} + \frac{u_{i,j} - u_{i,j-1}}{\delta y}$$

(3.2.14)

The discretization above indicates density values at the (i,j) cell face and viscosity values at the cell vertexes are needed.

Discretization of the v– control cell follows the same approach. The discretization of the momentum equation (Eq. 3.2.1) is shown in Eqs. 3.2.15 and 3.2.16 with notations defined in section 3.2.2.

www.manaraa.com

$$\frac{\hat{u}_{i,j}^{n+1}-u_{i,j}^{n}}{\delta t}=-\frac{\bar{u}_{i+1,j}^{n}\bar{u}_{i+1,j}^{n}-\bar{u}_{i,j}^{n}\bar{u}_{i,j}^{n}}{\delta x}-\frac{\tilde{u}_{i,j}^{n}\bar{v}_{i,j}^{n}-\tilde{u}_{i,j-1}^{n}\bar{v}_{i,j-1}^{n}}{\delta y}$$
$$+\frac{1}{\bar{\rho}_{i,j}^{n+1}}\left(2\frac{\mu_{i+1,j}^{n+1}\left(u_{i+1,j}^{n}-u_{i,j}^{n}\right)-\mu_{i,j}^{n}\left(u_{i,j}^{n}-u_{i-1,j}^{n}\right)}{\delta x^{2}}\right.$$
$$+\frac{\tilde{\mu}_{i,j}^{n+1}\left(u_{i,j+1}^{n}-u_{i,j}^{n}\right)-\tilde{\mu}_{i,j-1}^{n+1}\left(u_{i,j}^{n}-u_{i,j-1}^{n}\right)}{\delta y^{2}}$$
$$\left.+\frac{\tilde{\mu}_{i,j}^{n+1}\left(v_{i+1,j}^{n}-v_{i,j}^{n}\right)-\tilde{\mu}_{i,j-1}^{n+1}\left(v_{i+1,j-1}^{n}-v_{i,j-1}^{n}\right)}{\delta x\delta y}\right)+B_{x}^{n+1}$$

(3.2.15)

$$\frac{\hat{v}_{i,j}^{n+1}-v_{i,j}^{n}}{\delta t}=-\frac{\tilde{u}_{i,j}^{n}\bar{v}_{i,j}^{n}-\tilde{u}_{i-1,j}^{n}\bar{v}_{i-1,j}^{n}}{\delta x}-\frac{\tilde{v}_{i,j+1}^{n}\tilde{v}_{i,j+1}^{n}-\tilde{v}_{i,j}^{n}\tilde{v}_{i,j}^{n}}{\delta y}$$
$$+\frac{1}{\tilde{\rho}_{i,j}^{n+1}}\left(\frac{\tilde{\mu}_{i,j}^{n+1}\left(v_{i+1,j}^{n}-v_{i,j}^{n}\right)-\tilde{\mu}_{i-1,j}^{n+1}\left(v_{i,j}^{n}-v_{i-1,j}^{n}\right)}{\delta x^{2}}\right.$$
$$+2\frac{\mu_{i,j+1}^{n+1}\left(v_{i,j+1}^{n}-v_{i,j}^{n}\right)-\mu_{i,j}^{n}\left(v_{i,j}^{n}-v_{i,j-1}^{n}\right)}{\delta y^{2}}$$
$$\left.+\frac{\tilde{\mu}_{i,j}^{n+1}\left(u_{i,j+1}^{n}-u_{i,j}^{n}\right)-\tilde{\mu}_{i-1,j}^{n+1}\left(u_{i-1,j+1}^{n}-u_{i-1,j}^{n}\right)}{\delta x\delta y}\right)+B_{y}^{n+1}$$

(3.2.16)

3.2.4.Pressure Poisson Equation

The Pressure Poisson Equation (PPE) is an elliptical equation and can be solve directly provided that the boundary conditions are known. In this study, this equation is solved using a fixed point form Successive Overrelaxation (SOR) iterative method.

The implementation of a SOR method for a Poisson equation is straightforward. However, cautious must be paid on how the Pressure Poisson Equation should be solved. The solution procedure of a Pressure Poisson Equation must be consistent with the construction of the equation. As discussed earlier, the Pressure Poisson Equation is derived by taking a divergence of the momentum equations. This indicates the discretized Pressure Poisson Equation should exactly match how the divergence and gradient operators are taken. This requires that the divergence be

www.manaraa.com

calculated at the center of the pressure control volume while the pressure gradient is evaluated at the control volume faces. The control volume used in the discretization of the Pressure Poisson Equation is illustrated in Fig. 3.4.

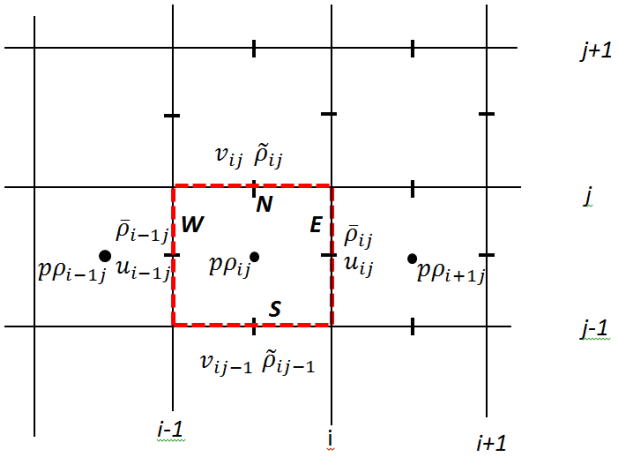

Figure 3.4 Control volume for Pressure Poisson Equation.

The discretization of the divergence operator is

$$\nabla \cdot \frac{1}{\rho}\nabla p = \frac{\left(\frac{1}{\rho}\nabla p\right)_E - \left(\frac{1}{\rho}\nabla p\right)_W}{\delta x} + \frac{\left(\frac{1}{\rho}\nabla p\right)_N - \left(\frac{1}{\rho}\nabla p\right)_S}{\delta y} \tag{3.2.17}$$

where

$$\left(\frac{1}{\rho}\nabla p\right)_E = \frac{1}{\bar{\rho}_{i,j}}\left(\frac{p_{i+1,j} - p_{i,j}}{\delta x}\right)$$

$$\left(\frac{1}{\rho}\nabla p\right)_W = \frac{1}{\bar{\rho}_{i-1,j}}\left(\frac{p_{i,j} - p_{i-1,j}}{\delta x}\right)$$

$$\left(\frac{1}{\rho}\nabla p\right)_N = \frac{1}{\tilde{\rho}_{i,j}}\left(\frac{p_{i,j+1} - p_{i,j}}{\delta y}\right)$$

www.manaraa.com

$$\left(\frac{1}{\rho}\nabla p\right)_s = \frac{1}{\tilde{\rho}_{i,j-1}}\left(\frac{p_{i,j} - p_{i,j-1}}{\delta y}\right.$$

(3.2.18)

The discretization above indicates density values are needed at the cell face. The discretization of the Pressure Poisson Equation (Eq. 3.2.5) is

$$\frac{\frac{1}{\bar{\rho}_{i,j}^{n+1}}\left(p_{i+1,j}^{n+1} - p_{i,j}^{n+1}\right) - \frac{1}{\bar{\rho}_{i-1,j}^{n+1}}\left(p_{i,j}^{n+1} - p_{i-1,j}^{n+1}\right)}{\delta x^2} + \frac{\frac{1}{\tilde{\rho}_{i,j}^{n+1}}\left(p_{i,j+1}^{n+1} - p_{i,j}^{n+1}\right) - \frac{1}{\tilde{\rho}_{i,j-1}^{n+1}}\left(p_{i,j}^{n+1} - p_{i,j-1}^{n+1}\right)}{\delta y^2}$$

$$= \frac{1}{\delta t}\left(\frac{\hat{u}_{i,j}^{n+1} - \hat{u}_{i-1,j}^{n+1}}{\delta x} + \frac{\hat{v}_{i,j}^{n+1} - \hat{v}_{i,j-1}^{n+1}}{\delta y}\right)$$

(3.2.19)

Often when solving the Pressure Poisson Equation, a homogenous Neumann boundary condition is needed for all boundaries, such as flows in a closed container. This is called a pure homogenous Neumann Boundary Condition system, which contains an infinite number of solutions. In such a case, a reference pressure is provided to create a unique solution.

SOR is an iterative method. The convergence rate of a SOR method is directly related to the relaxation parameter. The optimal relaxation parameter could be approximated based on the spectral radius of the problems. However, for transient problems, it has been noticed that the SOR convergence rate drops as the solution advances. In some scenarios, the convergence rate even drops to a point that the SOR method does not converge after a certain computing period. This often occurs when the flow becomes irregular and discontinuities start developing in the flow field. Although a relaxation parameter value that is close to the optimal value leads to a much faster convergence, it does not always guarantee convergence as time advances. As a result, a relaxation parameter value that is smaller than the optimal value was typically used in SOR to keep the solution procedure stable and converge. In some cases, a relaxation parameter value of one is used to keep PPE convergent. When the relaxation parameter value of one is used, SOR becomes Gauss-Seidel iteration while a value less than one leads to a under-relaxation iteration.

www.manaraa.com

3.2.5.Projection Equation

The last step of the projection methods is to project the auxiliary velocity field to a divergence-free velocity field using the pressure calculated from the Pressure Poisson Equation. To be consistent with the construction of the projector, the projection is taken at the cell center in the velocity component *u* and *v* control cells. The control cells for *u* and *v* are shown in Fig 3.5.

The projection equation (Eq. 3.2.8) for *u* and *v* is discretized as

$$u_{ij}^{n+1} = \hat{u}_{ij}^{n+1} - \delta t \frac{1}{\bar{\rho}_{i,j}^{n+1}} (p_{i+1,j}^{n+1} - p_{i,j}^{n+1})$$

$$v_{ij}^{n+1} = \hat{v}_{ij}^{n+1} - \delta t \frac{1}{\tilde{\rho}_{i,j}^{n+1}} (p_{i,j+1}^{n+1} - p_{i,j}^{n+1}) \qquad (3.2.20)$$

As indicated in the equation above, averaged density values ($\bar{\rho}$ and $\tilde{\rho}$) at the *(i,j)* cell faces are needed.

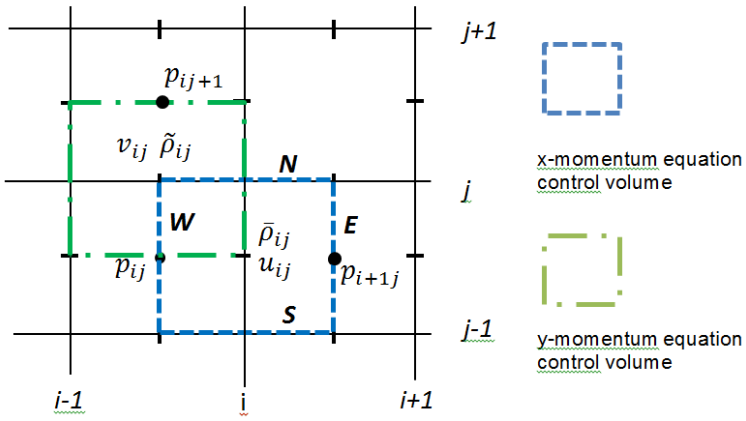

Figure 3.5 Control volume for projection equation.

www.manaraa.com

3.3. Two-phase Flow Model

To simulate the two-phase flow, a Volume of Fluid method is employed. In a Volume of Fluids model, the interface cell are determined from the volume fraction.. However, a volume fraction value does not explicitly define the shape or the location of an interface. In the Volume of Fluids model, the interface is reconstructed from the volume fraction distribution. A Volume of Fluid algorithm contains two steps: interface reconstruction and interface advection. The interface reconstruction is to determine the shape and location of the interface based on the known volume fraction distribution. The interface advection is to advance the reconstructed interface to a new location in each time step by solving the volume fraction transport equation.

3.3.1.PLIC Interface Reconstruction and Advection

In section 2.5, the approaches commonly used in the interface reconstruction have been reviewed. As mentioned previously, in this work Youngs' PLIC method (Youngs 1982) is used to reconstruct the interface.

In addition Youngs' geometric based method will be used to advance the interface. The volume fraction transport equation (Eq. 3.1.12) is an advection equation. In two-phase flow problems, the volume fraction at one side of the interface has a value of one and a value of zero at the other side. This is a numerical discontinuity and indicates that the volume fraction at the interface is not differentiable. As discussed in section 3.2, this always poses numerical difficulties for advection-dominant flows. Numerical oscillations tend to appear in the vicinity of the discontinuities if special care is not taken in the discretization procedure. Traditional approaches to handle this type of problems are to construct an oscillation-free finite difference discretization for the advection term, such as using an upwind weighted scheme for the advection discretization. Several shock-capture schemes have been developed to solve this pure advection equation with discontinuity. However, it has been found (Kothe et al., 1996) that if a high-order finite difference discretization is applied to solve the volume fraction transport equation the interface thickness does not remain compact. The interface spreads as a result of the numerical diffusion introduced to preserve monotonicity. It is also well-known that finite difference methods are not conservative as the fluxes across the interface between two adjacent cells might not match in the discretization process. It appears that the traditional shock capture methods, which are typically a combination of upwind and downwind differentiating, is a good approach to solve the volume fraction transport equation.

www.manaraa.com

To conserve the volume as well as remaining oscillation-free, Youngs (1982) proposed a geometric-based integration approach to solve the volume fraction transport equation. This geometric-based integration is a finite volume approach that calculates the flux across the interface and advances the volume fraction in time within each control cell. It is probably the most widely used method in VOF models. In Youngs' VOF, the volume fraction transport equation is solved geometrically instead of algebraically and hence there is no differentiating across the interface. The fraction volume transport equation is integrated using "outward" fluxes that are calculated geometrically at the four faces of each control volume. The flux is then exchanged and tracked between neighboring cells.

3.3.2. Interface Reconstruction

A volume fraction value between zero and one indicates the presence of an interface. In Youngs' piecewise linear interface reconstruction (PLIC), the interface is defined as an inclined line described by a line function

$$n_x x + n_y y + b = 0 \tag{3.3.1}$$

where (n_x, n_y) is the normal vector of the interface line pointing into the heavier fluid, as depicted in a dark color in Fig. 3.6. In the PLIC method, the normal vector is calculated based on the gradient of the volume fractions in the neighbor cells (nine cell stencil in the case of 2D and 27-cell stencil in the case of 3D).

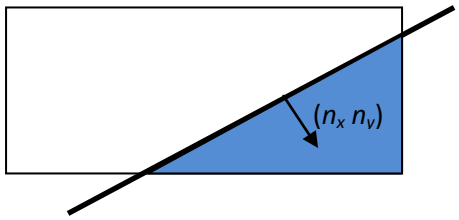

Figure 3.6 PLIC interface line segment.

www.manaraa.com

The normal calculation is

$$n_{i,j}^{x} = \frac{1}{\delta x}(f_{i+1,j+1} + 2f_{i+1,j} + f_{i+1,j-1} - f_{i-1,j+1} - 2f_{i-1,j} - f_{i-1,j-1})$$

$$n_{i,j}^{y} = \frac{1}{\delta y}(f_{i+1,j+1} + 2f_{i,j+1} + f_{i-1,j+1} - f_{i+1,j-1} - 2f_{i,j-1} - f_{i-1,j-1}) \qquad (3.3.2)$$

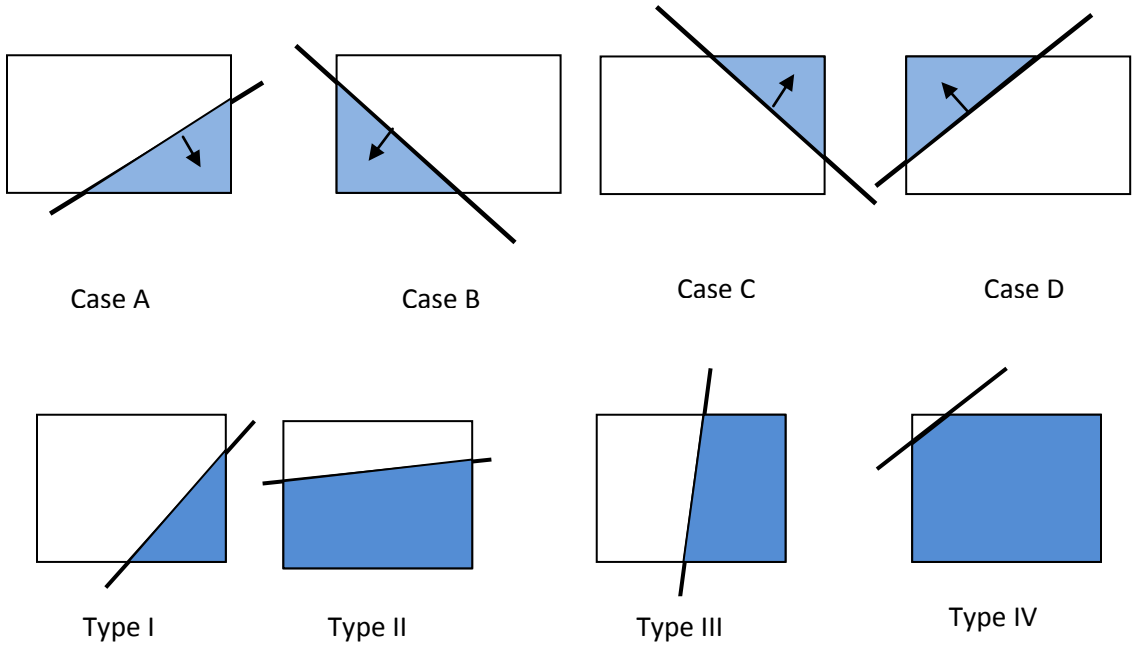

Figure 3.7 Interface configurations in PLIC interface reconstruction.

Following the determination of the slope of the interface line, the interceptor of the line can be determined by fitting the straight line within the cell until the line exactly cuts the cell with a fraction volume value of f_{ij}. As shown in Fig. 3.7, based on the orientation of the interface, there are four configurations (case A, B, C, and D) in the interface normal calculation. Each configuration contains four possible types (type I, II, III, and IV) of interface alignments. The volume of the heavier fluid (shaded area) can be calculated algebraically.

www.manaraa.com

3.3.3. Operator Splitting Interface Advection

Puckett et al., (1997) modified the original VOF governing equation (Eq. 3.1.12) by adding a divergence-free constraint to the right hand side, converting it to a conservative form. This "divergence correction" is to count the change of the effective cell volume after the first sweep. The modified volume fraction transport, shown in Eq. 3.3.3, was shown to produce more accurate results (Puckett et al. 1997).

$$\frac{\partial f}{\partial t} + \nabla \cdot (\boldsymbol{u} f) = f \nabla \cdot \boldsymbol{u} \tag{3.3.3}$$

To solve Eq. 3.3.3, an operator splitting approach is adopted which involves sweeping the time integration in both *x* and *y* directions. The operator splitting process is shown as

$$\hat{f}_t + (fu)_x = f u_x \tag{3.3.4}$$

$$f_t + (\hat{f} v)_y = \hat{f} v_y \tag{3.3.5}$$

As suggested by Puckett et al. (1997) and Rider and Kothe (1998), in order to maintain conservation of volume, Eq. 3.3.4 should be solved implicitly and Eq. 3.3.5 should be solved explicitly. These equations are discretized in a conservative form using fluxes defined at the cell faces of control volume cell (*i*, *j*), namely,

$$\hat{f}_{i,j} = \left\{ f_{i,j}^{n} - \frac{\Delta t}{\Delta x}\left[F_{i+\frac{1}{2},j} - F_{i-\frac{1}{2},j} \right] \right\} / [1 - \frac{\Delta t}{\Delta x}[u_{i,j} - u_{i-1,j}] \tag{3.3.6}$$

$$f_{i,j}^{n+1} = \hat{f}_{i,j} \left\{ 1 + \frac{\Delta t}{\Delta y}[v_{i,j} - v_{i,j-1}] \right\} - \frac{\Delta t}{\Delta y}[\hat{G}_{i,j+1/2} - \hat{G}_{i,j-1/2}] \tag{3.3.7}$$

where, $F_{i-1/2,j}$ $F_{i-1/2,j}$ $\hat{G}_{i,j+1/2}$ and $\hat{G}_{i,j-1/2}$ are geometrically calculated fluxes that "flow out of" the cell. $F_{i-1/2,j}$ and $F_{i+1/2,j}$ are the horizontal fluxes defined at the west and east faces while $\hat{G}_{i,j+1/2}$ and $\hat{G}_{i,j-1/2}$ are the vertical fluxes defined at the north and south faces. Figure 3.8 demonstrates the "outgoing" flux crossing the east face.

www.manaraa.com

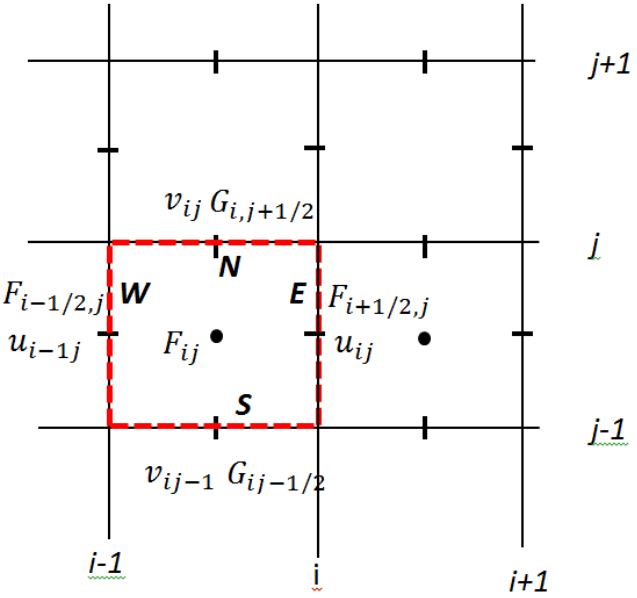

Figure 3.8 Control volume for VOF equation.

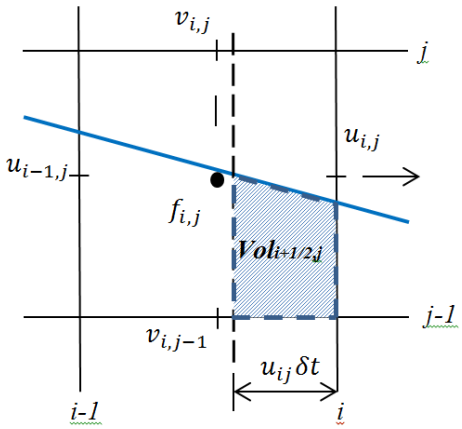

Figure 3.9 Geometric calculation of VOF volume flux across the east face.

The geometric-based flux calculation is illustrated in Fig. 3.9. All the fluxes are calculated in such a way that the solution of the volume fraction transport equation conserves volume both locally and globally, which is one of the advantages of a finite volume based method. In the

www.manaraa.com

incompressible flow case, conservation of volume is equivalent to the conservation of mass. In Fig. 3.9, the shaded area ($Vol_{i+1/2,j}$) represents the "outward" flux crossing the east face of cell (i, j) assuming the horizontal velocity $u_{i,j}$ at this face is positive.

To calculate the outward volume fraction flux, $Fi_{+1/2,j}$, the first step is to create an imaginary line by shifting the right face of cell (i, j) by a distance of $u_{ij}\delta t$. Because the shape and location of the interface are known from the reconstruction process, the area (or volume) cut between the imaginary line and the cell face, shown as a shaded area in Fig. 3.9, could be calculated geometrically. This volume, denoted as $Vol_{i+1/2,j}$, is the volume of the heavy fluid that will be advected through the right boundary to the adjacent cell in one time step. The volume fraction flux is calculated from

$$F_{i+1/2,j} = (fu)_{i+\frac{1}{2},j} = \frac{Vol_{i+\frac{1}{2},j}u_{i,j}}{u_{i,j}\delta t\delta y} = Vol_{i+\frac{1}{2},j}/(\delta t\delta y) \tag{3.3.8}$$

The "Outwards" Volume fraction fluxes at the other three faces can be calculated in a similar fashion.

3.3.4. VOF Bound Check and Redistribution

A bound check is performed at the end of each VOF computation process to avoid volume fraction value going above one or becoming negative. A threshold value, $\epsilon = 10^{-6}$, is used as the bound as suggested by several previous studies (Rudman, 1997, 1998; Kothe and Rider, 1996). The bound check process is implemented as

$$f_{ij} = \begin{cases} 1, if\ f_{ij} > 1 + \epsilon \\ 0, if\ f_{ij} < -\epsilon \end{cases}$$

For a resultant volume fraction value that is larger than one, the volume is redistributed in the nearest neighboring cells. For a resultant volume fraction value that is less than zero, the volume is accumulating by taking out volumes from the nearest neighboring cells. This is a manual redistribution process that is more ad-hoc than having any physical meanings. It is implemented purely for the purpose to conserve mass. However, results from this work have indicated that the redistribution subroutine is hardly used in the computation.

3.3.1. Algorithm for Volume-of- Fluid

www.manaraa.com

The overall procedure to solve the VOF fraction equations is illustrated in a flowchart in Fig. 3.10. The figure outlines the computational procedure for advancing from time step n to time step $n+1$.

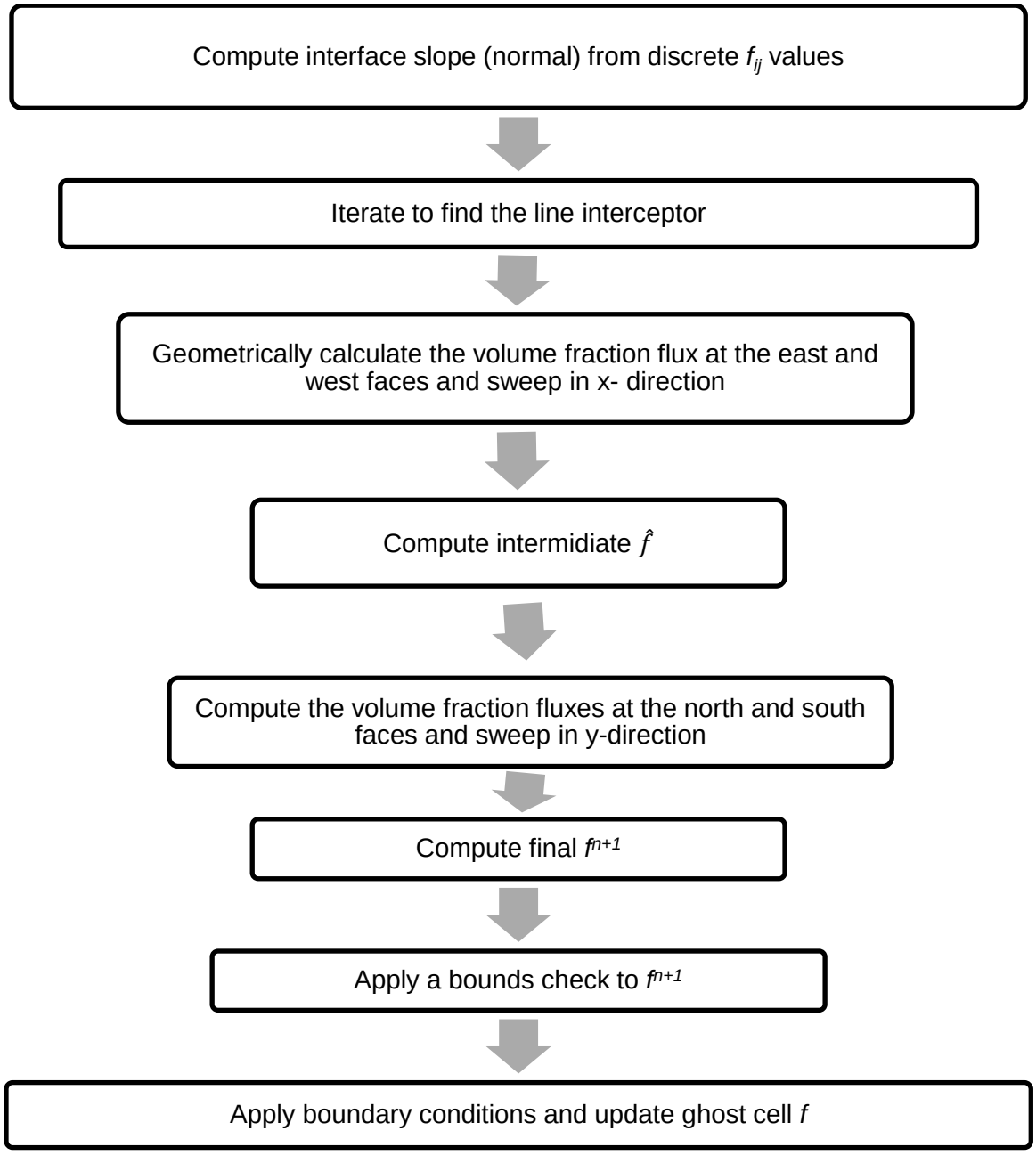

Figure 3.10 VOF algorithm flow chat.

www.manaraa.com

3.4. Averaging Density and Viscosity across the Interface

As shown in the discretization of the Navier–Stokes Equations, the spatial discretization requires density and viscosity values at the cell center, cell face and cell vertex. However, in the staggered grid system, all the scalar variables such as density, viscosity and volume fraction are defined at the cell center. The cell center density and viscosity could be computed from the volume fraction value. However, the density and viscosity values at the cell face and cell vertex are not available. Some type of averaging is needed to obtain a value for these locations.

The simplest way to obtain a value for these locations is to perform a straight averaging on the cell centered variables. For interface flows with large density and viscosity variations across the interface, such type of averaging could result in significant numerical errors. At the interface, the density and viscosity values vary by several orders of magnitude. The linear interpolation of density in an interfacial cell is neither physical nor accurate. This coarse averaging has been believed to be a source of spurious currents in some flow simulations (Rudman 1998). For instance, the well-known two-phase model, RIPPLE (Kothe et al. 1991), failed in the simulation of a stationary inclined plane perpendicular to gravity due to erroneous static pressure distribution.

To better represent the composite density values at cell faces and cell vertexes, a volume-based averaging approach, proposed by Rudman (1998), is adopted in this work. The volume-based averaging approach can be demonstrated using the u velocity control volume (or x-momentum control volume), as shown in a red dashed box in Fig. 3.11. In the calculation of velocity component u, an averaged density values at the center of the u control cell, denoted as $\bar{\rho}$, is needed in the Pressure Poisson Equation and the projection equation. As indicated in the figure, a simple linear average between this cell and the east neighbor is not representative of the actual density in the x-momentum control volume, especially if the interface is fairly steep.

There is a distinct difference between the volume-based averaging and a simple averaging. Since density in the Navier-Stokes equations is related to mass, the volume-based averaging counts the volumes (or mass) of each phase and average them over the whole control volume. From Figure 3.11, it can be seen that the volume-based averaging calculates the volume fraction, shown as the cross shaded area. This results in a composite density that better represents the x-momentum control cell.

www.manaraa.com

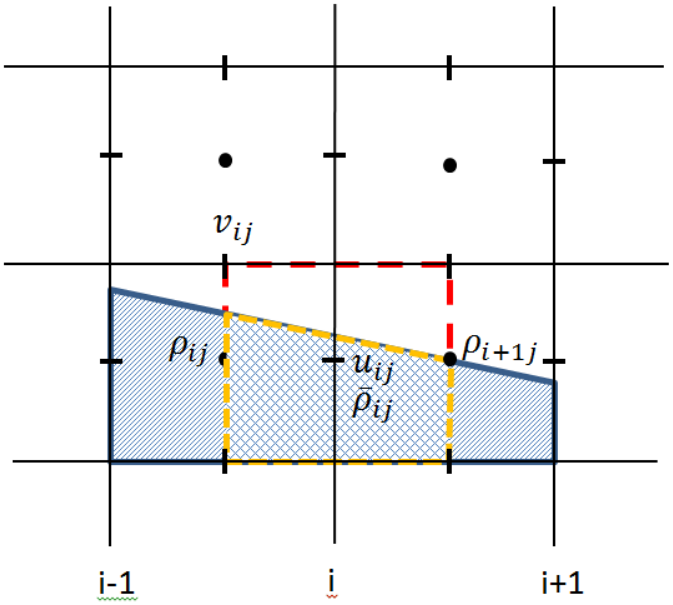

Figure 3.11 Estimate density for an *x*-momentum control volume.

For viscosity, a harmonic average suggested by Rudman (1998) is used. . The principal behind a harmonic average is to assign a higher weight to the more viscos fluid. This weighted average is to ensure that fluid stresses do not give rise to excessive acceleration in less viscous fluid near interface (Rudman, 1998). The harmonic averaging, is a weighted averaging, given as

$$\bar{\mu}_{i,j} = 2\frac{\mu_{i,j}\mu_{i+1,j}}{\mu_{i,j}+\mu_{i+1,j}} \tag{3.4.1}$$

3.5. Initial Conditions

The governing Navier-Stokes Equations is for unsteady incompressible flows. Therefore both initial and boundary conditions are required to solve the equations.

As stated by Sani et al. (2006) and Gresho (1991), the divergence-free condition is related to every aspect of solving incompressible flow equations. This condition should hold for both initial and boundary conditions.

www.manaraa.com

The initial velocity is set so that the velocity field satisfies the divergence-free condition in both the domain and at all boundaries. A convenient choice is to set the initial flow at rest. Prescription for the initial pressure distribution is not necessary as the pressure field is determined from the momentum equation based on a reference pressure, unless Dirichlet pressure boundaries are prescribed.

For flow transition problems, the computation often starts from a steady-state. In such a case, the simulation contains two steps. The first step is to generate a steady-state flow field that is suitable for the simulated problem and that satisfies the divergence-free condition. The second step is the real simulation using the steady-state flow field from the first step as an initial condition.

3.6. Boundary Conditions

The governing equations listed in Section 3.2 contain a series of partial differential equations of different types, including a Momentum equation that can be either hyperbolic or parabolic, an elliptical Pressure Poisson Equation and a hyperbolic volume of fluid equation. To uniquely solve these equations numerically, boundary conditions are needed.

Boundary Conditions for Momentum Equations

The boundary conditions required for the momentum equation is quite different for different types of flows.

Open channel flows are characterized by Froude number, defined as $Fr = v/\sqrt{gh}$, where v is a reference velocity and h is flow depth. The term $\sqrt{gh}$ represents the speed of a disturbance wave. Froude number in open channel flow is analogous to the Mach number in aerodynamics. Based on the Froude number value, open channel flows could be categorized into two types. If Fr is larger than one, the fluid velocity is greater than the disturbance wave speed and the flow is said to be supercritical. In this case, the disturbance waves (information) cannot travel upstream. If Fr is less than one, the flow is called subcritical and the disturbance waves (information) can travel in all directions, i.e. both upstream and downstream directions in a two-dimensional flow case.

The two types of flows require boundary conditions to be specified at different sides of the flows. For supercritical flows, both of the velocity and the flow depth are specified at the inflow. For subcritical flows, the velocity is specified at the inflow while the flow depth (or a rating curve) is specified at the downstream (outflow) end (Ferziger and Peric 2001; Bradford and Sanders 2002).

www.manaraa.com

Boundary Conditions for VOF Equation

The VOF equation is a 1st-order hyperbolic equation which indicates the information propagates towards downstream only (Carvalho 2008). In open channel flows, the boundary condition for this equation is only needed at places where the streamline enters the flow field, such as at an inflow boundary.

Boundary Conditions for Pressure Poisson Equation

The Pressure Poisson Equation is an elliptical equation. It requires a numerical boundary condition for all boundaries. However, the numerical boundaries must be consistent with the physical condition at the boundary. In the projection method, pressure is used to enforce the divergence-free constraint by correcting the auxiliary velocity field. Hence if a velocity is specified at a boundary, the corresponding velocity correction in the projection equation should be zero, which requires a zero pressure gradient for this boundary.

3.6.1. Ghost Cell

It seems unlikely, however, that physical boundary conditions are known at all boundaries. Most of the time, the variable values at a boundary are unknown and need to be solved as part of the numerical simulation. To solve a partial differential equation, values outside of the computation domain are often needed to carry the discretization at the boundaries. In such cases, additional numerical boundary conditions must be provided as an augment to complete the discretization. In this study, a layer of fictitious cells, called 'ghost' cells, are defined to implement the boundary conditions. The ghost cells are adjacent to the boundary cells, as demonstrated in Fig. 3.12. There is no computation for the ghost cells. The variable values in ghost cells are specified such that the resulted boundary flux is consistent with the physical condition.

A total of six types of boundary conditions are used in this study including non-slip wall, free-slip wall, velocity inflow, pressure inflow, open boundary, outflow and an internal boundary between two computational domains. As stated earlier, a one-equation system is solved in this study. Therefore, the free-surface boundary is embedded in the solution procedure implicitly. Consequently, no boundary condition is needed for the interface. In this work, surface tension is assumed negligible due to the absence of significant surface curvature, in general. The implementation of these boundary conditions is discussed, as follows.

www.manaraa.com

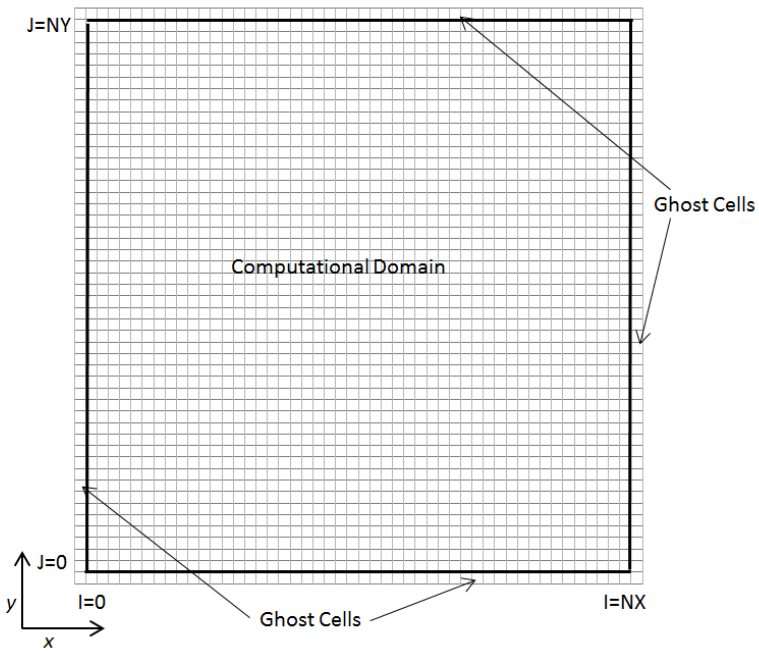

Figure 3.12 Ghost cells in boundary condition implementation.

3.6.2. Wall Boundaries

A wall is often referred as a solid boundary. At a solid boundary, the normal flow flux is zero. This results in a value of zero for the velocity component that is normal to the wall. For the velocity component that is tangential to the wall, the wall boundary is divided into two types for this work – no-slip wall and free-slip wall. For a no-slip wall, the tangential velocity component at the wall is zero. For a free-slip wall, there is no tangential shear stress which means the tangential velocity component has a zero gradient at the wall. For example, for a wall boundary that is at the top of the domain, we have

i. No-Slip Wall

$$u|_{wall} = 0 \;\Rightarrow u_{i,ny+1} = -u_{i,ny}$$

$$v|_{wall} = 0 \Rightarrow v_{i,ny} = 0 \qquad (3.5.1)$$

www.manaraa.com

ii. Free Slip Wall

$$\left.\frac{\partial u}{\partial y}\right|_{wall} = 0 \quad => u_{i,ny+1} = u_{i,ny}$$

$$v|_{wall} = 0 => v_{i,ny} = 0 \tag{3.5.2}$$

When it comes to the pressure boundary condition at a wall, the pressure should be set to enforce the divergence-free constraint. Consequently, a zero gradient (homogeneous) Neumann boundary condition is imposed for all wall boundaries, namely,

$$\left.\frac{\partial p}{\partial n}\right|_{wall} = 0 \; => p_{i,ny+1} = p_{i,ny} \tag{3.5.3}$$

This is consistent with the zero normal-flux boundary condition discussed above. This is also consistent with the projection method used in the solution of the Navier-Stokes equations. A homogeneous Neumann boundary condition leads to a zero correction to the normal velocity component at a wall boundary.

For the Volume Fraction boundary condition, volume fluxes across both no-slip and free-slip walls are zero. The volume fraction values in the ghost cell are used only in the calculation of the interface normal. These values are determined based on the adjacent interior cell values. If the interior cell is full, the ghost cell is assumed to be full; vice versa. If the interior cell is an interface cell, linear extrapolation is performed to obtain the volume fraction values in the ghost cells.

3.6.3. Inflow Boundary

At the inlet boundary, either velocity or pressure Dirichlet type of boundary can be specified, but not both at the same time. There are two types of inflow boundaries at an inlet: velocity inflow and pressure inflow. For a velocity inflow boundary, the velocity profile at the inlet is prescribed while pressure at the inlet is solved from Navier-Stokes Equations. For a pressure inflow boundary, the pressure distribution is provided at the inlet while the inflow velocity is solved.

www.manaraa.com

a. Velocity Inflow

For single-phase flows, the velocity inflow profile could be determined fairly easily. The velocity profile can be either scaled from a known analytical solution or simply specified as uniform, based on a pre-defined flowrate.

The velocity inflow for an open channel flow or free surface flow is more complicated. As discussed earlier, for open channel flows, depending on the flow type (i.e. supercritical or subcritical) boundary flow information propagates in different directions in the domain. Hence, for a supercritical flow, both velocity and depth should be only specified at the upstream end while for a subcritical flow, velocity can only be specified at the inflow and a depth (or rating curve) is only specified at the outflow. For both types of flows, the inflow profile is typically assumed to be uniform. For a supercritical flow, the velocity profile is calculated from the specified depth based on a pre-defined flowrate. For a subcritical flow, the depth is calculated as part of the solution. The velocity profile is obtained from the resultant depth based on a pre-defined flowrate and prescribed at the inlet.

For a velocity inflow boundary, the pressure is calculated from Pressure Poisson Equation. The pressure at the ghost cell is set in such a way so that the pressure gradient at the inflow boundary is zero, which corresponds to a zero inflow velocity correction in the projection step.

For the VOF transport equation, an inflow volume fraction must be provided at the inflow boundary where streamline enters the flow field. For the velocity inflow boundary case, the volume flux that enters the domain is directly calculated from the inflow velocity and the flow depth at the inlet. The volume fraction of ghost cells in the velocity inflow boundary condition is set as the same as the adjacent boundary cells.

b. Pressure Inflow

For a pressure inlet boundary, the pressure distribution is specified at the inlet. Additionally, for this type of inflow boundary, a reference pressure must be provided in the flow region to prescribe pressure gradient information for the momentum equation. The reference pressure usually is a specified pressure distribution at the outlet. Basically, this is to prescribe a pressure drop for the flow between the inlet and the outlet. In the pressure inflow cases, the velocity at the inlet is determined by solving the Navier-Stokes Equations so that the pressure loss within the domain matches the specified value. The pressure in the ghost cell is linearly extrapolated from

www.manaraa.com

the interior pressure and the specified pressure at the boundary. This prescribed pressure boundary has been studied by several researchers such as Heywood et al. (1996) and Fernandez-Feria and Sanmiguel-Rojas (2004) for bound and unbounded domains.

In this work, the pressure distribution in the inlet is assumed to be hydrostatic if gravity is present. Otherwise the pressure distribution is assumed to be constant if no gravity exists. This estimation is reasonable by selecting inlet and outlet surfaces sufficiently far away from each other and normal to the inflow and outflow (Heywood et al., 1996). In the open channel flow case, it means the inlet and outlet should be perpendicular to the channel.

For the VOF transport equation, the calculation of the inflow volume fraction is the same as in the inflow velocity case following the solution of the inflow velocity and depth. The volume fraction of ghost cells is set as the same as the boundary cells.

3.6.4. Outflow Boundary

The outflow boundary condition poses a bit of a challenge because an outflow boundary condition is not a physical boundary condition, and does not exist in nature. They are set artificially because of the need to truncate a computational domain for the purposes of efficiency. Problems can arise from this simplification, especially in complicated flow problems, such as turbulence simulations. The implementation of an outflow boundary condition is an ongoing research topic and a lot of studies have been done in this area. The method proposed by Ziaei et. al. (2007) proved to be efficient and accurate to implement the outflow boundary condition for complicated flows. Their method involves solving an additional vorticity equation near the outflow boundary for just a few grids into the computational domain. The resultant vorticity is then used to supply the required velocity values for the momentum equations.

In this work, a generally accepted practice is used, namely, the outflow boundary is assumed to be a fully developed flow. It is specified so that the prescribed value at this boundary has a minimum upstream influence on the inner flow field. For the outflow boundary, a zero gradient (homogeneous Neumann conditions) is used for all components except pressure.

The boundary condition for pressure at the outflow is set to hold hydrostatic equilibrium based on the flow depth at the outlet (Drikakis and Rider, 2005). For open channel flows, a flow depth is specified at the downstream side of the flow for the subcritical flow and the flow depth is calculated for the supercritical flow. For flows with gravity, a hydrostatic pressure profile is used

www.manaraa.com

for outflow pressure. Otherwise, a constant reference pressure is used for the whole outflow cross-section. Pressure for the ghost cell is linearly extrapolated from the inner cells.

3.6.5. Open

An open boundary is used when the top boundary is open to the air. An open boundary means that air could move in and out from the computational domain freely. The boundary conditions for an open boundary are numerically the same as an outflow boundary. At the open boundary, a zero-gradient boundary is used for all components except pressure. For the pressure, a constant pressure (atmosphere pressure), or zero gage pressure, is used at an open boundary.

3.6.6. Interface between two domains

In this work, the computational domain is split into two domains including a horizontal Main pipe domain and a vertical Manhole domain. An internal boundary exists between the two domains. A boundary condition is needed for numerical discretization purpose. For this type of boundary, a Dirichlet boundary condition is implemented. The values of the Dirichlet boundary are simply taken from the solution of the other domain and treated as known variables. Ghost cell values are obtained in a similar fashion.

For the momentum and VOF equations, they are solved explicitly. Hence, a Dirichlet boundary condition is only needed once in each time step. For the Pressure Poisson Equation, it is solved by a SOR iterative method. This requires that Dirichlet boundary conditions be implemented in each iteration. Therefore, communications between the two domains must be included. This is done by updating the ghost cell pressure values using the calculated results from the other domain in each SOR iteration.

3.7. Treatment of Advective terms

Advection-dominant flow problems tend to develop numerical oscillations near a discontinuity that cause the solution to be unstable. Special treatment must be taken in the discretization of the advective term to reduce the oscillations and keep the solution stable. One way to eliminate the oscillations is to implement a shock-capture or oscillation-free type of scheme.

Flux Correction Transport (FCT) was originally introduced by Boris and Book (1973) and Boris et al.(1975) to solve a one-dimensional advective equation. It was improved and extended to solve the multi-dimension advective equations by Zalesak (1979). As an improvement to the

www.manaraa.com

original FCT method, Zalesak (1979) used a different flux limiter and correction calculation procedure that is less diffusive. The improved FCT was shown to be able to restore physical peaks instead of smearing them.

The basic idea of FCT can be demonstrated by the following simple advective problem. The following equation

$$\frac{\partial Q}{\partial t} + \frac{\partial F}{\partial x} = 0 \tag{3.6.1}$$

is first solved using a lower-order scheme, such as a 1st-order upwind, for the advective term to obtain a stable intermittent solution. The discretization of the advective equation is

$$Q_i^r = Q_i^n - (F^L_{i+\frac{1}{2}} - F^L_{i-\frac{1}{2}})\delta t \tag{3.6.2}$$

where, $F^L_{i+\frac{1}{2}}$ is the flux at the east face of a control volume, and is calculated from a lower-order scheme. Then an advective flux $F^H_{i+\frac{1}{2}}$ is calculated using a higher order scheme, such as a QUICK scheme.

Following the calculation of the lower and higher order fluxes, an "anti-diffusive" flux F^A is calculated based on the difference between the higher-order and the lower-order fluxes.

$$F^A_{i+\frac{1}{2}} = F^H_{i+\frac{1}{2}} - F^L_{i+\frac{1}{2}} \tag{3.6.3}$$

The anti-diffusive flux is then corrected using a correction factor $C_{i+1/2}$ which is determined from a pre-defined flux limiter. The flux limiter technique used in FCT is critical. It assures that anti-diffusive flux is only applied to regions where no new extrema will be introduced. The correction factors could be estimated in two ways, the original Boris and Book method or the Zalesak (1979) method. Zalesak's method has been shown less diffusive and able to capture the physical peaks in smooth solution region.

It is well known that the first-order upwind type of lower-order schemes for advective terms is stable, but very diffusive, while higher order schemes are unstable. In FCT method, the lower order solution could be "corrected" to a higher order by adding just enough anti-diffusive flux. The resulted higher order solution is stable and also remains monotonicity near the discontinuity.

www.manaraa.com

The final value of Q^{n+1} is obtained from the lower order solution Q^r using the "corrected" anti-diffusive flux, CF^A. The computation of the final Q^{n+1} is shown here

$$Q_i^{n+1} = Q_i^r - (C_{i+1/2}F^A_{i+\frac{1}{2}} - C_{i-1/2}F^A_{i-\frac{1}{2}})\delta t \tag{3.6.4}$$

In recent years, it has been shown by several researchers that the numerical truncation errors or numerical diffusions introduced by the flux limiters in a FCT are very similar to a subgrid stress models in large-eddy simulations (Grinstein and Guirguis 1992; Fureby and Grinstein 1999, 2002; Rider and Moyce 2003). Hence FCT falls into the general family of the Implicit Large Eddy Simulation (ILES).

In this work, to calculate the momentum flux in the advective term, a 1st-order upwind scheme is used for the lower-order flux and a QUICK scheme is used for the higher-order flux. In both flux calculation, the mass at the control volume face was calculated at the exact location while the velocity at the control volume face was approximated using a 1st-order upwind or a QUICK scheme. This can be demonstrated in the calculation of the east face and north face of a control volume for the *x*- and *y*- momentum equation. Momentum fluxes for other faces can be estimated in a similar manner.

1st order upwind scheme (FOU)

x-momentum equation control volume

$$Momentum\ Flux|_{East} =$$

$$\bar{u}_{i+1,j}\bar{u}_{i+1,j} = \begin{cases} \bar{u}_{i+1,j}u_{i+1,j} & if\ \ \bar{u}_{i+1,j} < 0 \\ \bar{u}_{i+1,j}u_{i,j} & else \end{cases} \tag{3.6.5a}$$

$$Momentum\ Flux|_{North} =$$

$$\bar{v}_{i,j}\tilde{u}_{i,j} = \begin{cases} \bar{v}_{i,j}u_{i,j+1} & if\ \ \bar{v}_{i,j} < 0 \\ \bar{v}_{i,j}u_{i,j} & else \end{cases} \tag{3.6.5b}$$

y-momentum equation control volume

$$Momentum\ Flux|_{East} =$$

www.manaraa.com

$$\tilde{u}_{i,j}\bar{v}_{i,j} = \begin{cases} \tilde{u}_{i,j}v_{i+1,j} & if\ \ \tilde{u}_{i,j} < 0 \\ \tilde{u}_{i,j}v_{i,j} & else \end{cases} \tag{3.6.6a}$$

$$Momentum\ Flux|_{North} =$$

$$\tilde{v}_{i,j+1}\tilde{v}_{i,j+1} = \begin{cases} \tilde{v}_{i,j+1}v_{i,j+1} & if\ \ \tilde{v}_{i,j+1} < 0 \\ \tilde{v}_{i,j+1}v_{i,j} & else \end{cases} \tag{3.6.6b}$$

QUICK scheme

x-momentum equation control volume

$$\text{Momentum Flux}|_{\text{East}} =$$

$$\bar{u}_{i+1,j}\bar{u}_{i+1,j} = \begin{cases} \bar{u}_{i+1,j}(\frac{6}{8}u_{i+1,j} + \frac{3}{8}u_{i,j} - \frac{1}{8}u_{i+2,j}) & if\ \ \bar{u}_{i+1,j} < 0 \\ \bar{u}_{i+1,j}(\frac{6}{8}u_{i,j} + \frac{3}{8}u_{i+1,j} - \frac{1}{8}u_{i-1,j}) & else \end{cases} \tag{3.6.7a}$$

$$\text{Momentum Flux}|_{\text{North}} =$$

$$\bar{v}_{i,j}\tilde{u}_{i,j+1} = \begin{cases} \bar{v}_{i,j}(\frac{6}{8}u_{i,j+1} + \frac{3}{8}u_{i,j} - \frac{1}{8}u_{i,j+2}) & if\ \ \bar{v}_{i,j} < 0 \\ \bar{v}_{i,j}(\frac{6}{8}u_{i,j} + \frac{3}{8}u_{i,j+1} - \frac{1}{8}u_{i,j-1}) & else \end{cases} \tag{3.6.7b}$$

y-momentum equation control volume

$$\text{Momentum Flux}|_{\text{East}} =$$

$$\tilde{u}_{i,j}\bar{v}_{i,j} = \begin{cases} \tilde{u}_{i,j}(\frac{6}{8}v_{i+1,j} + \frac{3}{8}v_{i,j} - \frac{1}{8}v_{i+2,j}) & if\ \ \tilde{u}_{i,j} < 0 \\ \tilde{u}_{i,j}(\frac{6}{8}v_{i,j} + \frac{3}{8}v_{i+1,j} - \frac{1}{8}v_{i-1,j}) & else \end{cases} \tag{3.6.8a}$$

$$\text{Momentum Flux}|_{\text{North}} =$$

www.manaraa.com

$$\tilde{v}_{i,j+1}\tilde{v}_{i,j+1} = \begin{cases} \tilde{v}_{i,j+1}(\frac{6}{8}v_{i,j+1} + \frac{3}{8}v_{i,j} - \frac{1}{8}v_{i,j+2}) & if \ \ \tilde{v}_{i,j+1} < 0 \\ \tilde{v}_{i,j+1}(\frac{6}{8}v_{i,j} + \frac{3}{8}v_{i,j+1} - \frac{1}{8}v_{i,j-1}) & else \end{cases} \quad (3.6.8b)$$

3.8. Shuman Filter

A Filter is applied to the auxiliary velocity field after solving momentum equations to treat the "Cell-Re" and aliasing problems. Filtering is similar to the mollification post-process used in an image processing field which convolutes an irregular solution to a smooth one. The particular type of filter used in this study is a Shuman filter, originally developed by Shuman when he studied atmosphere data (Shuman 1957). This filter convolutes the velocity field by providing additional dissipation needed to damp aliasing (McDonough 2008). The Shuman filter is a discrete solution operator that is fairly easy to implement.

In a two-dimensional velocity field, the velocity component *u* and *v* is filtered separately. The Shuman filter for velocity *u* component can be implemented as

$$\bar{\bar{u}}_{i,j} = \frac{u_{i-1,j} + u_{i,j-1} + \beta u_{i,j} + u_{i+1,j} + u_{i,j+1}}{4 + \beta} \quad (3.6.9)$$

where

β is the filter parameter.

$\bar{\bar{u}}_{i,j}$ is the filtered velocity *u*

$u_{i-1,j}, u_{i,j-1}, u_{i,j}, u_{i+1,j}, u_{i,j+1}$ are the velocity *u* in five stencils used in the filtering process.

The selection of the filter parameter β is important to the results. The small the filter parameter is, the more dissipation will be added to the solution which results in a more "smeared" solution. It has been noticed that a filter parameter that is too small (such as less than 5000) often significantly slows down a wave front. Unfortunately, there is no existing formula to estimate an optimal filter parameter value. The section of the filter parameter is a trial and error process. A

www.manaraa.com

rule of thumb is to pick the highest possible β while still maintaining a stable solution. In this work, the same filter value is used to filter both velocity *u* and *v* unless specifically stated.

The filtering process could be performed to density and viscosity as well. But it appears in the numerical experiments performed in this study that filtering physical property does not improve the stability of the solution noticeably. Hence in this work, density and viscosity are not filtered.

3.9. Domain Decomposition

In this work, the physical domain contains two rectangular shapes: a horizontal main pipe and a vertical manhole riser. Naturally, the physical domain is decomposed into two rectangular computational domains. The two domains share a common internal boundary, i.e., the bottom boundary of the manhole riser. The domain decomposition is shown in Fig. 3.13.

There are two advantages of a domain decomposition strategy. First, domain decomposition provides potentials for parallel computing, which often cuts the total computing time significantly. Additionally, domain decomposition reduces the size of the coefficient matrix for an iterative solution procedure, such as SOR, due to the resulted smaller sub-domains. A smaller domain is associated with a smaller spectral radius, which indicates a faster SOR convergence.

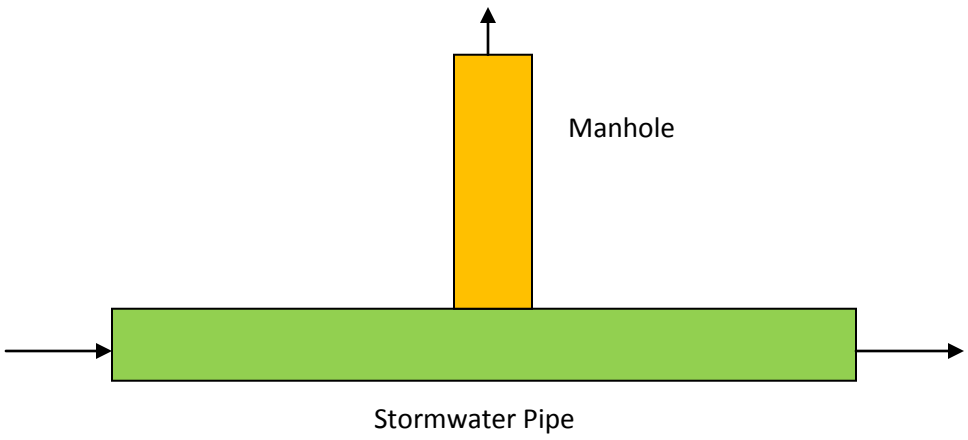

Figure 3.13 Domain decomposition.

www.manaraa.com

Communication cost is always a concern in domain decomposition and parallel computing. In this work, the momentum equation and the VOF equation are solved explicitly. Hence no communication is necessary between the two domains during each time step. However, for the Pressure Poisson Equation, an iterative procedure, SOR, is used. The convergence and stability of an iterative method on multi-domain always raises questions.

The approach used in this study is based on a theory developed by Schwarz (Schwarz 1870). As proved by Schwarz, an iterative procedure of an elliptical problem would converge when the domain is divided into two (or more) regular shapes, as long as the boundary conditions required by one subdomain are determined from the solution in the other subdomain (McDonough 2007). Following this theory, the pressure values at the common boundary are communicated at each SOR iteration. This is done by implementing a Dirichlet boundary condition for the pressure at the internal boundary. In the solution procedure, the PPE is solved in a main pipe manhole sequence. Pressure in the main domain was calculated first using ghost cell values supplied by the manhole domain in the previous SOR iteration. Then the boundary pressures are updated and used as a Dirichlet boundary condition in the computation of the manhole domain pressure.

Three arrays are defined in the code to exchange velocity, volume flux and pressure between the two domains, UEXCH, VEXCH, FEXCH, PEXCH. The inflow volume flux at the bottom boundary of the manhole domain is calculated based on the outflow volume flux in the main domain.

3.10. Computation Procedure

The overall algorithm can be summarized as follows. Assuming *n* time steps have been calculated, At time step *n+1*,

i. Reconstruct the interface using a discrete volume fraction distribution. Solve VOF equation to obtain a new volume fraction distribution.

ii. Update density and viscosity values.

iii. Solve Momentum equations without pressure explicitly to obtain intermittent velocity field $\hat{u}$ and $\hat{v}$.

www.manaraa.com

iv. Filter intermittent velocity field $\hat{u}$ and $\hat{v}$, if necessary.

v. Solve Pressure Poison Equation iteratively using point SOR.

vi. Project intermittent velocity field to the divergence-free velocity field *u* and *v*.

www.manaraa.com

CHAPTER 4 MODEL VALIDATIONS

The integrity and accuracy of the numerical model need to be validated extensively prior to applying to the complicated geyser simulation. The numerical model developed in this work contains two solvers that are coupled together, namely, the two-dimensional incompressible Navier-Stokes solver and the two-phase flow VOF solver. The validation of a coupled model is complicated. To conduct the validation, the first step is to decouple the two solvers and validate the individual model. The validation process is performed at several levels, starting with simple flow problems. Following successful validation in the simple flow problems, the validation is carried out in more advanced flows.

The two-dimensional two-phase numerical model was extensively tested to ensure that the implementation of the solution procedure and boundary conditions performs correctly. The different levels of the validation process are summarized as follows:

i. The single-phase two-dimensional Navier-Stokes solver is first tested. The Navier-Stokes solver is used to solve single phase flow problems which have analytic solutions or well-established numerical results. The validation cases include the classic lid-driven cavity problem and parallel plate flows that are driven either by a moving upper wall (Couette Flow) or by a pressure gradient (Poiseuille Flow).
ii. The next step is to validate the two-phase flow VOF model. This is done by decoupling the interface reconstruction and interface advancing algorithm from the Navier-Stokes computation. In these simulations, simple objects are advected and deformed in a VOF model without solving Navier-Stokes equations. A divergence-free velocity field is pre-defined for the whole domain instead of computing from the Navier-Stokes Equations. This validation process is often called a “static validation” since only the interface is tracked and no flow dynamics is solved. In this step, a series of interface evolution tests are performed including simple object advection, rigid object rotation, shear flow and reverse shear flow.
iii. Following the validation of both Navier-Stokes solver and the VOF model, the two solvers are combined and applied to benchmark free surface flows with either known analytical solutions or well-established experimental data. This validation is called a “dynamic validation” because the velocity field is solved as part of the solution process and interface advancing. Test cases performed in this step include Rayleigh–Taylor

www.manaraa.com

instability problem, horizontal tank acceleration, dam break wave and open channel film flow.

iv. The last step of the validation process is to test the code over multi-domains by adding a manhole domain. A single-phase Poiseuille problem is tested to check the performance of the multi-domain simulation.

Following the validations, the numerical model is then applied to solve real life engineering problems, such as mixed flows, open channel surge and pressurization process.

In this numerical study, turbulence simulation is not included. All the test cases in this study are assumed to be non-turbulent flow, even if the Reynolds number is large. It is aware that in mixed flow and geyser simulations, turbulence inevitably occurs as flow field gets disturbed and becomes violent. However, this study is a first step in numerical simulation of mixed flows by solving two-phase Navier-Stokes Equations. It lays the groundwork for future, more complete numerical simulations. For this reason, only major components in mixed flows and geysers are included in the numerical model in this work.

4.1. Two-dimensional Navier-Stokes Solver Validation

As stated above, the first step of the validation process is to validate the single-phase Navier-Stokes equation solver. The validation problems in this step include the lid-driven cavity problem and two parallel plate flow problems that are driven either by a moving upper wall (Couette Flow) or a pressure gradient (Poiseuille Flow).

4.1.1. Lid Driven Cavity

Lid driven cavity problem is a benchmark problem for validating new Navier-Stokes code or new algorithms due to its simple geometry and straight forward boundary conditions. Extensive numerical studies have been performed on this problem. Numerical results published by Ghia, and Shin (1982) have been widely used as benchmark data for comparison of new numerical codes.

In this problem, the flow is in a square cavity of unit width. The cavity contains four rigid walls, as shown in Fig. 4.1. The initial system is at rest. At $t = 0^+$, the top lid starts moving to the right with a unit velocity $U_{wall}=1.0\ m/s$. The flow inside of the cavity reaches a steady state after some time. In this simulation, density of the flow is $1.0\ kg/m^3$ and viscosity is $0.001\ kg/m{\cdot}s$. The flow

www.manaraa.com

could be characterized by Reynolds number defined as $RE = \frac{U_{wall}}{\nu} L$, where L is the characteristic length of domain. In this case, *L=1.0 m*, which results in a Reynolds number of *1000*.

The non-slip wall boundary condition is used for all walls. A zero gradient Neumann boundary condition is used for the pressure. In this problem, gravity is ignored. A reference pressure point is provided in addition to the pure Neumann boundary condition for the Pressure Poisson equation to "pin" the solution. The selection of a reference pressure point in this problem is arbitrary and does not affect the velocity field computation. The reference pressure point is selected to be the middle point adjacent to the bottom wall. The reference pressure value was set to be zero.

A Reynolds number of 1000 case (*RE=1000)* is tested to compare the numerical results with the data published by Ghia et al. (1982). A grid size of *128* x *128* is used for this simulation so that the numerical results are comparable to Ghia's results. Time step size is $5x10^{-4}$ *s*.

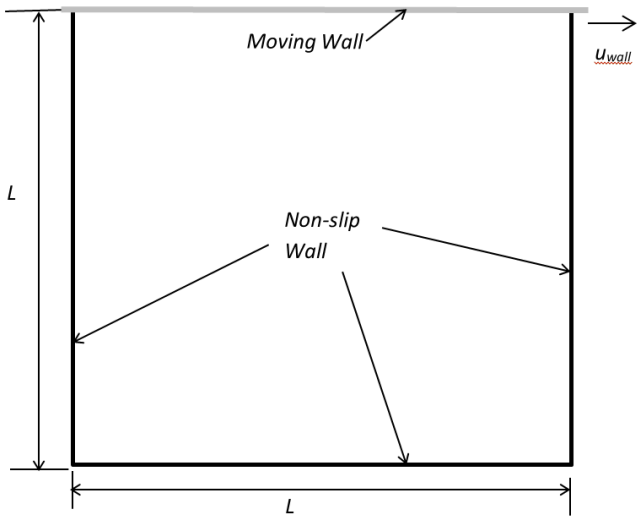

Figure 4. 1 Lid-driven cavity computational domain.

The numerical results are shown in Figs. 4.2 and 4.3. The velocity profile for *u* at *x*=0.5 and *v* at *y*=0.5 are plotted along with the data published by Ghia et al. (1982). It can be seen that the numerical predictions from this model match very well with Ghia's. Fig. 4.4 plots the velocity

www.manaraa.com

and pressure fields. Figure 4-5 plots the streamline in the flow filed. It can be seen from Fig. 4.5 that the two vortexes at the lower corner of the domain are predicted correctly by this numerical model.

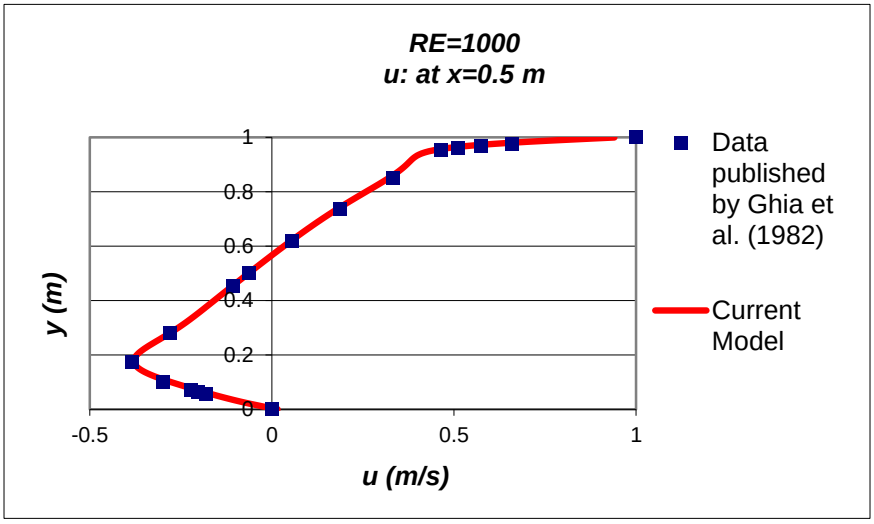

Figure 4. 2 Velocity u profile at x=0.5.

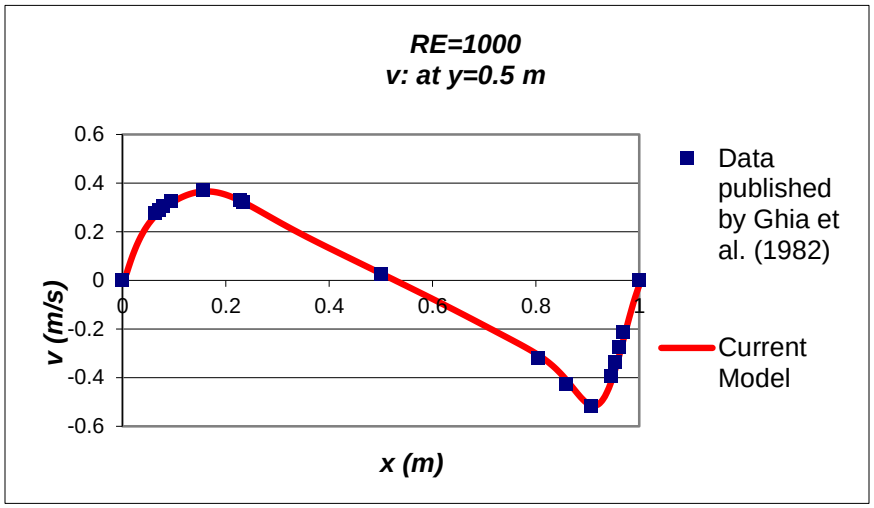

Figure 4. 3 Velocity v profile at y=0.5.

www.manaraa.com

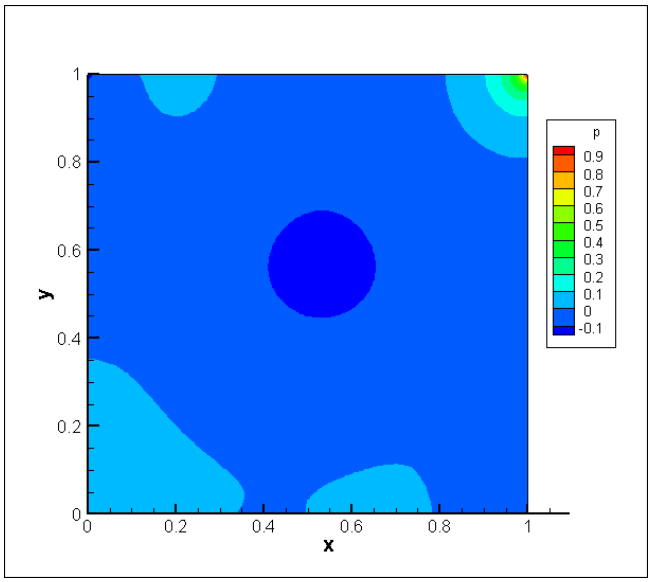

Figure 4. 4 Lid Driven Cavity simulation pressure (*p*) field (*RE=1000*).

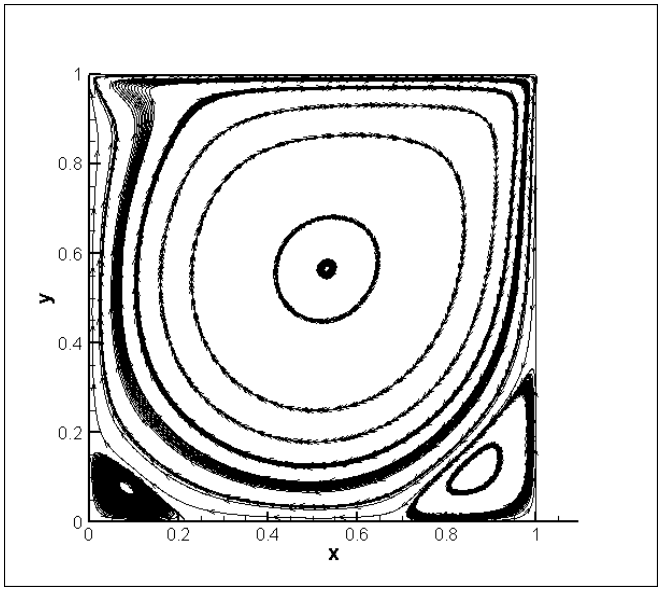

Figure 4. 5 Lid Driven Cavity simulation streamline (*RE=1000*).

For flow problems without analytical solutions, grid convergence test is often carried out to check the convergence performance of the code. In this study, a grid convergence test is performed for a

www.manaraa.com

lower Reynolds number. In the Grid Convergence tests, the top wall speed is U_{wall}=*1.0 m/s*. The density of the flow remains to be *1.0 kg/m*^{3} while the viscosity is *0.01 kg/m·s*. This results in a Reynolds number *RE=100.* The grid convergence test is carried out in three sets of grid size including *20* x *20, 40* x *40* and *80* x *80.* In the grid convergence test, the QUICK scheme detailed in Section 3.7 is used to discretize the advective terms. The grid convergence rate for velocity component *u* could be calculated following the formula

$$GCT = \frac{u^{4h} - u^{2h}}{u^{2h} - u^{h}} \tag{4.1}$$

where *h* is the finest grid size, and is the *80* x *80* grid in this test. Results of the grid convergence test for *RE=100* case are included in Table 4.1. It can be seen from Table 4.1 that a 2nd-order grid convergence rate (*GCT =4.0*) was reached. In some instances a convergence rate higher than 2nd-order is observed. This is believed that QUICK can reach 3rd-order accuracy (*GCT=8.0*) for smooth solutions.

Table 4.1 Lid driven cavity grid convergence rate test (*RE=100*).

		Grid Convergence Rate (GCT)		
x(m)	*y(m)*	*u*	*v*	*p*
0.1	*0.1*	*3.94*	*3.95*	*1.78*
0.2	*0.8*	*3.19*	*4.83*	*3.95*
0.4	*0.6*	*4.82*	*4.79*	*3.90*
0.5	*0.5*	*4.60*	*3.00*	*3.71*
0.5	*0.9*	*4.58*	*4.67*	*4.03*
0.6	*0.4*	*4.44*	*4.52*	*3.11*
0.7	*0.95*	*11.26*	*3.10*	*4.29*
0.8	*0.8*	*4.05*	*4.08*	*3.68*
0.9	*0.1*	*37.80*	*7.88*	*2.73*

4.1.2.Pressure Driven Parallel Plate Flow - Poiseuille Flow

Pressure driven flow between two parallel plates is also known as Poiseuille flow, which has an analytical solution. The analytical solution is derived from the two-dimensional Navier-Stokes equations by setting the velocity gradients along *x*-direction to be zero and the vertical velocity

www.manaraa.com

component to be zero. Velocity at both upper and lower plate boundaries are zero due to non-slip wall boundary conditions. Poiseuille flow is driven by a pressure gradient. The analytical velocity profile has a parabolic distribution in the *y*-direction. The analytical pressure gradient can be written in the following form

$$\frac{dp}{dx} = -\frac{8v}{D^2}u_{max} \tag{4.2}$$

where $\frac{dp}{dx}$ is the pressure gradient between the inlet and outlet, v is viscosity, u_{max} is the maximum velocity at the cross section, and D is the distance between the two plates, as shown in Fig. 4.6. Likewise, the velocity profile is determined if pressure gradient is known, by

$$u(y) = \frac{(y^2 - yD)}{2v}\frac{dp}{dx}; v = 0 \tag{4.3}$$

where y is the distance measured from the bottom plate.

In this simulation, the initial flow is at rest. A non-slip wall boundary is used for both top and bottom plates.

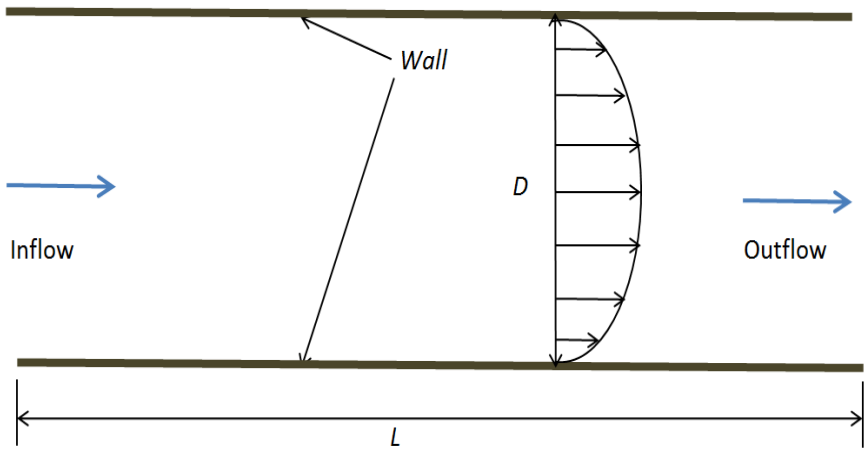

Figure 4. 6 Pressure driven parallel plate flow.

www.manaraa.com

This problem can be tested in two ways depending whether velocity inflow or pressure inflow boundary is prescribed at the inlet. For a velocity inflow case, a parabolic inflow profile is prescribed at the inlet while the pressure drop is calculated and compared with the analytical results. For the pressure inflow case, Dirichlet boundary conditions for the pressure are specified at both inlet and outlet. The velocity profile at the inlet will be calculated. In this study, a velocity inflow type is tested, where an analytical velocity inflow profile is provided and the pressure drop is calculated. The pressure at the outflow boundary is specified with a zero value.

The fluid in this simulation has a viscosity value of *0.01 kg/m·s* and a density value of *1.0 kg/m*^{3}. The dimension of the domain is *L* x *D=1.0 m* x *0.1m*, with a mesh size of *40* x *20*. Time step is $\delta t = 0.001s$ for this grid size. The simulation is run until a steady-state is reached. The steady state convergence criterion for steady-state is 10^{-6} for both velocity and pressure. The maximum velocity is *1.0 m/s*, with a corresponding theoretical pressure gradient of

$$\frac{dp}{dx} = -\frac{8 \cdot 0.01 \frac{kg}{m} \cdot s}{(0.1\ m)^2} \cdot 1\ m/s = -8\ pa/m$$

Figure 4.7 plots the velocity vector and pressure filed in this simulation. As expected, the pressure drop in the flow direction is linear and the velocity vector is parallel to the plates. The pressure gradient calculated by the numerical model is *7.97 pa/m*. The difference between the theoretical and numerical predicted pressure is

$$\frac{\|7.97 - 8.0\|}{\|8.0\|} = 0.375\%$$

www.manaraa.com

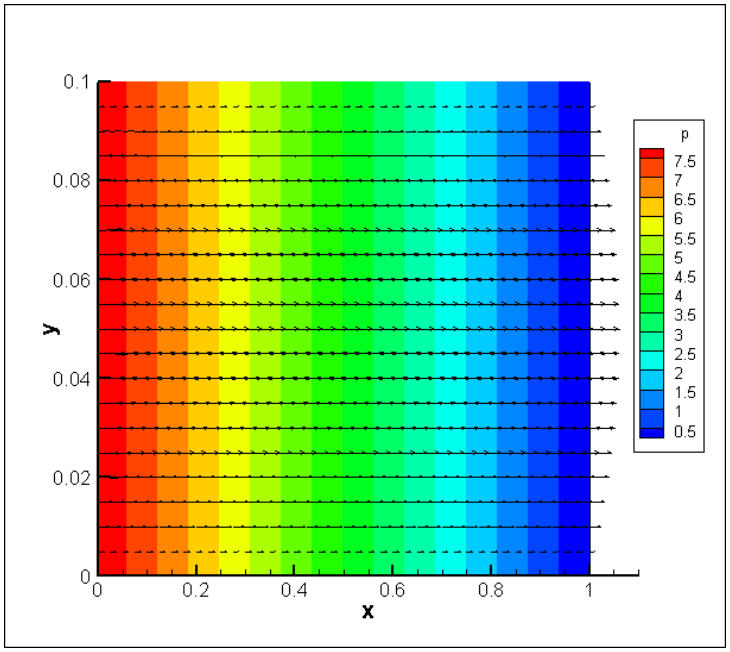

Figure 4. 7 Velocity vector and pressure distribution in Poiseuille flow simulation.

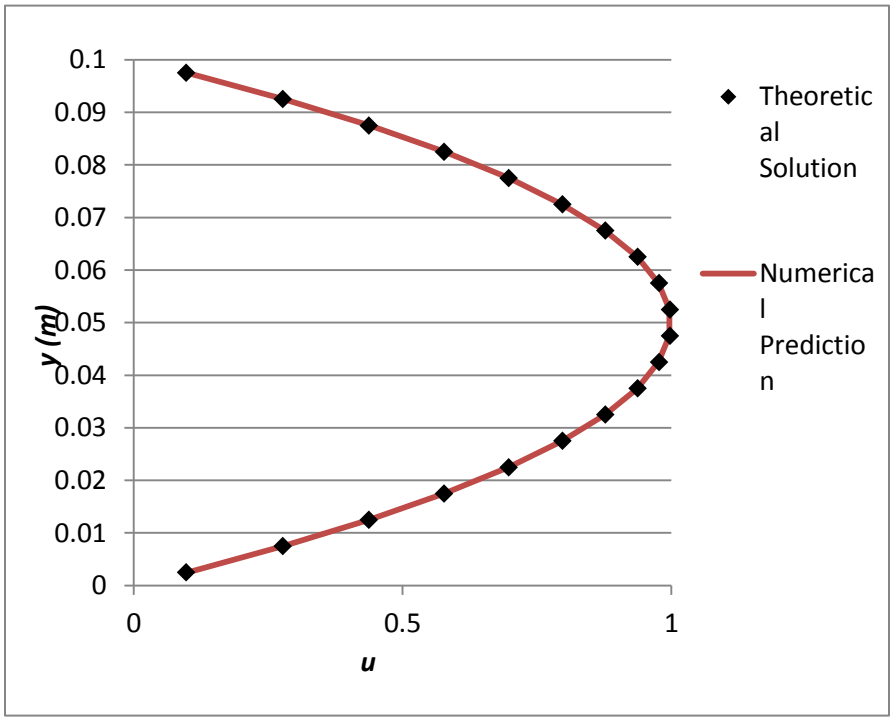

Figure 4. 8 Velocity profile at the outlet in Poiseuille flow simulation.

www.manaraa.com

Figure 4.8 plots the velocity profile from the numerical model at the outlet and the theoretical parabolic velocity profile. It could be seen that velocity at the outlet remains a parabolic profile as expected. The numerical solution matches the analytical result very well.

4.1.3. Upper Plate Driven Parallel Plate Flow – Couette Flow

Couette flow is another type of flow between two parallel plates. This type of flow also has an analytical solution. The computational domain of a Couette flow is the same as a Poiseuille flow. But in Couette flow, the flow is driven by the movement of the upper lid. The initial flow is at rest. At $t=0+$, the upper lid starts moving to the right with a unit velocity, namely, $u_{wall} = 1.0\ m/s$. The analytical velocity profile between the two plates is linear along the y direction, as derived from a two-dimensional Navier-Stokes Equations by setting the velocity gradients along x-direction to zero and normal velocity component to zero. Both plates are non-slip walls. Hence, the horizontal velocity at the upper lid is the same as the lid speed, u_{wall}, and the horizontal velocities at the lower plate is zero, as demonstrated in Fig. 4.9.

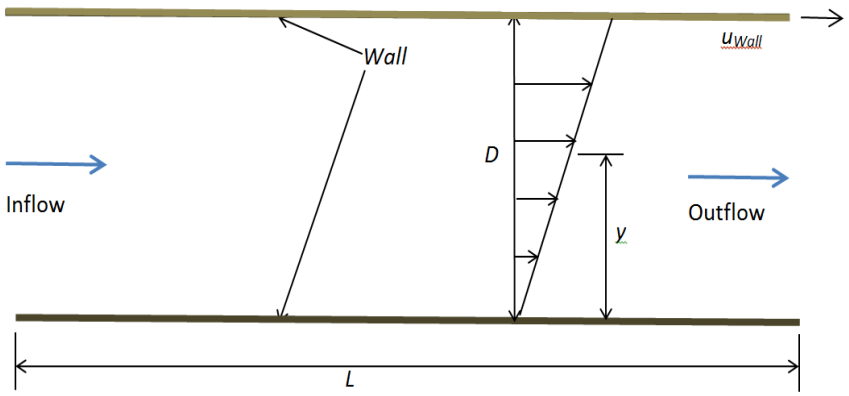

Figure 4. 9 Upper plate driven parallel plate flow.

The analytical velocity distribution derived from Navier-Stokes Equations is

$$u = \frac{u_{wall}}{D} y; v = 0 \tag{4.4}$$

www.manaraa.com

where *y* is the distance measured from the bottom plate and D is the distance between the two plates, as depicted in Fig. 4.9.

In the numerical model, the initial flow is at rest. The non-slip wall boundary is used for top and bottom plates. The upper lid velocity is *1.0 m/s*. At the inflow boundary, a zero-gradient boundary condition is prescribed for the velocity. The pressure at both inflow and outflow are zero.

The fluid in this simulation has a viscosity of $0.01\ kg/m{\cdot}s$ and a density of $1.0\ kg/m^3$. The dimension of the domain is L x $D=1.0\ m$ x $0.1m$, with a mesh size of *40* x *20*. Time step is set to be $\delta t = 0.005s$ for this grid size. The simulation is run until a steady-state is reached. The convergence criterion for steady-state is 10^{-6} for both velocity and pressure. Figure 4.10 compares the computed velocity profile with the analytical solution. The velocity profile is linear in the vertical direction, which is consistent with the analytical solution.

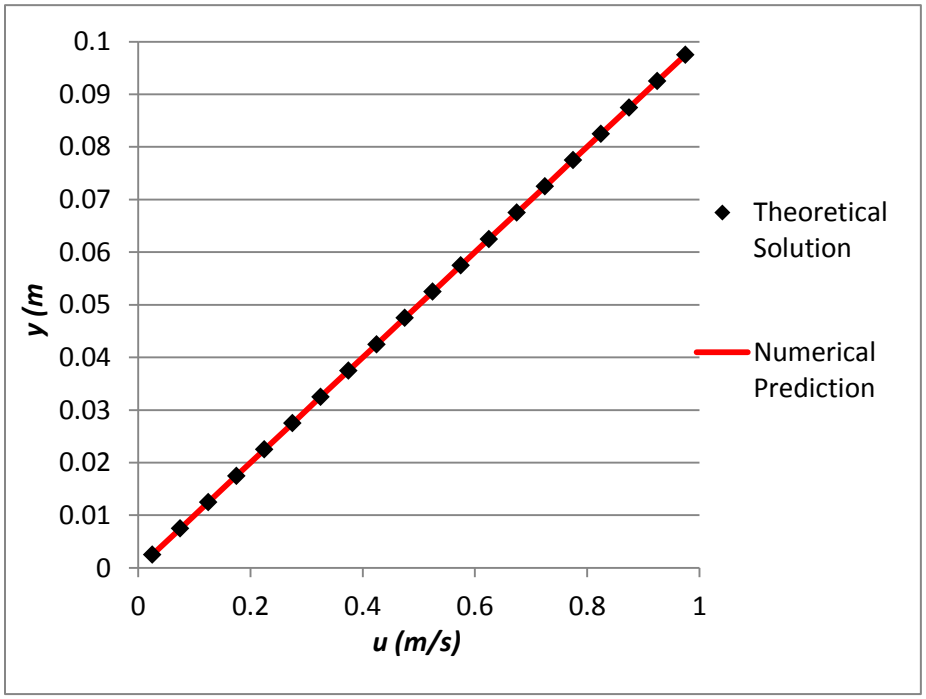

Figure 4. 10 Velocity profile at outlet in Couette flow simulation.

www.manaraa.com

4.2. Validation of two-phase VOF model

The next step is to validate the two-phase flow VOF model. This is done by decoupling the interface reconstruction and interface advancing algorithm from the Navier-Stokes computation. A divergence-free velocity field is pre-defined for the whole domain. In this step, a series of interface evolution tests are performed including simple object advection, rigid object rotation, shear flow and reverse shear flow.

4.2.1. Simple Object Advection

To measure the performance of the proposed VOF advection algorithm, a series of simple object advection tests are carried out. Massless markers are initially placed in each cell and advected with the pre-defined velocity field. Final locations of the markers are calculated in a Lagrangian way and used as the "exact" solution for the tested problem. Locations of markers can be directly integrated from the following ordinary partial differential equation

$$\frac{dx}{dt} = u \; ; \frac{dy}{dt} = v \tag{4.5}$$

where (x,y) are the coordinates of markers.

The computational domain is a *10 m* x *10 m* square with origin at (*0, 0*) in all cases. The mesh size is *200* x *200* for all simulations. The initial location of each simulated object is described below.

- A square with an angle of *26.57* º and a width of *2.0m* is initially centered at (*3.75m, 3.75m*). The time step is *0.005s*. The specified velocity field is (*u, v*) = (*1.0m/s, 1.0m/s*). At time *t = 2s* (after *400* time steps), the center of the circle travels to (*5.75m, 5.75m*).
- A hallow square aligned with the coordinates is initially centered at (*4.0m, 4.0m*) with a width of *2.0m*. The time step is *0.005s*. The specified velocity field is (*u, v*) = (*0.8m/s, 0.8m/s*). At time *t = 2s* (after *400* time steps), the center of the circle travels to (*5.6m, 5.6m*).

Final locations of numerical predictions and exact solutions are shown in Fig. 4.11. Since the velocity field is uniform, there is no shear stress or any other forces exerted on the objects. As a result, the objects are expected to advect to the analytical locations without any deformation. The shaded areas represent the exact solutions while the red triangle represents the numerical solutions. It could be seen that the numerical solutions match the theoretical solutions well, and

www.manaraa.com

both mass and shape are conserved very well. This comparison shows that the VOF solver is capable of accurately advecting objects without noticeable smearing or deforming.

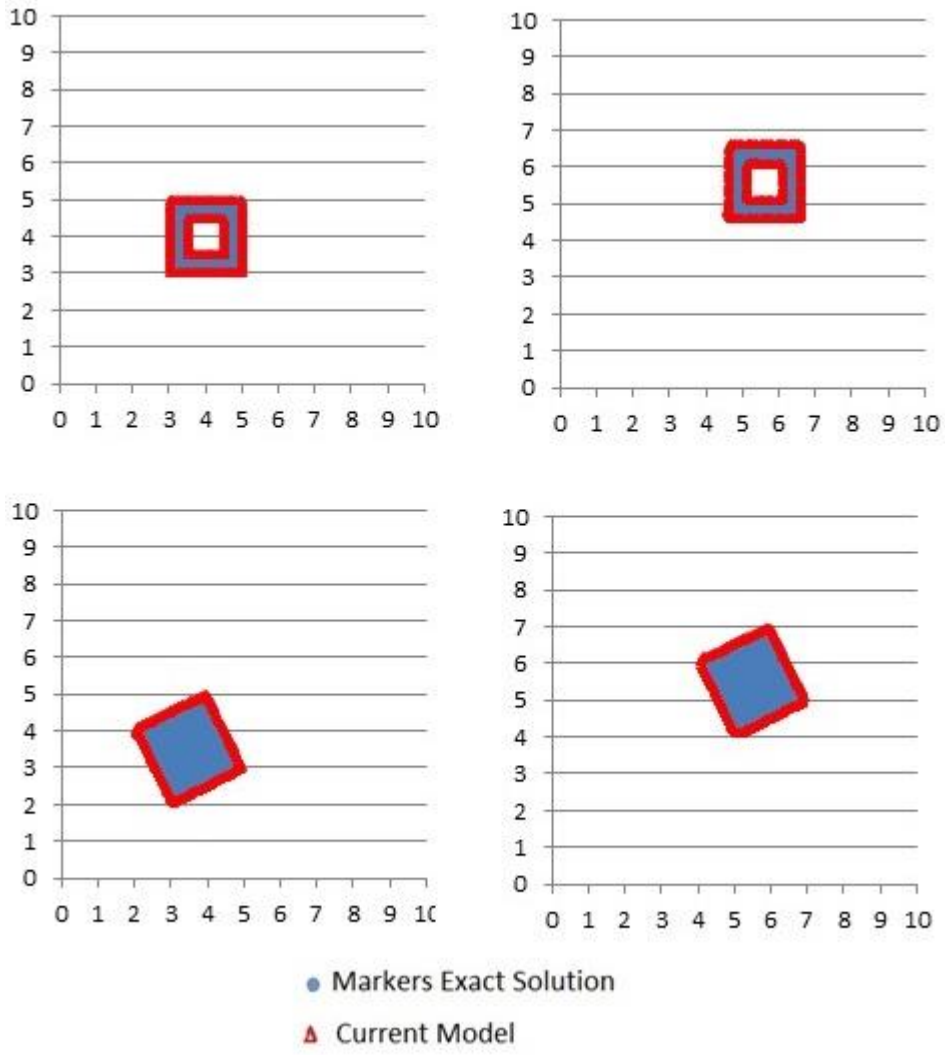

Figure 4. 11 Simple object advection at initial time (left) and time step *200* (right).

4.2.2.Rigid Body Rotation

Additional tests are performed to examine the ability to advance an interface by the VOF solver. This validation case includes rotating a rigid slotted disk around a center with a constant angular velocity field, known as Zalesak's rotating slotted disk problem (Zalesak, 1979). A good

www.manaraa.com

evolution scheme is expected to adequately preserve the disk geometry without smearing the sharp corners.

The computation domain is *4.0m* x *4.0m* square on a mesh size of *200* x *200*. The longest direction of the circle contains *50* cells and the slot contains *6* cells, as shown in Fig.4.12. The axis of the rotation center is at (*2.0m*, *2.0m*) and the circle center is initially at (*2.0m*, *2.7 m*). The angular velocity is set to be *0.5rad/sec* at the center of the initial circle so that the disk can return to its original position at every *2512* time units. In the initial state, the slot is facing downside. The time step is *0.01 s*. The numerical results at time step *1256* and *2512* are shown in Figs. 4.12 and 4.13, with the initial condition in the background. It can be seen that after 1256 time steps, the slot is facing upside and after *2512* time steps, the slot returns to the initial location without any noticeable smearing.

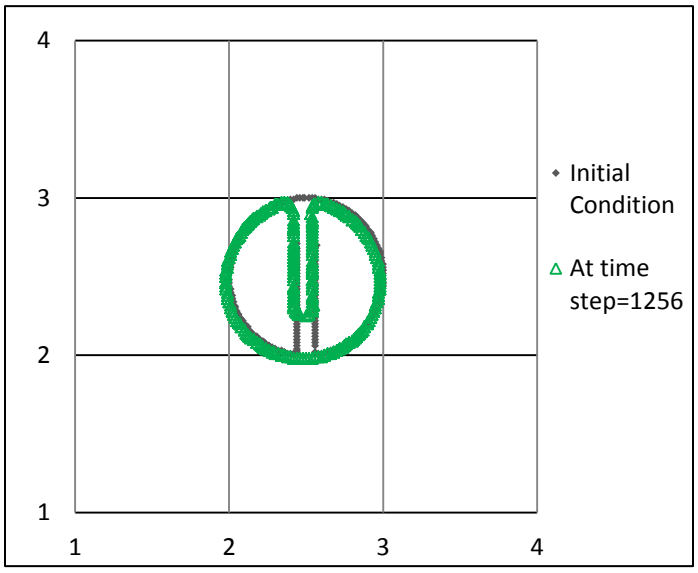

Figure 4. 12 Solid body at initial time and time step *1256*.

www.manaraa.com

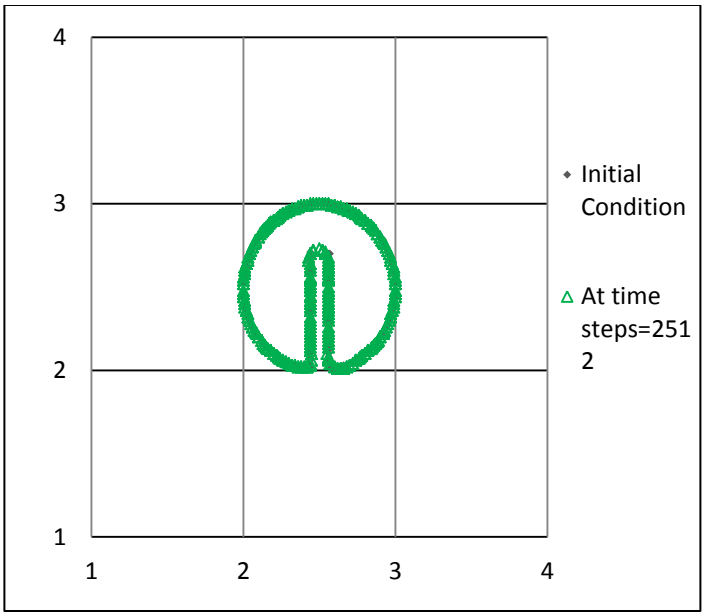

Figure 4. 13 Solid body rotation test at time step and *2512*.

4.2.3.Forward Shearing Flow Problem

According to Kothe and Rider (1996), simple advection and rotation tests by themselves are not sufficient to test the integrity of volume tracking methods because there is no topological change in simple object advection tests. In real problems, interface deformation, such as in wave breaking, occurs frequently. One of the features of VOF interface tracking method is the capability to simulate complicated interface topology changes such as breaking, stretching and merging. To check the performance of the VOF model handling these complicated interface changes, a shearing flow test is performed. In this test, a single vortex is imposed in a velocity field defined by the following stream function

$$\Psi = \frac{1}{\pi} sin^2(\pi x)\, sin^2(\pi y) \tag{4.6}$$

and $u = -\delta\Psi/\delta y$ and $v = \delta\Psi/\delta x$.

The computational domain is a unit square. A circle with a radius of *0.15m* is initially centered at (*0.5 m, 0.75 m*), as shown in Fig 4.14. The grid size is *166* x *166*. The time step is *0.006s*. The circle is deformed by a swirling vortex. With the circular object is placed in this field, the vortex stretches and spirals around the center of the circle. Massless markers are placed within each cell

www.manaraa.com

and move with the pre-defined velocity field. Figure 4.15 shows the numerical result and the exact solution at *t=3s*. It can be seen that the numerical result matches the theoretical result well.

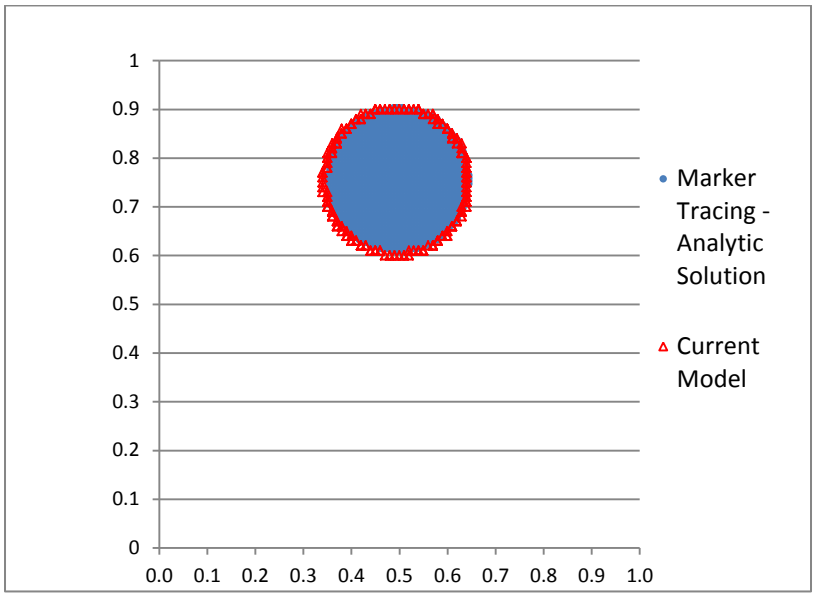

Figure 4. 14 Shearing flow at initial time.

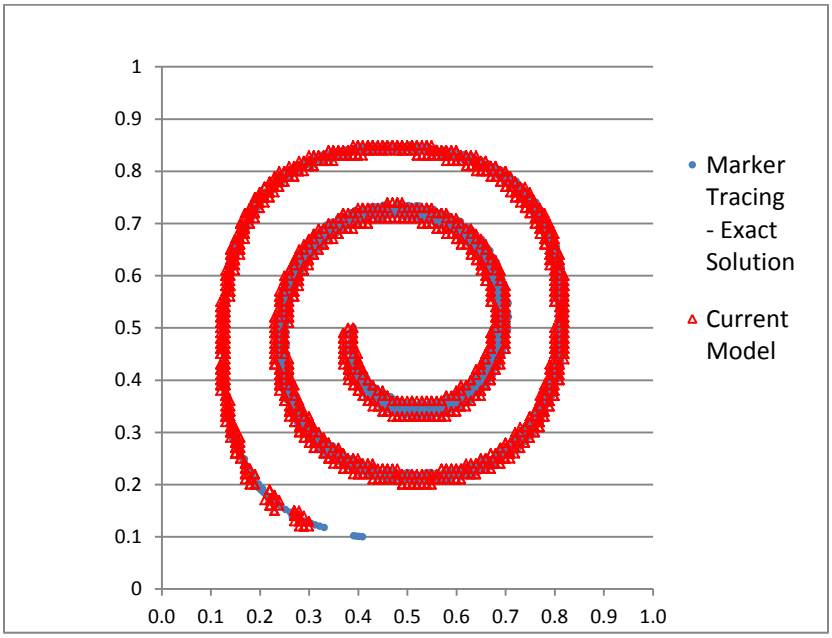

Figure 4. 15 Shearing flow at *t = 3.0 s*.

www.manaraa.com

4.2.4. Backward Time Marching Shearing Flow Problem

This problem is to integrate the numerical solution from the previous test case (forward shearing flow problem), as shown in Fig. 4-15, for an additional *3s*, but reversing the sign of the velocity field. This is a backward process of the previous forward shearing flow problem. Theoretically, the shape of the interface should return to the original circle configuration.

The numerical results are shown in Fig. 4.16. It can be seen from the figure that the VOF code performs fairly well with some minor stretches. This result agrees with the findings by Rudman (Rudman, 1997) when he compared the different VOF reconstruction methods.

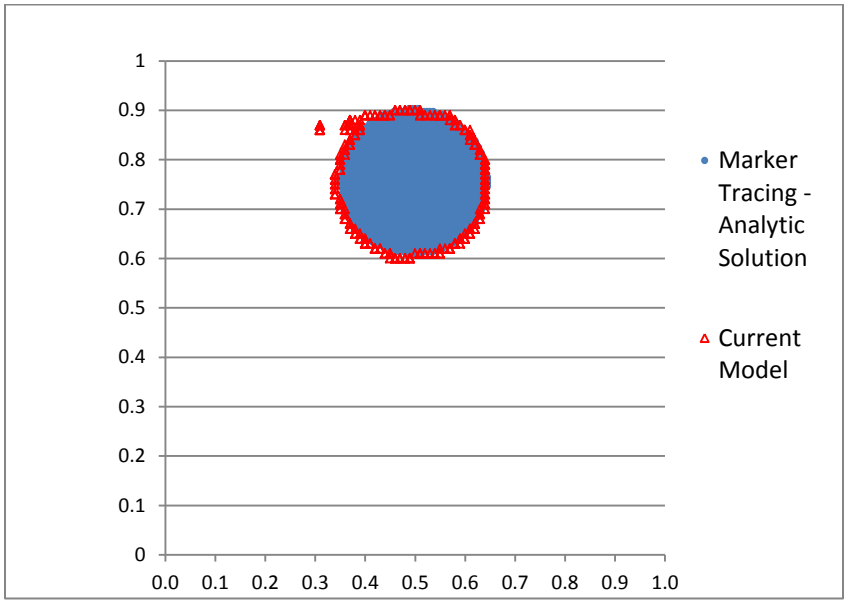

Figure 4. 16 Reverse shearing flow at $t = 3.0\ s$.

4.3. Two Domain Simulations

As stated in the introduction, the key feature of this study is the dynamic two-phase simulation in the vertical manhole. In this section, the multi-domain algorithm is tested using a single-phase Poieulle flow problem.

www.manaraa.com

In this case, a horizontal pipe flows full with a manhole outlet that forms a "T" shape joint. The fluid simulated is a hypothetical flow with a density of *10 kg/m*^{3} and a viscosity of *0.01 kg/m·s*. A velocity inflow boundary is used at the inlet. The velocity profile is prescribed in a way such that the distribution follows a Poiseuille flow. The outflow boundary condition is applied at the main pipe outflow. In this simulation, gravity is ignored. A zero pressure is specified at the outlet of the main pipe as well as the outlet of the manhole domain. A non-slip wall boundary is used for all walls in both domains.

The setup and boundary conditions are shown in Fig. 4.17. The domain sizes for the main pipe and manhole are *4.0m* x *0.5m* and *0.1m* x *2.0m*, respectively. The grid size is *320* x *80* for the main pipe domain and *8* x *320* for the manhole domain. The center of the manhole is located at *x = 0.55 m*.

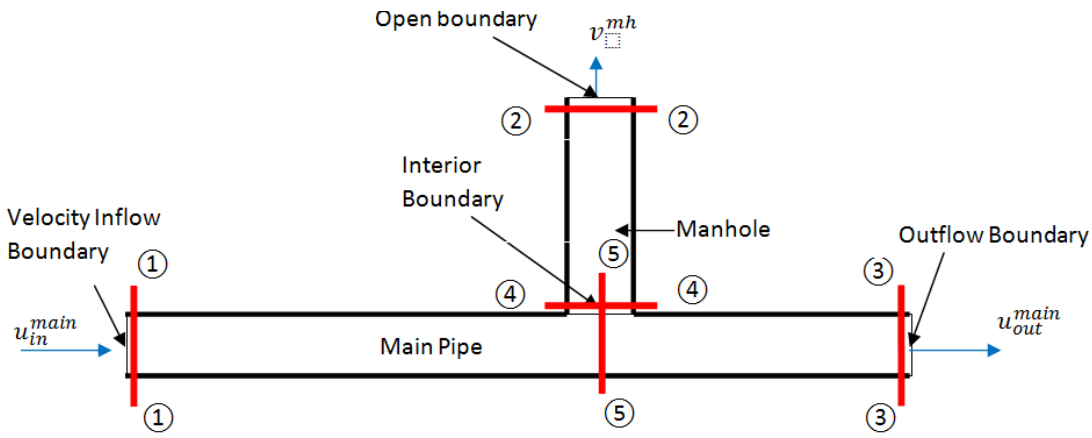

Figure 4. 17 Problem setup and boundary conditions.

When the flow reaches steady-state, a Poiseuille velocity profile should be observed at the outlet of both main and manhole pipes, provided that the distance between the inlet and outlet is long enough for the flow to reach a fully-developed state. The flow in both pipes are driven by a pressure gradient. At the outlets, the pressures are set to be the same, i.e., atmosphere pressure (zero gauge pressure). The analytical velocity profile can be derived based on the continuity equation and the Poiseuille flow theory in section 4.1.2. Applying the continuity equation between section 1-1, 2-2 and 3-3 (shown in Fig. 4-17) results in

www.manaraa.com

$$u_{in}^{main} D^{main} = u_{out}^{main} D^{main} + v^{mh} D^{mh} \tag{4.7}$$

Here u_{in}^{main} and u_{out}^{main} are the maximum velocities at the inlet and outlet of the main domain; v^{mh} is the maximum velocity at the manhole outlet, as depicted in Fig. 4-17. Also D^{main} and D^{mh} are the height between the two walls in the main and manhole domains.

Assuming there is no energy loss, for a pressure driven flow between parallel plates, the velocity at the outlet has a parabolic profile. Once the height and the maximum velocity are known, the flow profiles at the outlets can be determined. The maximum velocity at the outlets can be calculated from a pressure gradient between the inlet and the outlet. The cross sections used for pressure gradient calculation are shown in Fig. 4-17 and labeled as 1-1, 2-2, 3-3, 4-4 and 5-5. This leads to

$$\frac{(p_4 - p_2)}{L_{42}} = \frac{8\nu}{(D^{mh})^2} v^{mh} \tag{4.8}$$

$$\frac{(p_5 - p_3)}{L_{53}} = \frac{8\nu}{(D^{main})^2} u_{out}^{main} \tag{4.9}$$

$$p_4 = p_5 \tag{4.10}$$

$$p_2 = p_3 \tag{4.11}$$

where L_{42} is distance between section 4 and 2, L_{53} is distance between section 5 and 3, and p_2, p_3, p_4, and p_5 are pressures at section 2, 3, 4 and 5, respectively.

In this simulation, a Poiseuille velocity inflow boundary is implemented at the inlet with a maximum velocity of *0.25m/s*, i.e. u_{in} = *0.25m/s*. Based on the geometry of the main pipe and the manhole, we have $D^{main} = 0.5m$, $D^{mh} = 0.1m$, $L_{42} = 2.0m$, and $L_{53} = 3.45m$. This configuration yields a theoretical maximum velocity of *0.247m/s* at the outlet of the main pipe and *0.017m/s* at the outlet of the manhole. The velocity profile at these two outlets follows a parabolic distribution which is consistent with Poiseuille flow theory. Figures 4.18 and 4.19 plot the velocity profile normal to the flow direction at the outlet of main pipe and manhole, along with the analytical solutions. It can be seen that the numerical prediction matches the analytical solution very well in both pipes.

A coarse grid of *160* x *40* is run and compared with the results from *320* x *80* grid. The velocity profile normal to the flow direction at the outlet of the main pipe and the manhole are shown in

www.manaraa.com

Figs 4.18 and 4.19 along with the theoretical solutions. It can be seen from both plots that the numerical solution converges to the analytic solution as the mesh is refined.

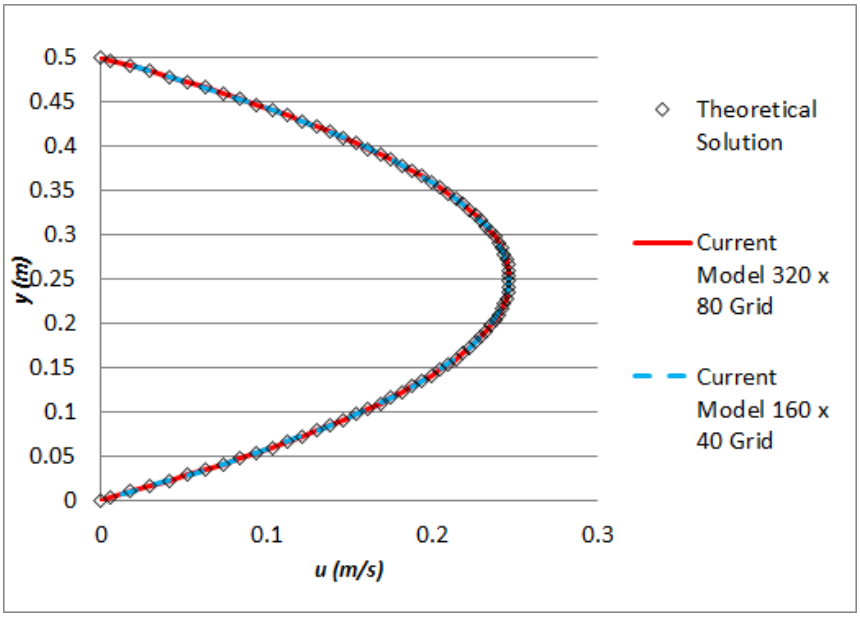

Figure 4. 18 Velocity profiles (u_{out}^{main}) at the main pipe outlet.

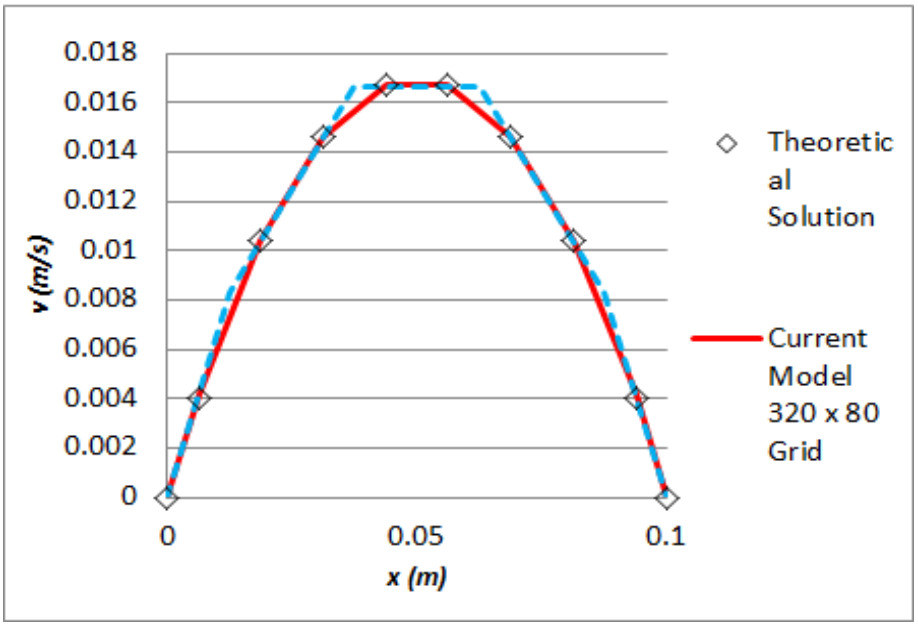

Figure 4. 19 Velocity profiles (v^{mh}) at the manhole out.

www.manaraa.com

Figures 4.20 and 4.21 show the numerical predicted pressure field in the main pipe domain and the manhole domain based on a *320* x *80* grid. It can be seen from this plot that pressure linearly drops between inlet and outlet at fully developed section, which is expected for a Poiseuille flow.

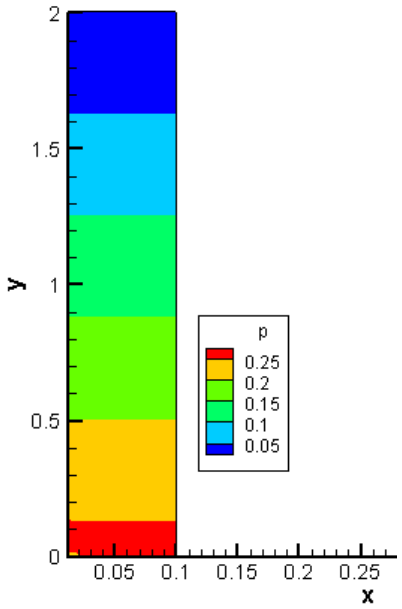

Figure 4. 20 Pressure distribution in manhole domain (320 x 80 Grid).

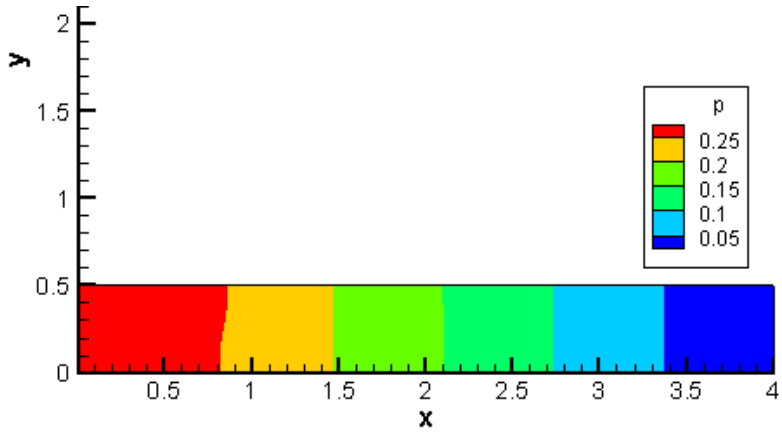

Figure 4. 21 Pressure distribution in main domain (*320* x *80* Grid).

www.manaraa.com

Chapter 5 TWO-PHASE MODEL DYNAMIC VALIDATION

VOF validations in Chapter 4 are called "static" two-phase model valuations because Navier-Stokes Equations are not solved in these simulations. In this chapter, a series of "dynamic" validations are performed. In the dynamic validations, the two-phase VOF model is coupled with a two-dimensional Navier-Stokes Solver. The coupled numerical model is tested on several two-dimensional two-phase flow benchmark problems including Rayleigh–Taylor instability, dam break, horizontal tank acceleration and uniform open channel flows.

5.1. Rayleigh–Taylor Instability

In the Rayleigh–Taylor instability problem, a heavier fluid layer initially lies on top of a lighter fluid. Densities of the two fluids are *1.225* and *0.1694kg/m*^{3}. Both fluids have a viscosity of *0.00313kg/m·s*. Instability occurs at the interface when the initial interface is disturbed. In the simulation, the interface is disturbed by a small perturbation at time $t = 0+$. The perturbation of the interface is a sinusoidal wave with amplitude of *0.05m* and a wavelength of *1.0m*, as shown in Fig. 5.1. The density difference of the two fluids deforms the interface further as time advances. The deformation continues until the two fluids completely change locations. The gravitational acceleration is *9.81m/s*^{2} in this case. The computational domain is a *4 m* x *1 m* rectangle with a mesh size of *64* x *256*. The time step size is *0.001s*. Figure 5.1 shows the initial interface shape and the evolved shape at *t=, 0.7, 0.8* and *0.9s*.

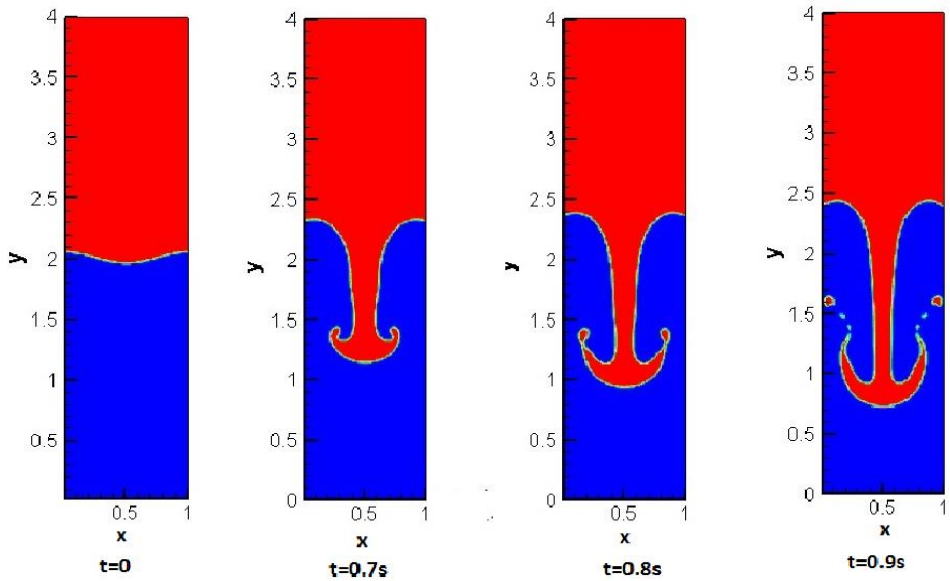

Figure 5.1 Interface at *t = 0, 0.7s, 0.8s* and *0.9s* in Rayleigh–Taylor instability problem.

www.manaraa.com

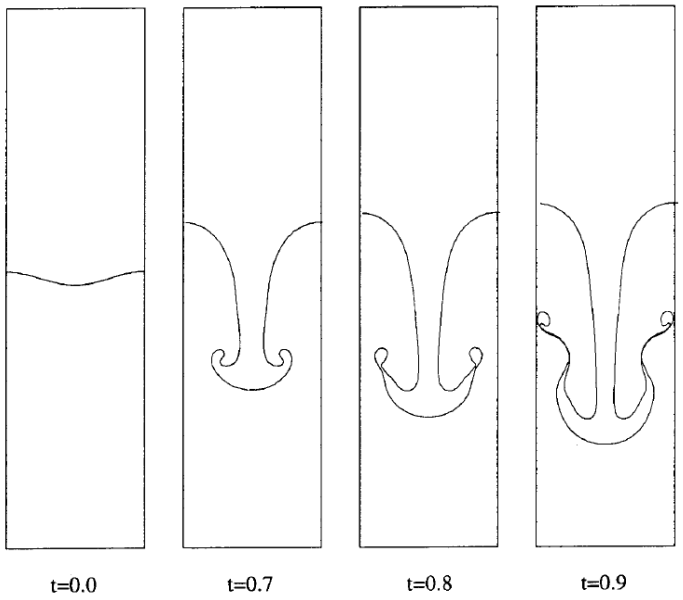

Figure 5. 2 Numerical results of Rayleigh–Taylor instability problem published by Popinet (1999 Int. J. Numer. Meth. Fluids with permission from John Wiley & Sons, Ltd.).

The interface evolution compares well with the results published by Popinet (1999) on a 128x512 grid, shown in Fig. 5.2.

5.2. Tank Horizontal Acceleration

In this simulation, a rectangular tank with two immiscible fluids is initially at rest. The top fluid is a gas; the bottom fluid is a liquid. Density is *100 kg/m*^{3} for the liquid and 1 *kg/m*^{3} for the gas. The viscosity is 0.1 *kg/m·s* and 0.001 *kg/m·s* for the liquid and gas, respectively. The tank is *1.0m* wide and *0.5m* tall. The initial liquid depth in the tank is *0.2 m*. At $t=0^+$, the tank is suddenly accelerated to the right at *1.0 m/s.*^{2} The acceleration results in a horizontal body force (B_x) of -*1m/s*^{2}; The gravitational acceleration is *9.8m/s*^{2}. The domain and initial state are shown in Fig. 5.3. The calculation is continued until the fluids reaches steady-state. The convergence criterion for the steady-state is 10^{-6}*m/s* for velocity and 10^{-6}*pa* for pressure.

www.manaraa.com

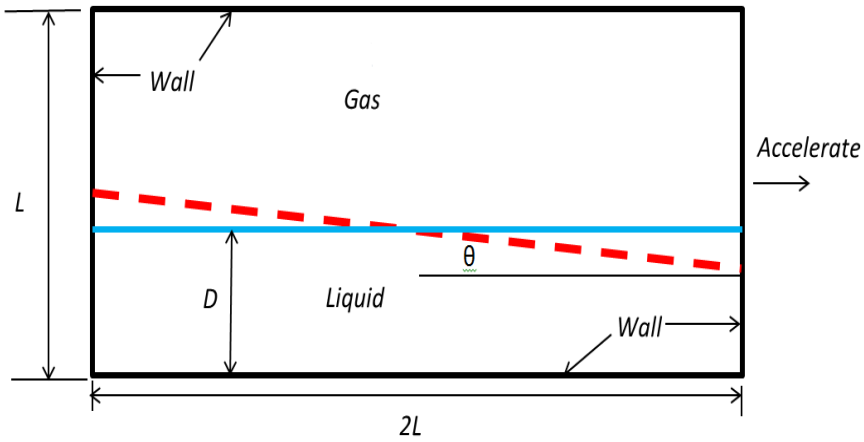

Figure 5.3 Tank horizontal acceleration computational domain

(solid line: initial flow surface; dash line: theoretical flow surface at steady state).

At steady-state, an analytical free surface configuration can be determined based on the force balance analysis in the flow field. At equilibrium the horizontal body force and the vertical gravity force are balanced by hydrostatic pressures. The equilibrium state requires the free surface incline with an angle θ to the horizontal direction. The bold dash line in Fig. 5.3 presents the analytical interface location at steady state. The inclination angle is calculated from

$$\theta = tan^{-1}\left(\frac{B_x}{B_y}\right) = tan^{-1}\left(\frac{-1}{-9.8}\right) = 0.1017 = 5.8^{o} \quad (5\text{-}1)$$

The grid size is *80* x *40* in the computation with the time step size of *0.005s*. A non-slip wall is used for all four boundaries. This boundary specification results in a pure Neumann boundary condition in the Pressure Poisson Equation, leading to an infinite number of solutions. Here a reference pressure is provided to pin the solution. In this case, the pressure reference point is chosen to be the upper corner of the tank with a reference pressure value of zero. Figure 5.4 plots both the numerical and theoretical interfaces at steady state. The numerical model accurately predicts the interface shape and location. Figure 5.5 shows the numerical pressure distribution at steady state. As expected, the pressure field within the tank is hydrostatic.

www.manaraa.com

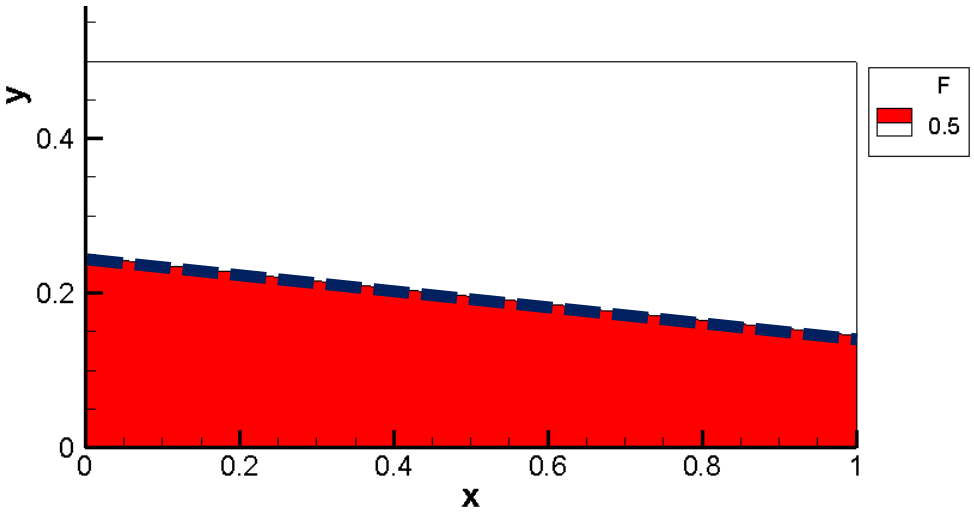

Figure 5.4 Interface at steady state

(solid line: numerical simulation; dash line: Theoretical solution).

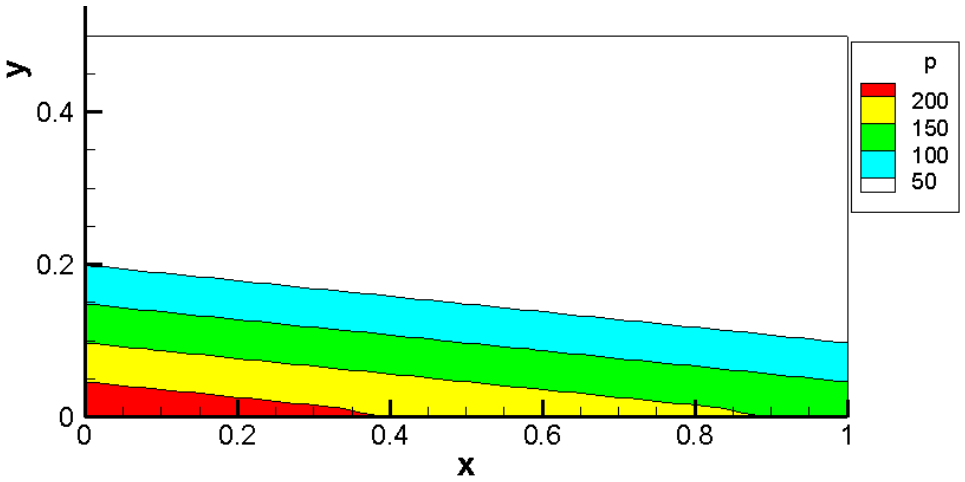

Figure 5.5 Pressure field predicted by numerical model at steady state for accelerating tank case.

5.3. Dam Break

Dam-break simulation is a benchmark problem for two-phase flow models due to the simple initial and boundary conditions. Dam break problems involve significant interface deformation such as overturning, breaking up and air entrapment. The complicated dynamics at the interface

www.manaraa.com

pose challenges to two-phase flow models. The experimental work of Martin and Joyce (1952) is commonly used to check the numerical results. In their experiments, the front propagation speed and the remaining water columns height for different dam configurations were measured.

In the dam break problem, initially a rectangular column of still water is contained between a vertical wall and a gate. At time $t = 0+$, the gate is suddenly removed and the water column starts collapsing under gravity. This collapsed water column forms an advancing wave that propagates to the right. Two different initial water column sizes are simulated in this work. In Case I, the initial water column is a rectangle with height and length of $2a$ x $1a$. In Case II, the initial water column is a square with height and length of $1a$ x $1a$. Here a is the dimension unit used in Martin and Moyce's experiments and a equals to $0.05715m$ in all simulations. The computational domain and initial water column are shown in Fig. 5.6.

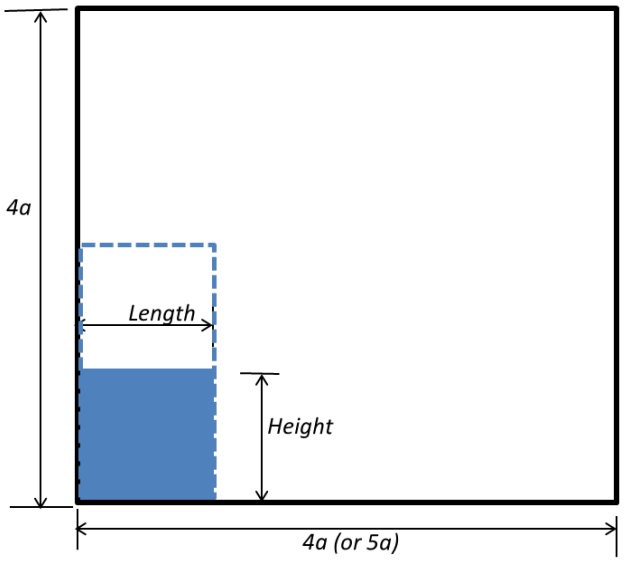

Figure 5.6 Dam break simulation initial condition ($a = 0.05175\ m$).

In Martin and Moyce's (1952) experimental setup, the downstream of the contained water column is a channel that is slightly wider than the water column. But in this simulation, the downstream channel is cut off and a rigid wall is used at some distance from the dam. For both cases, the height of the computational domain is $4a$. The length of the computational domain is $4a$ for case I

www.manaraa.com

and *5a* for case II. The domain size for Case I was chosen so that it is close to the experimental system used in the experiments by Koshizuka et al. (1995), in which the dam break phenomenon was videotaped.

A non-slip boundary condition is used for the two vertical walls and the bottom wall. The top boundary is open. The two fluids are water and air. The densities of water and air are $1000kg/m^3$ and $1.23kg/m^3$, respectively. Viscosities for water and air are $1.0x10^{-3}kg/m{\cdot}s$ and $1.8\times10^{-5}kg/m{\cdot}s$, respectively. The gravitational acceleration is $9.8m/s^2$. The grid size is *64* by *64* with a time step size of $5x10^{-5}s$. Three sets of grid size are used in this simulation including *32* x *32*, *64* x *64* and *128* x *128*. Time step size is $1.0x10^{-4}$ *s*, $5.0x10^{-5}$ *s and* $2.5x10^{-5}$ *s* for grid size of *32* x *32*, *64* x *64* and *128* x *128* grid respectively. Zalesak FCT is used in the discretization of the advective term. Shuman filter value $\beta = 5000$ is used to filter velocity component *u* and *v* for all grid size.

To compare with the experimental results, the wave front location (*x*), remaining water column height (*h*) and time (*t*) are converted to the non-dimensional numbers published in Martin and Moyce's work. The normalization factors used to produce the dimensionless numbers in Cases I and Cases II are shown in Table 5.1. Here *x* is the front location; *h* is the remaining water column height after dam collapse and *t* is time.

Table 5.1 Definition of dimensionless parameters used in plots.

	Case I (*2a* x *1a*)	Case II (*1a* x *1a*)
Wave Front Location x^* vs. dimensionless time T^*	$x^* = \frac{x}{a}, T^* = t\sqrt{(\frac{2g}{a})}$	$x^* = \frac{x}{a}, T^* = t\sqrt{(\frac{g}{a})}$
Remaining Water Column Height h^* vs. dimensionless time t^*	$h^* = \frac{h}{a}, t^* = t\sqrt{(\frac{g}{a})}$	$h^* = \frac{h}{a}, t^* = t\sqrt{(\frac{g}{a})}$

www.manaraa.com

Figure 5.7 shows the surge front locations and compares the numerical predictions and experimental results for Case I. Figure 5.8 shows the water column height and compares the numerical predictions with the experimental measurements. It can be observed that the numerical prediction of water heights, wave front location and advancing wave agree very well with the experimental data. However, it can be seen that the numerical solution does not converge to the experimental solution as the grid is refined.

Several reasons could possibly contribute to the discrepancy between the experimental and numerical results. First there is no turbulent model in the numerical model. A dam-break phenomenon involves violent flow conditions with significant shearing and energy losses. Without a turbulent model, the energy loss could not be reflected accurately. Hence the numerical front could move more freely. Another reason could be contributed to the difficulty in determining the exact location of the leading edge in the experiment, as mentioned by other researchers (Greaves 2004).

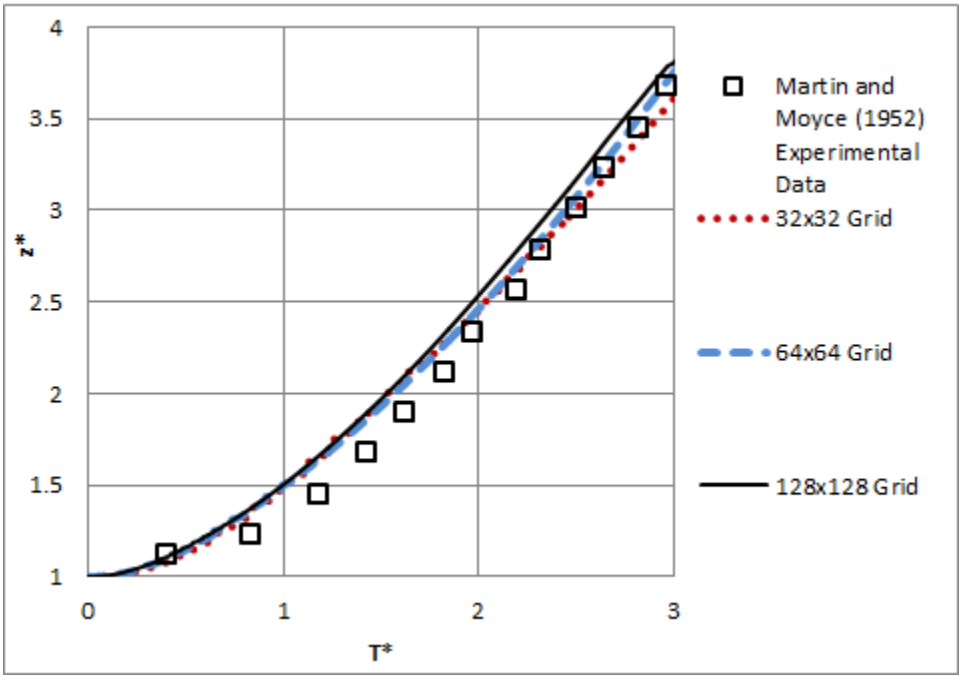

Figure 5.7 Surge front location (initial water column height x width = *2a* x *1a*).

www.manaraa.com

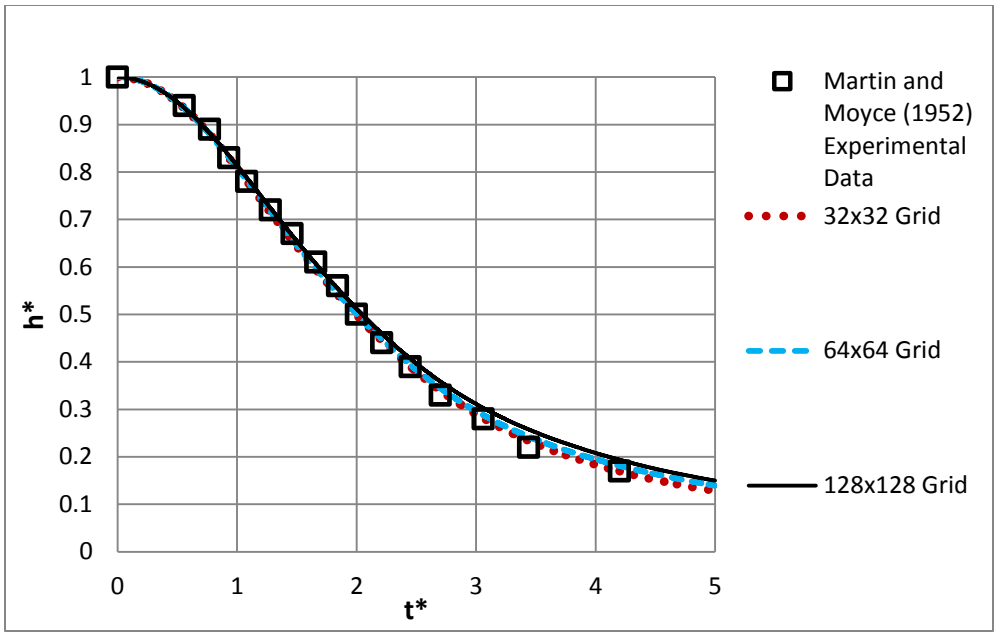

Figure 5.8 Remaining water column height (initial water column height x width = *2a* x *1a*).

To investigate this discrepancy in the grid convergence test, additional simulations are performed which is Case II (*1a* x *1a*). Martin and Moyce (1952) developed a theoretical solution for this case by solving a velocity potential equation as suggested in Penney (1952). However, the analytical solution was only valid for a very short time after the dam collapse. The theoretical analysis ignored energy loss and turbulence. The theoretical solutions are plotted in Fig. 5.9 along with the experimental data and numerical simulations for the three grid sizes. As shown in this plot, the numerical solution converges to the theoretical solution. This is consistent with expectations as the current model does not include turbulence simulations and associated energy losses.

www.manaraa.com

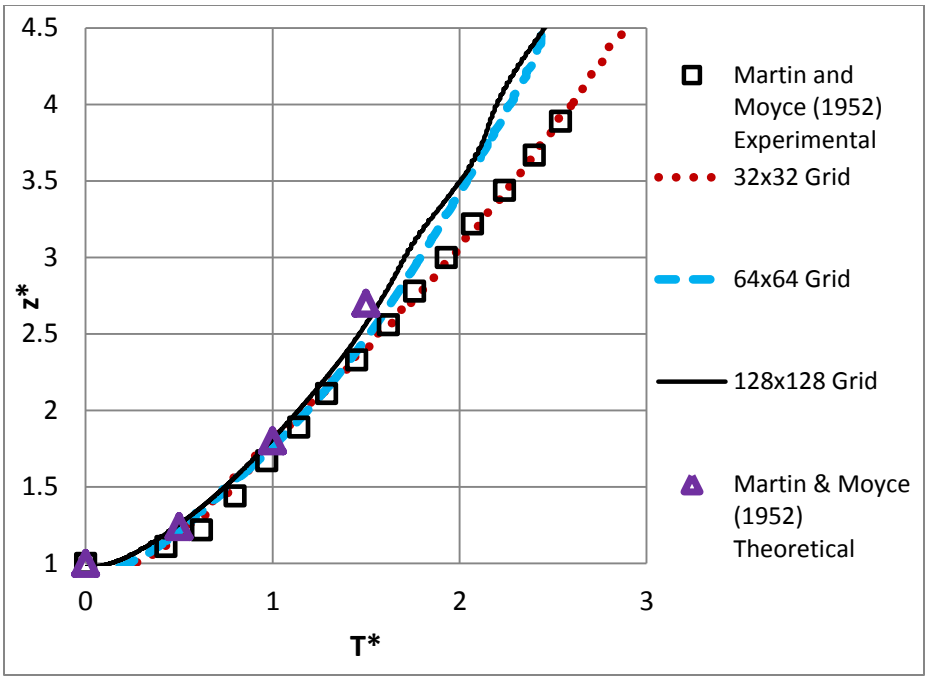

Figure 5.9 Surge front location (initial water column height x width = *1a* x *1a*).

The converging pattern issue indicated in Figs. 5.7 through 5.10 has been noticed by several researchers in their numerical simulations. Greaves (2004) reported the same pattern as grid size shrinks when he implemented a VOF method to simulate two fluid flows. He performed numerical simulations for the same two initial water columns sizes used in this work using grid size *32* x *32*, *64* x *64* and *128* x *128*. This pattern was also observed by Ubbink (1997) when he studied two-phase flow problems with sharp interfaces. He showed that the leading edge predicted by numerical models moves faster as the grid resolution increase. Also Hieu (2004) plot the dam break numerical simulation data published by Hirt and Nichols (1981) in his original VOF paper for an initial water column size of *2a* x *1a*. The plots indicates that the computed front with a $\delta y=0.05$ grid size is further away from the experimental measurement as compared to using a finer ($\delta y = 0.025$) grid size.

Figure 5.10 shows the remaining water column height with time compared with the corresponding experimental measurements. Similar to Case I, the remaining water column height is predicted very well by the numerical model.

www.manaraa.com

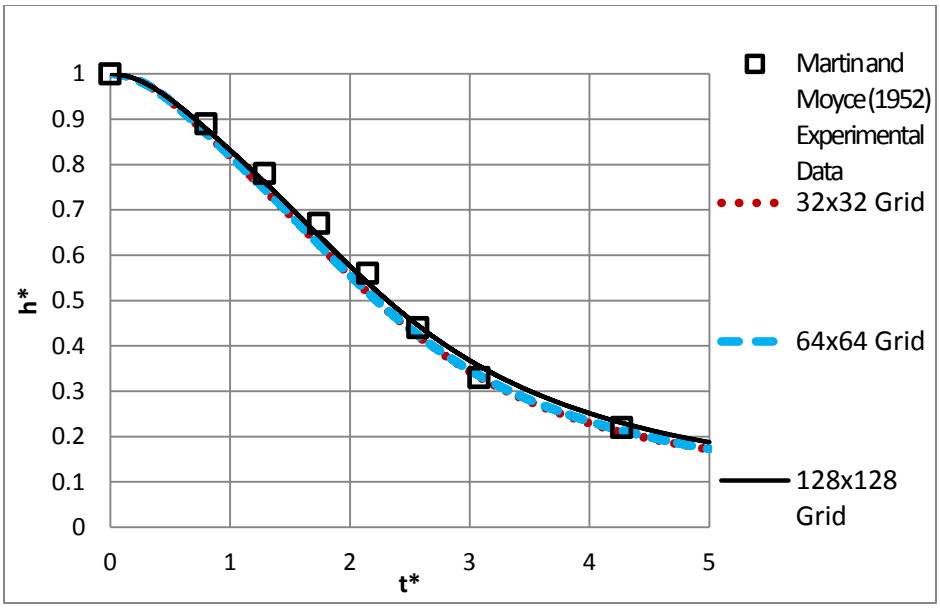

Figure 5.10 Remaining water column height (initial water column height x width = *1a* x *1a*).

Snapshots of the interface from the numerical model for Case I at selected times are displayed in Figs. 5.11a and 5.11b. The dimensionless time used in these plots is defined as $T^* = t\sqrt{g/a}$. Figures 5.11a and 5.11b show at time (a) $T^* = 0$; (b) $T^* = 1.71$; (c) $T^* = 3.99$; (d) $T^* = 4.91$; (e) $T^* = 6.45$; and (f) $T^* = 8.15$. It can be observed that the numerical model predicts the motion of the dam break wave front as well as the dynamics between water and air. The interface evolution also compares well with the dam break flow motion videotaped by Koshizuka (1995) in his experiments. From the numerical snapshots, it appears that the water column collapsed and formed a wave front immediately following the removal of the gate. After the wave front hit the right wall, it starts climbing the right wall. At $T^* = 4.91$, the water column started detaching from the wall and overturning. A water jet was formed and impinged into the water accompanied with air entrainment. This case demonstrated that the numerical model is capable of simulating complex free surface flow with air entrainment, break-up and merging, and interface overturning.

www.manaraa.com

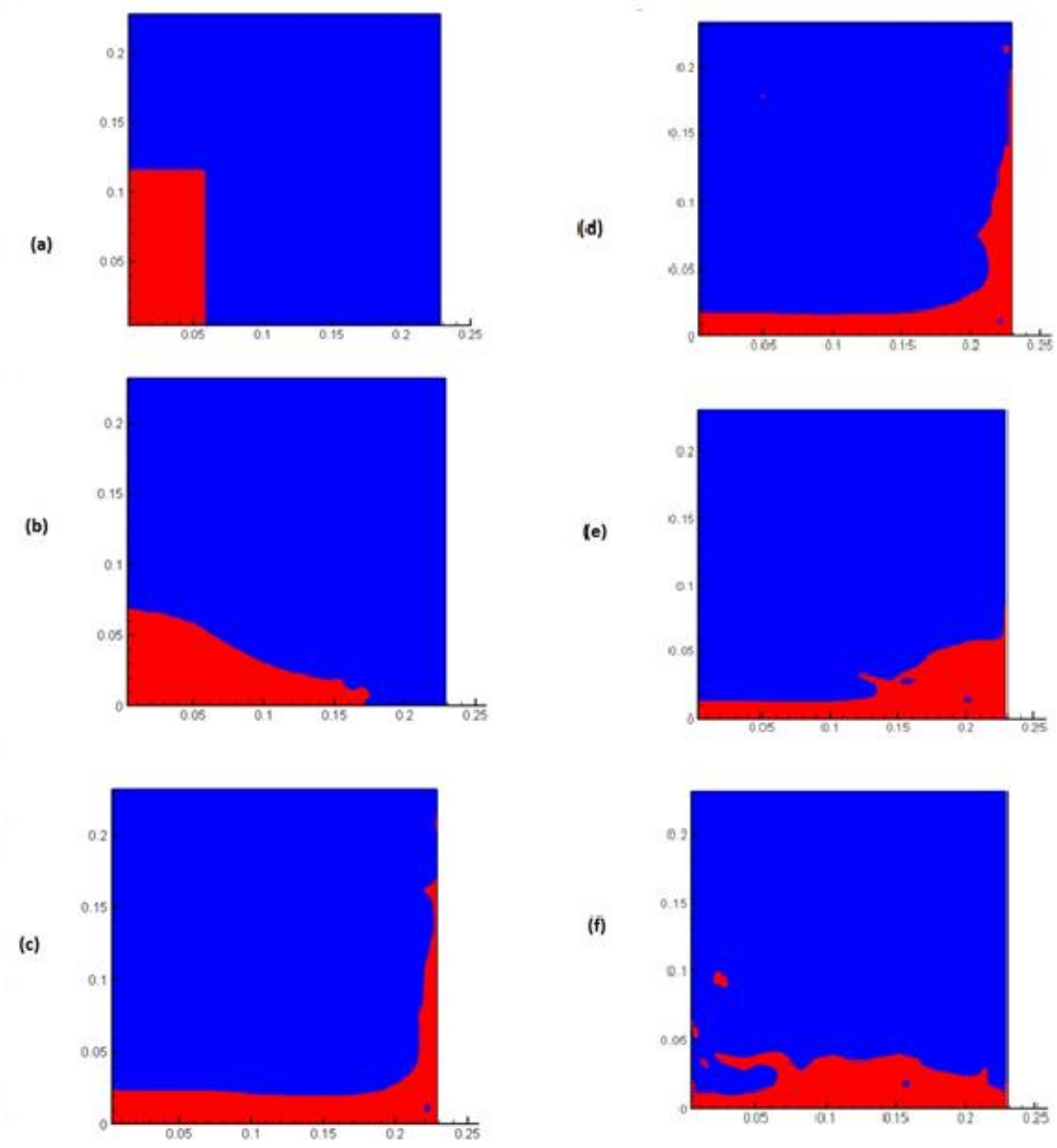

Figure 5.11 Dam break snapshots for initial water column height x width = *2a* x *1a*.

5.4. Uniform Open Channel Film flow

The next validation simulation is a two-dimensional open channel film flow with a known analytical solution. This test is to validate the implementation of inflow and outflow boundary condition in a two-phase simulation. This simulation is similar to a gravity flow in the stormwater system.

www.manaraa.com

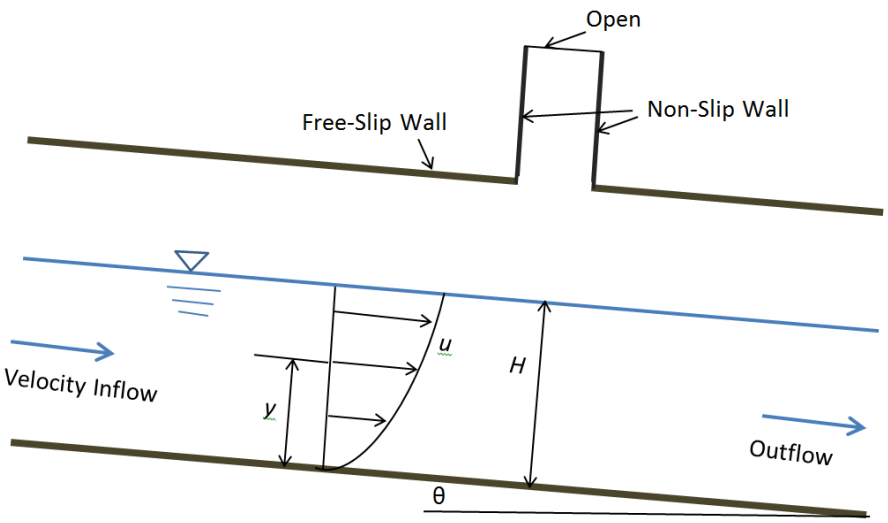

Figure 5.12 Uniform open channel flow.

In this problem, a constant thickness film of viscous liquid flows down a plan that is inclined at angle θ, as shown in Fig. 5.12. The flow, driven by gravity, is a uniform flow in a laminar motion. In the uniform channel flow, gravity acceleration is balanced by frictions from channel bottom. Flow within the channel remains the same profile along the flow direction.

The analytical solution of this type of flow could be derived from two-dimensional Navier-Stokes Equations by assuming a fully developed flow along the flow direction (all variable gradients are zero). Additionally, since the presence of a free surface indicates a zero flux across the interface. The shear stress at the top of the flow is set to zero. The resulted analytical velocity profile is half of a Poiseuille flow. The analytical velocity profile can be written as

$$u(y) = \frac{gsin(\theta)}{2\nu} y(2H - y); v = 0 \tag{5.2}$$

where H is the total flow depth in channel and y is the flow depth. Likewise, if a flowrate is determined, the normal depth could be calculated from Eq. 5.2.

The computation domain includes a main pipe and a manhole. The domain in the horizontal direction enclosed by two walls is denoted as “main domain” or “main pipe”. A rectangular domain in the vertical direction is added to the top of the main domain and is referred to as “manhole domain”, as shown in Fig. 5.12. The use of a manhole domain is to allow air move in

www.manaraa.com

and out of the system freely, thus avoiding artificial pressure buildup. The main pipe is *8m* long and *0.4m* tall. The manhole domain is *0.2m* wide and *0.1m* tall. The manhole center is located at *x=5.05m*. Three sets of grid size are used in the simulation to observe the grid convergence trend, namely, *80* x *20*, *160* x *40* and *320* x *80*. Time step used for the three grids is

The two fluids in this simulation are hypothetical fluids. The heavier fluid has a viscosity value of *0.05 kg/m·s* and a density value of *1000.0 kg/m*^{3}. The lighter fluid has a viscosity of *0.001 kg/m·s* and a density of *1.0 kg/m*^{3}. Body force along flow direction is $B_x = g*sin(\theta)$ while normal to the flow direction is $B_y = - g*cos(\theta)$ with g being gravity acceleration. Initially, the flow field is uniform with an analytical profile. The initial flowrate for the heavier fluid is *0.01m*^{3}*/s* and the initial flow depth is *0.05m*.

The non-slip wall boundary is used for channel bottom boundary. A free-slip wall boundary is used for the top of the channel to simulate an atmosphere open field. A specified velocity profile inflow boundary is used for the inlet. The inflow velocity profile is a uniform velocity obtained by dividing the flowrate by depth. The flowrate are *0.01 m*^{3}*/s* for the heavier fluid and *0.007 m*^{3}*/s* for the lighter fluid. At the outlet, an outflow boundary condition is implemented. Since gravity is included in the simulation, pressure at the outlet has a hydrostatic distribution.

It can be verified that Froude number for this problem is

$$Fr = \frac{v}{\sqrt{gh}} = \frac{0.25\ m/s}{\sqrt{9.8\ m/s^{-2} * 0.05m}} = 0.7 \tag{5.3}$$

The Froude number is less than one, hence the flow is subcritical and a downstream depth needs to be provided for calculations. The downstream boundary depth is the normal depth corresponding to the channel slope and flowrate. If a random depth is specified at the outlet, it would impact the upstream flow pattern. In such a case, a free surface profile would form and force the upstream normal depth to tie in with the depth specified at the downstream end. In engineering practice, this often occurs if a channel flows into a reservoir. It is referred as "backwater effect" when the reservoir surface is higher than the normal depth at the channel downstream. In this simulation, the downstream depth is specified to be the same depth used in the initial condition, which is *0.05 m*.

The time step size is set to be δt*= 0.001s*. The simulation is run until steady-state, with the convergence criteria set to be *10*$^{-6}$ and *10*$^{-3}$ for the velocity and pressure, respectively.

www.manaraa.com

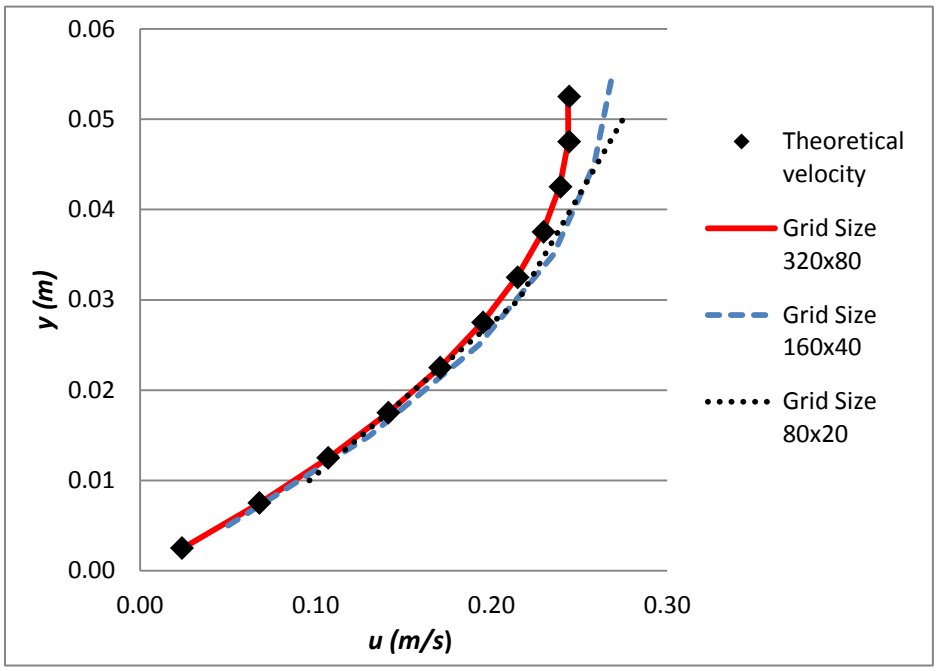

Figure 5.13 Velocity profile at the downstream side of the channel.

Figure 5.13 plots the velocity profile predicted by the model using three grid sizes at the outlet, and compares them with the analytical profile. It can be observed that the numerical solution matches the analytical result very well. It could also be seen that as the grid size is refined, the numerical solution converges to the analytical solution.

Figure 5.14 plots the pressure distribution and free surface in the channel at steady state. The surface is parallel to the channel bottom with the pressure distribution being hydrostatic, as expected in a channel that flows under normal/uniform conditions.

www.manaraa.com

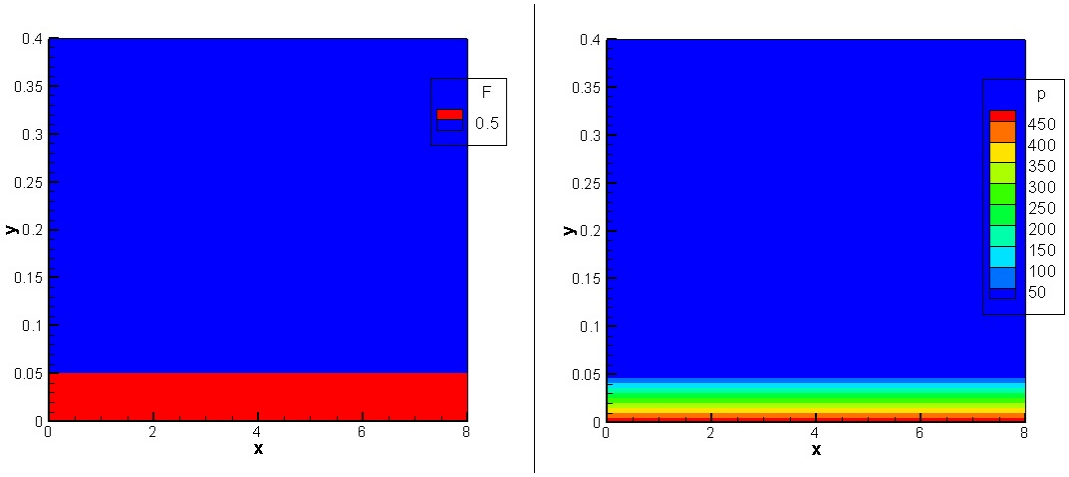

Figure 5.14 Pressure distribution and free surface.

www.manaraa.com

CHAPTER 6 TRANSIENT FLOW SIMULATION

In the previous chapters, the two-dimensional two-phase numerical model has been extensively tested and validated. As described in chapter 2, the process of geyser formation involves mixed flow where a surge wave propagates in the pipe and traps air within the system. In this section, the numerical model will be applied to practical open channel problems with wave features, more specifically, open channel bore and pressurization waves.

Waves occur frequently in free surface flows. A wave is manifest by variations in flow depth. A wave could propagate in still water as well as in moving flows. Depending on the direction of the wave propagation relative to the flow, a wave could be categorized into "positive" and "negative". A wave is referred to as "positive" if the flow depth behind the wave is higher than the undisturbed flow depth and is called "negative" in the opposite case (Chaudhry, 1993). A wave with a steep front usually symbolizes a discontinuity in the velocity and depth at the wave front.

Surge wave are considered positive waves. It usually originates from an increase inflow or a reduced downstream flow area, and shows as an increase in flow depth. A surge wave impacts the flows in several ways. On one hand, a surge with sufficient strength or height can induce pressurization in the system by completely filling the flow area with water, which, in turn, blocks the air passage. Also, a surge wave may introduce instabilities in the air-water interface, generating waves on the surface that block the air passage. Additionally, as the surge wave propagates, it compresses existing air pockets in the system.

In this section, the numerical model simulates two types of positive surge waves that occur frequently in the stormwater system, namely open channel bore and pressurization surge wave. In both simulations, the surge waves are generated by a sudden closure of a downstream gate in a frictionless horizontal channel. A distinguish difference exists between these two types of surge waves. The former has a height lower than the pipe crown and hence the whole flow region still flows under gravity with an air passage on top of the free surface. The latter has a pressure head that exceeds the pipe crown and the flow region behind the wave becomes pressurized. This type of wave causes increased pressurization in the pipe as it propagates. The pressure wave is typically characterized by a faster wave speed than an open channel bore. When a downstream gate is suddenly closed, a positive surge forms immediately at the downstream and reflects back towards the upstream. If the initial pipe flow almost flows full prior to the closure, the closure

www.manaraa.com

induces a pressure wave and starts pressurizing the whole pipe. Otherwise, an open channel bore would form and propagate towards upstream.

6.1. Horizontal Channel Open Channel Bore

In a horizontal channel, there is no gravity acceleration in the *x*- direction. The open channel is represented by a rectangular computational domain that contains two parallel walls. Figure 6.1 shows a sketch of the computational domain. The computation domain includes a main pipe and a manhole. In the surge wave simulations, the manhole domain purely acts as a venting outlet so that air could travel freely in and out of the system. The purpose of using a manhole domain in this simulation is to avoid artificial pressure buildup within the system.

In this test case, the main computational domain is *12m* long (*L*) and *0.15m* deep (*D*). A manhole vent is located at $x = 1.5\ m$ to allow the air to escape from the system. The manhole is *0.15 m* wide and *0.15 m* tall. The grid size used in the surge simulation for the main domain is *320* by *40*, whereas the grid size for the manhole is *8* by *40*. The densities of water and air in the simulation are $1000kg/m^3$ and $1.23kg/m^3$, respectively. Viscosities of water and air are $1.0x10^{-3}kg/m{\cdot}s$ and $1.8\times10^{-5}kg/m{\cdot}s$, respectively. Gravity is $9.8m/s^2$.

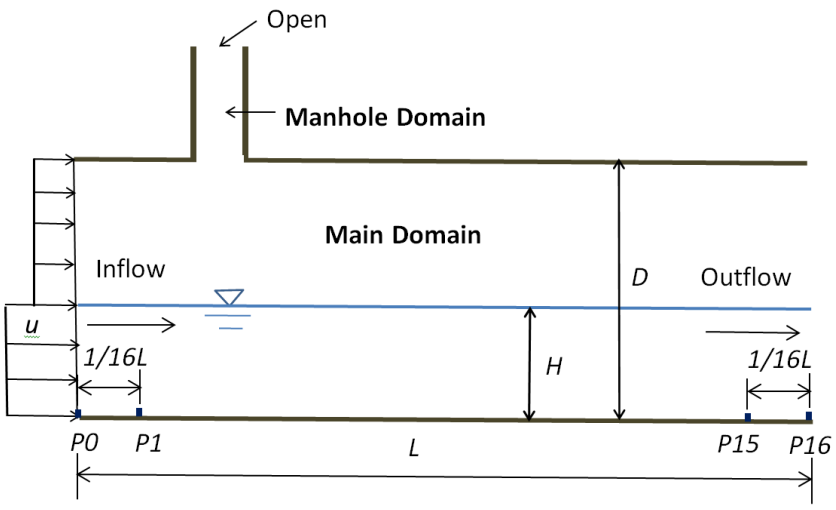

Figure 6. 1 Schematic of a horizontal channel.

www.manaraa.com

To record the pressure history during the surge wave propagation, pressure head is output for seventeen (*17*) locations at the channel bottom, referred as pressure recording points. These pressure recording points, denoted by *P0* through *P16*, are spaced evenly along the channel bottom with *P0* at the upstream end and *P16* at the downstream end. The layout of the pressure recording points is shown in Figure 6.1.

6.1.1. Open Channel Bore Analytic Solution

An open channel bore is a positive surge wave characterized by a surge height lower than the pipe crown. This type of surge wave has an analytical solution for a frictionless horizontal channel. The unknown surge height and wave speed can be calculated analytically from surge theories. The control volume of a positive surge wave front is shown in Fig. 6.2. Originally, a fluid is flowing steadily from left to right with a uniform velocity V_1 in a frictionless channel. Suddenly the downstream gate is shut down and generates a positive surge wave that reflects back with a speed *c*. By using a Lagrangian coordinate frame of reference that moves in the same speed as the surge front, mass and momentum conservation laws can be written for the two faces of the control volume, labeled as 1-1 and 2-2 in Fig. 6.2, namely,

$$(V_1 + c)A_{1=}(V_2 + c)A_2 \tag{6.1}$$

$$\gamma(\ \bar{y}_1 A_1 - \bar{y}_2 A_2) = \rho A_1 (V_1 + c)(V_2 + c - V_1 - c) \tag{6.2}$$

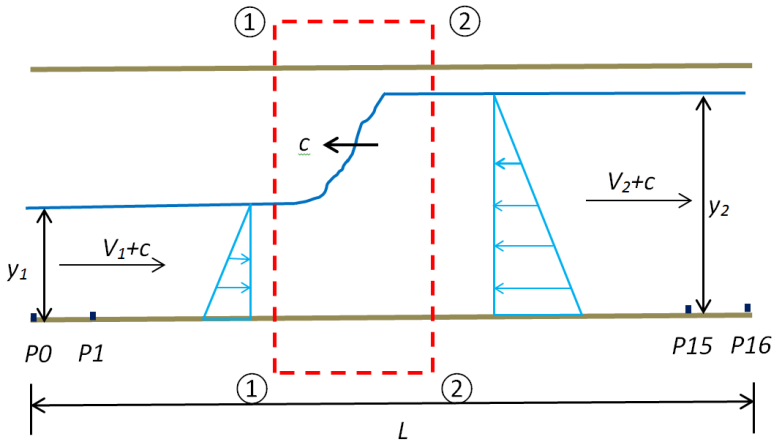

Figure 6. 2 Control volume analysis of a positive open channel surge wave.

www.manaraa.com

where V_1 and V_2 are flow velocities on both sides of the surge, A_1 and A_2 are flow areas, c is surge wave speed, $\bar{y}_1$ and $\bar{y}_2$ are centers of gravity for each flow area, and y_1 and y_2 are flow depths at the cross sections. By assuming hydrostatic distribution on both sides of the surge, we have $\bar{y}_1 = \frac{1}{2}y_1$ and $\bar{y}_2 = \frac{1}{2}y_2$. For a unit-width rectangular channel, $y_1 = A_1$ and $y_2 = A_2$. Substituting these values into Eqs. 6-1 and 6-2, combined with the boundary condition $V_2 = 0$, leads to only two unknowns, the surge speed c and the surge height y_2.

6.1.2. Open Channel Bore Initial Steady State Condition

A wave is an unsteady flow. To simulate an unsteady flow, a steady state flow field needs to be established first and used as an initial condition. Most of the time, it is difficult to define an steady state flow field that satisfies the continuity equation, especially in the two-phase flow cases. Hence the simulation of the unsteady flow actually contains two steps. The first step is to generate a steady state flow field. The second step is the actual surge simulation following the establishment of an initial steady state flow condition.

The generation of a steady state flow field is performed as follows. The flow is initially at rest. Then at $t = 0^+$, an inflow profile is introduced to the system at the inlet. The downstream boundary type is outflow. . The system is run until a steady-state is reached.

The time step is *0.001 s* for a *320* by *40* grid. The steady-state convergence criteria are $10^{-6} m/s$ for the velocity and $10^{-4} pa$ for the pressure, respectively.

The upstream boundary is velocity inflow. Since gravity is included in the simulation, pressure at the outlet is hydrostatic. The Froude number for this problem remains less than one. Hence the flow in this simulation is subcritical, which means a flow depth is needed at the downstream boundary. For a subcritical inflow, either a flow depth or a velocity profile can be specified at the upstream inlet boundary but not both. For this study, the velocity profile is specified while the depth at the inlet can vary. This inflow boundary condition is implemented as follows. A constant flowrate is prescribed at the inlet for both water and air. A uniform velocity profile is calculated from the pre-defined flowrate once the depth is known from the solution procedure. The bottom and top walls for the main domain are free-slip. All the walls in the manhole domain are non-slip. The top boundary of the manhole domain is an open boundary.

www.manaraa.com

At steady-state, the flow depth is *0.1088m*. The inflow flowrate is $0.03m^3/s$ for the water phase and is $0.007m^3/s$ for the air phase. At steady-state, the velocity profile at the outlet of the main pipe is plotted in Fig. 6.3, which shows a mean velocity of *0.2759m/s* for the water phase.

The pressure distribution at steady-state is plotted in Fig. 6.4. The pressure distribution is hydrostatic, as expected for a uniform open channel flow. At steady-state, the free surface is a plane parallel to the channel bottom, as shown in Fig. 6.5. This is consistent with the open channel flow theory for a frictionless horizontal channel (Chaudhry 1993).

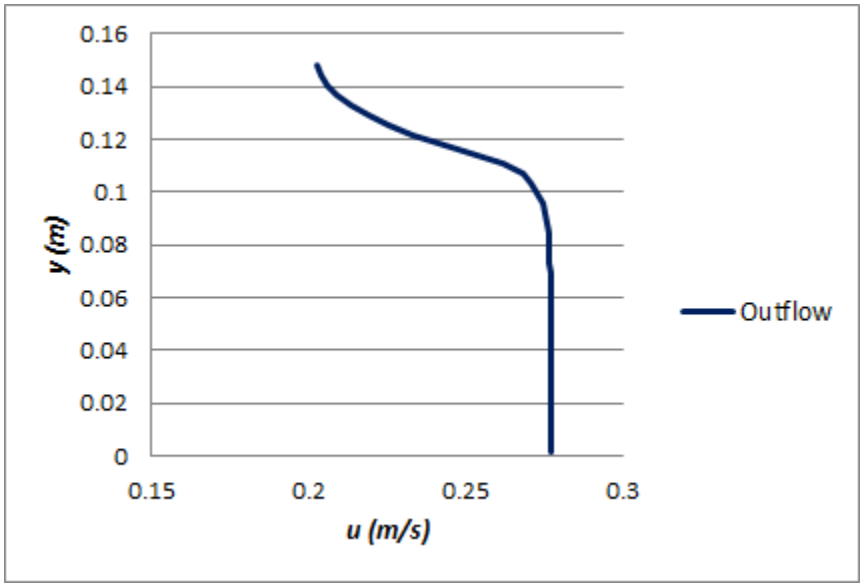

Figure 6. 3 Steady-State velocity profile at the outlet of main pipe in open channel bore simulation.

www.manaraa.com

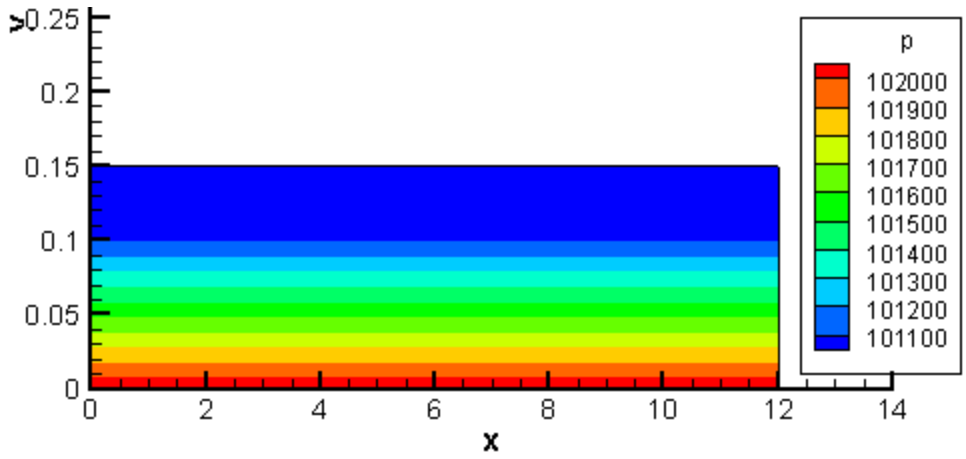

Figure 6. 4 Initial pressure field in open channel bore simulation.

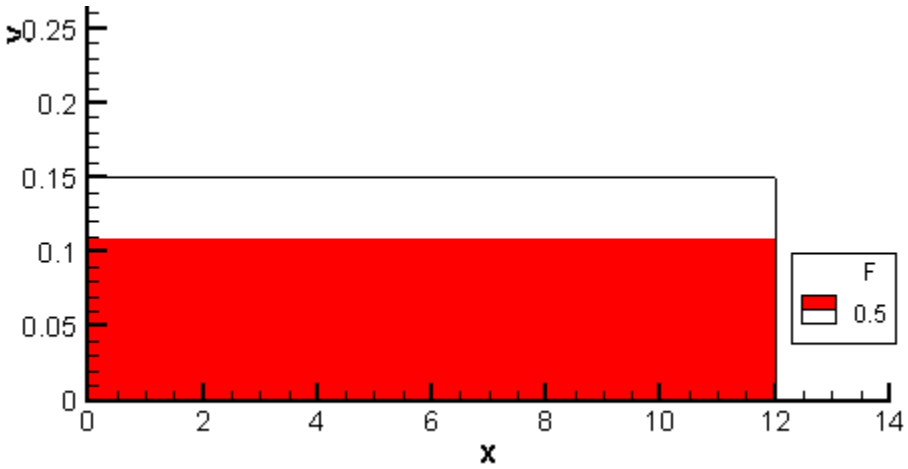

Figure 6. 5 Initial interface in open channel bore simulation.

6.1.3. Open Channel Bore Simulation

Once the initial steady state is reached, the downstream gate is shut down by switching the downstream boundary to a non-slip wall at $t = 0^+$. In this case, the initial velocity and flow depth in this simulation are relatively low. The sudden closure induces an open channel bore with the hydraulic head lower than the upper wall.

www.manaraa.com

The grid size used in the surge simulation is the same as in the initial steady state simulation for both main and manhole domains. The time step is *0.001s* for a *320* x *40* grid.

Figure 6.6 compares the pressures head predicted by the numerical model and the theoretical values at pressure recording points P6, P9 and P13, located *3/8L*, *9/16L* and *13/16L* downstream from the inlet, respectively. It can be seen from the plot that the numerical prediction of the front location, as well as the surge wave depth, matches the theoretical solution very well.

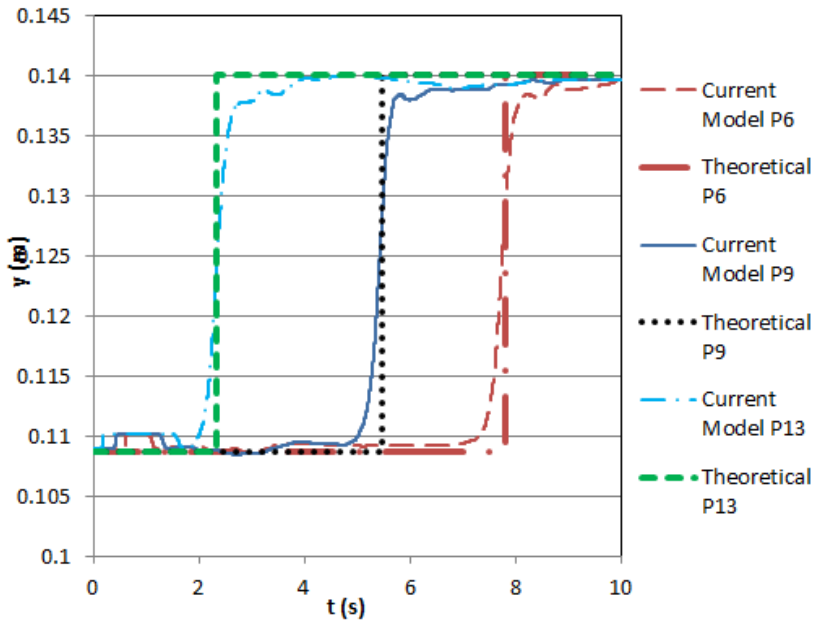

Figure 6. 6 Comparison of numerical and theoretical solutions of surge front in open channel surge simulation.

Figure 6.6 also shows that the calculated profiles contain slight numerical oscillations. The oscillations make it difficult to read a mean value directly from the plot. To further compare the numerical and theoretical results quantitatively, the calculated profile after $t = 8$ s was filtered temporarily (averaged over time) to obtain the mean value of the surge height. The filtered values from the model and the theoretical results are summarized in Table 6.1. The surge speeds calculated at pressure points *6*, *9* and *13* are also showed in Table 6.1 compared with the

www.manaraa.com

theoretical values. As seen from this table, the numerical results satisfactorily predict the surge speed and surge head for the open channel bore propagation case.

Figure 6.7 plots the instantaneous interfaces at time *t = 1s, 3s, 5s* and *7s*. A steep surge front can be observed from the plot, as expected for the horizontal channel bore. The bore maintains a similar shape and depth as it propagates towards upstream.

Table 6.1 Comparison between the numerical prediction and theoretical solution of wave speed and height for an open channel (grid size 320 x *40*).

	Current Model			**Theoretical**
	P6	**P9**	**P13**	-
Location (m)	4.5	6.75	9.75	-
Front Reaching Time (s)	7.72	5.4	2.3	-
Surge Speed (m/s)	-0.972	-0.972	-0.978	-0.960
Surge Height (m)	0.1391	0.1397	0.1397	0.1400

www.manaraa.com

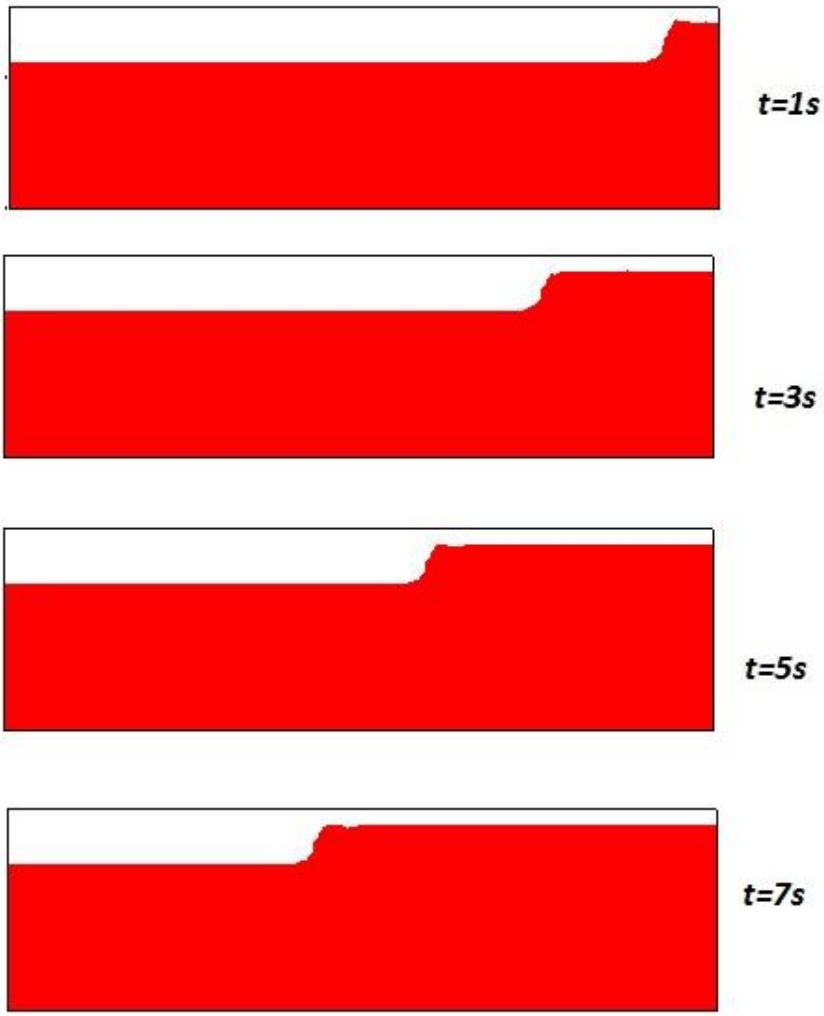

Figure 6. 7 Instantaneous interface at time *t = 1s, 3s, 5s* and *7s* in open channel bore simulation.

6.1.4. Open Channel Bore Grid Convergence Test (GCT)

To measure the convergence performance of the model, an additional simulation with a coarser grid (*160* x *40*) for the same channel flow is compared to the results of the finer grid. In Figs. 6.8 and 6.9, the surge head predicted by two different grid sizes are plotted along with the theoretical solution. As the grids are refined, the numerical prediction is closer to the theoretical solution. This indicates that the numerical simulation is converging.

www.manaraa.com

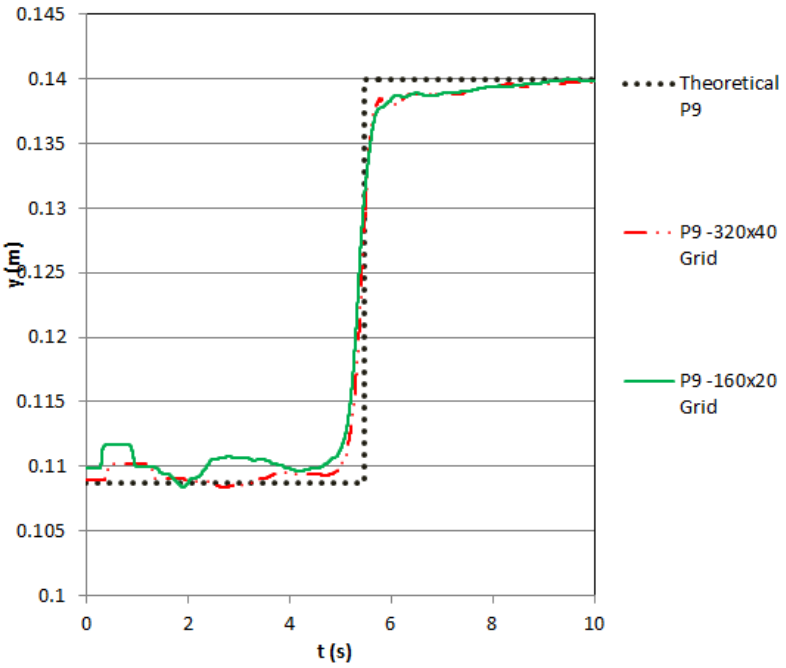

Figure 6. 8 Grid convergence test for open channel bore simulation at pressure recording point *P9*.

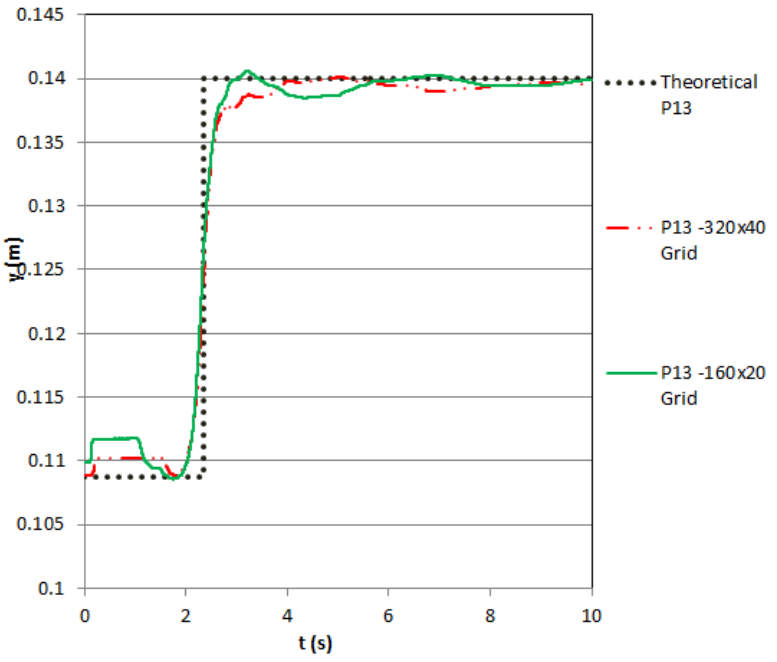

Figure 6. 9 Grid convergence test for open channel bore simulation at pressure recording point *P13*.

www.manaraa.com

6.2. Pressurization wave simulation

The last section simulated a downstream gate closure that resulted in a hydraulic bore, where the surge is not great enough to reach the pipe crown. Now a downstream gate closure will produce a wave that will reach the top wall, creating a pressurization wave. The numerical results are compared with analytical solutions at various points along the channel.

The computational domain in the pressurization wave simulation is the same as the open channel bore simulation in Section 6.1. The main domain is *12 m* long and *0.15 m* deep. The manhole domain size is *0.15m* wide and *0.3m* deep. The manhole domain starts at $x = 1.5m$ in the main pipe. The grid size used in the surge simulation for the main domain is *320* by *40*, whereas the grid size for the manhole is *4* by 8*0*. The time step is *0.001s*. The inflow flowrate is $0.04m^3/s$ for the water phase and is $0.00544m^3/s$ for the air phase.

In this simulation, the manhole also only acts as a venting outlet to allow the air to freely flow out of the system. A total of seventeen (17) pressure recording points are placed the same way as in Section 6.1. The two fluids simulated are still water and air with same density and viscosity values as in Section 6.1.

6.2.1. Pressurization Wave Analytic Solution

A pressurization wave occurs if the initial channel flows almost full before a sudden increase of inflow or downstream gate closure. The speed and height of a pressure surge wave in a frictionless horizontal channel can be calculated in a similar fashion as for an open channel surge wave in section 6.1, except that the surge height is above the pipe crown (top wall). Figure 6.10 shows the control volume for a positive pressure surge wave that is reflecting to the left with a speed *c*.

www.manaraa.com

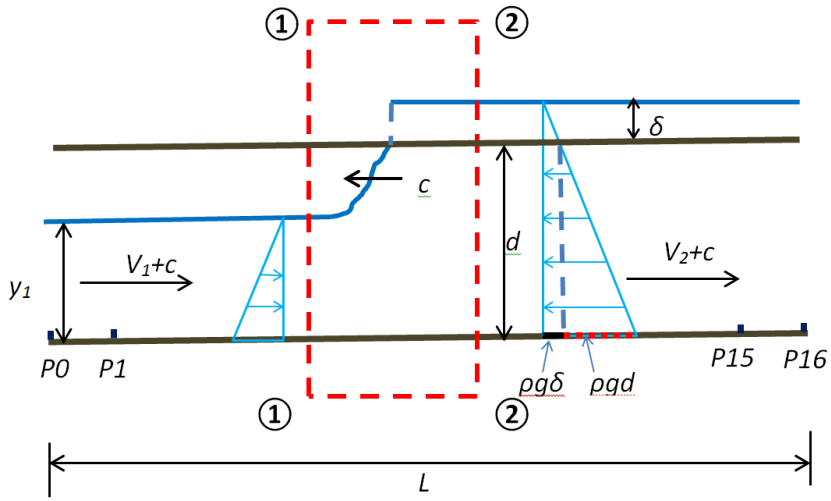

Figure 6. 10 Control volume analysis of a positive pressure surge wave.

The same set of continuity and momentum equations (Eqs. 6-1 and 6-2) are written for a pressure surge wave, with one modification. In the pressure wave momentum equation, the calculation of $\bar{y}_2$ is more complicated. Because the flow behind the surge wave is pressurized, the pressure distribution for flow area 2-2 has a trapezoidal shape, as shown in Fig. 6.10. To calculate the total pressure for flow area 2-2, the trapezoidal shape is split into two parts: a rectangle and a triangle. The width of the rectangle is $\rho g \delta$ and the bottom width of the triangle is $\rho g d$, respectively, where δ is the surcharged pressure head above the pipe crown and d is the distance between the two plates, as depicted in Fig. 6-10. Hence, the total pressure exerted on flow area 2-2 is the summation of the two pressure distribution parts. The total pressure is

$$\gamma A_2 \bar{y}_2 = \gamma(d\delta + \frac{dd}{2}) \tag{6.3}$$

. Hence, the momentum equation (Eq. 15) for the pressure surge wave can be re-written as:

$$\frac{1}{2}y_1^2 - (d\delta + dd/2) = \frac{1}{g}y_1(V_1 + c)(V_2 - V_1) \tag{6-4}$$

Coupling this equation with continuity equation (Eq. 6-1), and using the same boundary condition at the downstream end, namely $V_2 = 0$ due to gate closure, the surge speed and height are solved.

www.manaraa.com

6.2.2.Pressurization Wave Initial Steady State Computation

A similar approach to Section 6.1.2 is used to generate an initial steady state flow field for this simulation. However, a larger flowrate and a smaller downstream depth are used in this case so that the combination of the flowrate and depth would induce a surge that reaches the top wall, creating the pressurization wave.

The downstream boundary type is an outflow boundary in the initial steady state computation process. The upstream boundary type is a velocity inflow. The Froude number for this problem remains less than one. Hence the flow in this simulation is subcritical. A downstream flow depth is specified and the associated pressure at the outlet is hydrostatic. Similar to the open channel bore case, at the inlet a uniform velocity profile is calculated based on the pre-defined flowrate for water and air once the depth is known from the computation. The bottom and top wall for the main domain are free-slip. All walls in the manhole domain are non-slip. The top of the manhole is open boundary.

The steady-state convergence criteria are $10^{-6} m/s$ for the velocity and $10^{-4} pa$ for the pressure. The density and viscosity for the water and air phases are the same as in the open channel bore case in section 6.1. At steady-state, the velocity profile at the outlet of the main pipe is shown in Fig. 6.11.

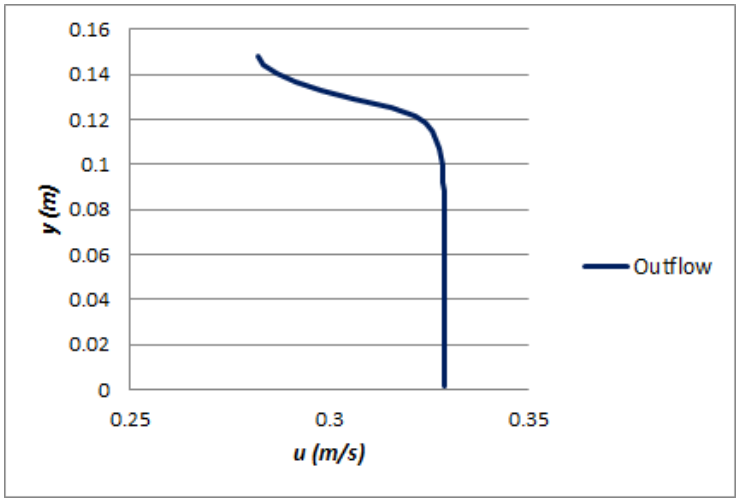

Figure 6. 11 Steady State velocity profile at the outlet of main pipe in pressure wave simulation.

www.manaraa.com

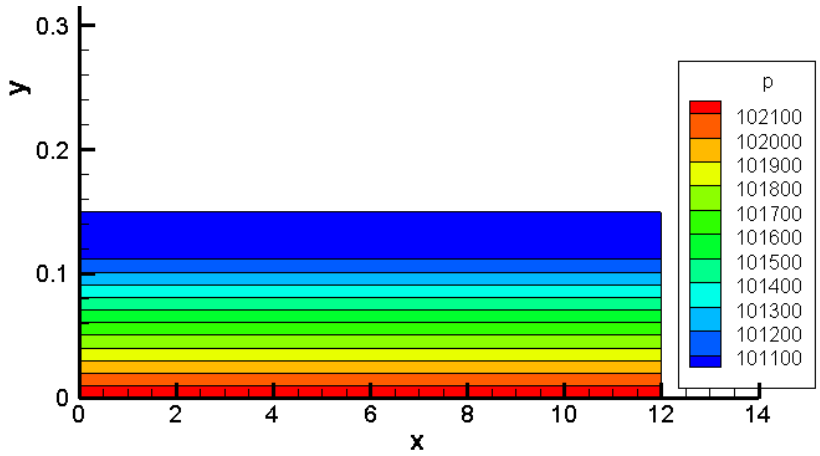

Figure 6. 12 Steady state pressure field in pressure wave simulation

As indicated by Fig. 6.12, at steady-state, the flow has a depth of *0.12198* m and a mean velocity of *0.3279m/s* for the water. The pressure distribution at steady-state is plotted in Fig. 6.12. The pressure is hydrostatic, as expected for uniform open channel flow.

6.2.3.Pressurization Surge Wave Simulation

Once the initial steady-state is reached, the downstream boundary is changed from outflow to a non-slip solid wall at $t=0^{+}$. A pressure surge wave forms instantaneously and starts propagating upstream. Flow depth at downstream starts rising until it touched the top wall and formed a pressure wave. The computation ends when the wave reaches the manhole domain. Other boundary conditions for both main domain and manhole domain remain the same as in the initial steady state run. Figure 6.13 compares the pressures predicted by the numerical model and the analytical pressure head at pressure recording points *P6*, *P9* and *P13*, located *3/8L*, *9/16L* and *13/16L* downstream from the inlet, respectively. Here $L = 12m$. It can be seen from the plot that the numerical prediction matches the analytical solution closely.

The same filter process (time averaging) presented in the open channel bore case is used to analyze the surge head results. The surge head history series after $t = 6s$ from the numerical estimation are averaged to obtain a mean value. The filtered pressure head values from the model are compared to the theoretical results, summarized in Table 6.2. The calculated surge speeds are

www.manaraa.com

compared with the theoretical values at pressure points *6*, *9* and *13*, shown in Table 6.2, and. As seen in this table, the numerical predictions match the theoretical values well.

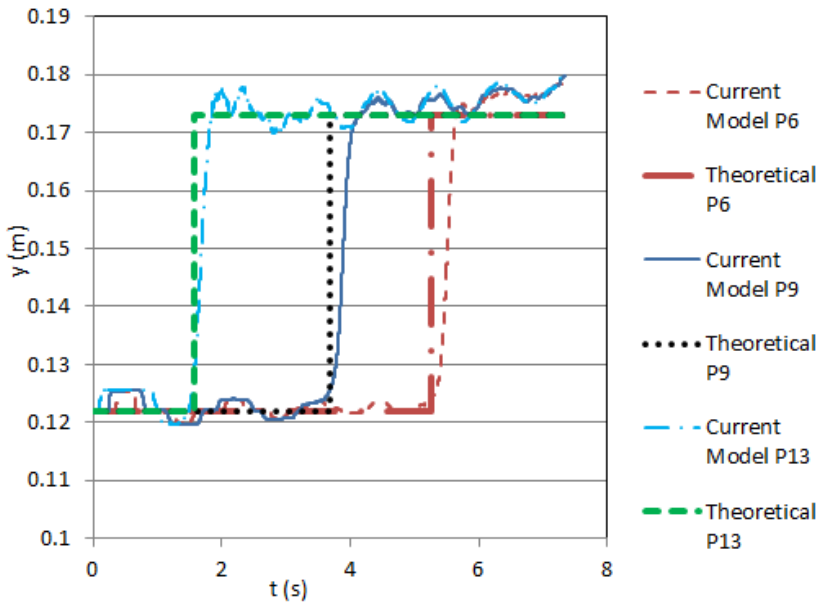

Figure 6. 13 Comparison of numerical and theoretical solutions of surge front in pressure wave simulation.

Table 6.1 Comparison between the numerical prediction and theoretical solution of wave speed and height for a pressure surge wave (grid size *320* x *40*).

	Current Model			**Theoretical**
	P6	**P9**	**P13**	-
Location (m)	4.5	6.75	9.75	-
Front Reaching Time (s)	5.4	3.8	1.67	-
Surge Speed (m/s)	-1.389	-1.382	-1.347	-1.428
Surge Height (m)	0.1766	0.1766	0.1766	0.1730

www.manaraa.com

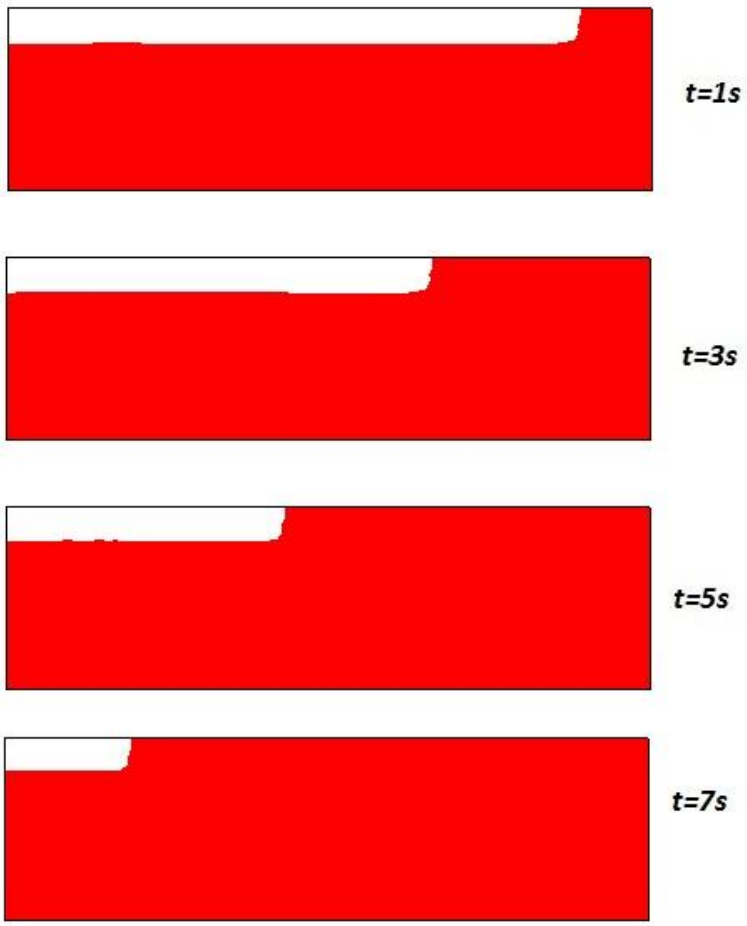

Figure 6. 14 Instantaneous interface at time t=1s, 3s, and 5s in pressure wave surge simulation.

Figure 6.14 plots the instantaneous interface at time *t = 1s, 3s, 5s* and *7s*. A steep surge front is observed from the plot, as expected in the horizontal channel.

www.manaraa.com

6.2.4.Pressurization Wave Grid Convergence Test (GCT)

To measure the convergence performance of the model, an additional simulation with a coarser grid (*160* x *40*) is performed for the same channel flow. In Figures 6.16 and 6.17, the surge head predicted by the two different grid sizes are plotted along with the theoretical solution. As shown in Figs. 6.15 and 6.16, as the grids get refined, the numerical prediction gets closer to the theoretical solution. This indicates that the numerical simulation is converging.

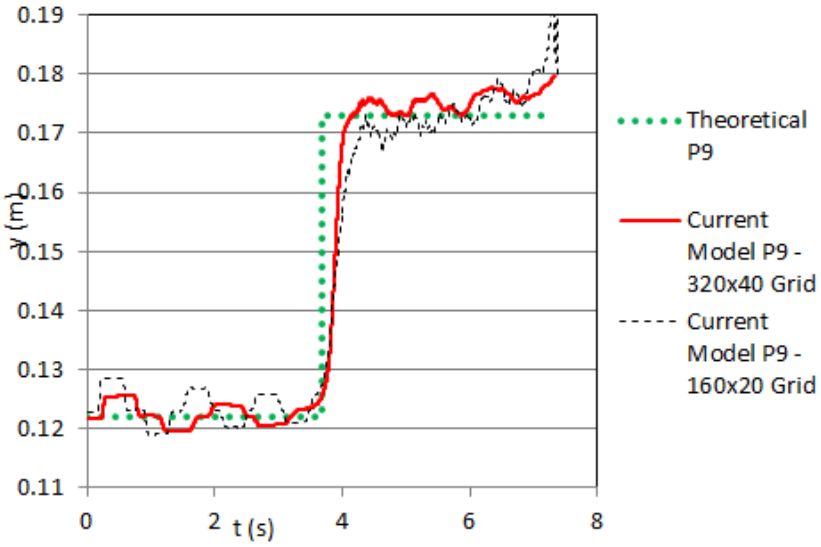

Figure 6. 15 Grid convergence test for open channel bore simulation at pressure recording point P9.

www.manaraa.com

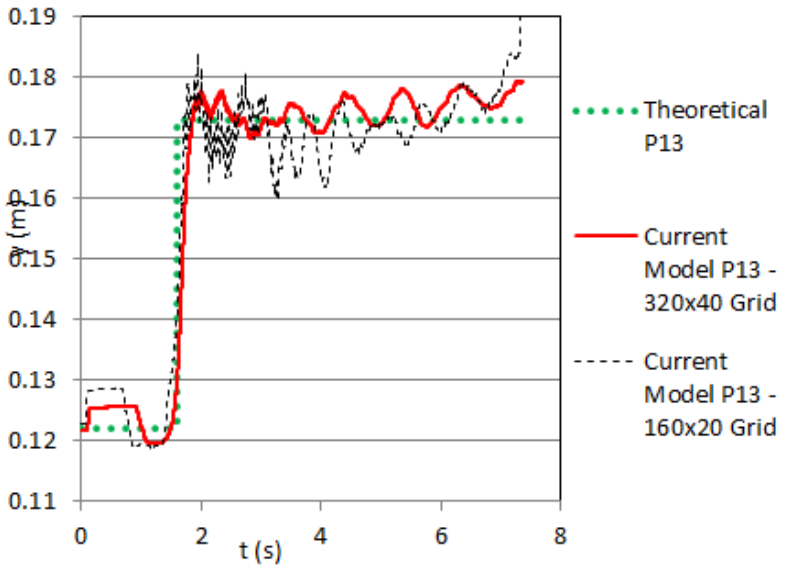

Figure 6. 16 Grid convergence test for open channel bore simulation at pressure recording point P13.

www.manaraa.com

CHAPTER 7 GEYSER SIMULATION

This chapter contains a series of simulations that investigate the air pocket rising dynamics in a vertical riser from different perspectives. The simulations explore the primary geyser driving mechanism from the following respects: buoyance, air compressibility, momentum inertia and pressure. Each section in this chapter represents one respective. In each section, the simulation cases and setups are laid out first followed by the numerical results and discussion. The numerical findings of the key factors that form a geyser and affect the geyser strength are discussed in the conclusion section.

The two phases in this chapter are water and air. For all simulations, the densities of water and air in the simulation are $1000kg/m^3$ and $1.23kg/m^3$, respectively. Viscosities of water and air are $1.0x10^{-3}kg/m{\cdot}s$ and $1.8\times10^{-5}kg/m{\cdot}s$, respectively, with gravity being $9.8m/s^2$. The pressure values used are gauge pressures (relative pressure).

7.1. Buoyance Effects

The first simulation investigates the air pocket rising motion that is purely induced by buoyancy effect. In this case, an air pocket is initially at rest and contained below a stagnant water column in a vertical riser, as shown in Fig. 7.1, by a hypothetical rigid film. Initially, the air occupies the bottom of the manhole with a height H_a. The initial water column height is H_w. At $t = 0^+$, the film is removed and the air pocket starts rising in the vertical riser due to buoyancy effect.

In this case, the initial pressure within the air pocket (P_0) equals the hydrostatic pressure from the water column height, namely, $P_0 = \rho g H_w$. The bottom boundary is a non-slip solid wall. Hence the air pocket is in a close system without extra air mass entering the air pocket. These two conditions isolate the air rising motion, driven only by buoyancy. Although compressibility exists in any close air system, the impacts of air compressibility are reduced by setting the initial pressure to hydrostatic.

www.manaraa.com

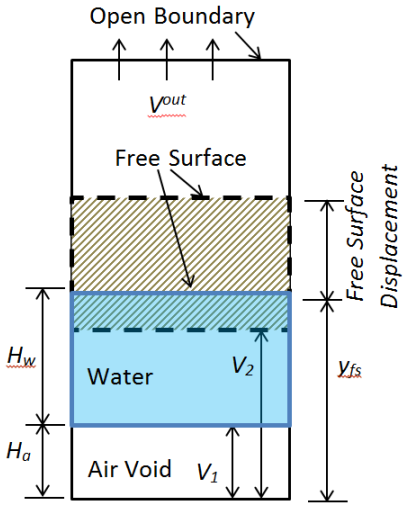

Figure 7. 1Computational domain for rising air pocket simulation.

The expansion of the air pocket is determined using the ideal gas law. Assuming the air pocket undergoes a pseudo-adiabatic expansion and compression process, the relationship between the air pressure p and the volume (V) inside the bubble follows the ideal gas law, namely:

$$p^{n+1}V^{n+1} = p^nV^n \tag{7.1}$$

Here p^{n+1} and V^{n+1} represent the absolute pressure and air pocket volume at time step $n+1$, respectively, while p^n and V^n represent the absolute pressure and volume at time step n. The resulting pressure within the air pocket is used as a reference pressure in the solution of the Pressure Poisson Equation. The location of the reference point is assumed to be at the bottom center in the air pocket.

At time step $n+1$, substituting the known (time step n) absolute pressure and the volume with the calculated volume at the new time step, the resulting absolute pressure at the new time step can be calculated. The volume of the air pocket at the new time step V_a^{n+1}, is calculated based on volume conservation. Hence the air pocket at the new time step V_a^{n+1} equals the air pocket volume at the previous time step V_a^n plus the volume of air expelled from the system V_a^{out} (air escaping the top boundary) during each time step. This can be written as

$$V_a^{n+1} = V_a^n + V_{out}^n \tag{7.2}$$

www.manaraa.com

There are two distinctive interfaces between the water and air phases. The first interface is the top surface of the water column that contacts with the atmosphere. This interface is referred to as the free surface. The second interface is between the water column that is on top of the air pocket and the air pocket itself. This interface is referred to as the air pocket front or air pocket nose. The upward speed of the free surface can be calculated based on the displacement of the free surface in any time interval (t_1 and t_2) as

$$v_{fs} = \frac{y_2 - y_1}{t_2 - t_1} \tag{7.3}$$

The free surface height refers to the maximum *y*-coordinate value of the free surface. The free surface displacement refers to the distance between the initial elevation and final elevation of the free surface when the air pocket breaks through the top water column, or escapes.

The geyser strength is often defined as the elevation of the free surface height at the instant that the air pocket breaks through the free surface. The free surface height is normalized by the initial pressure head using

$$y_{fs}^* = \frac{y_{fs}}{P_0} \tag{7.4}$$

The free surface displacement D_{fs} is also normalized using the initial pressure head by defining

$$D_{fs}^* = \frac{D_{fs}}{P_0} \tag{7.5}$$

The computational domain of the riser is *0.1m* wide and *4.0m* tall. The initial height of the air void is *0.5m*. The initial height of the water column is *1.0m*, which results in an initial pressure head of *1.0m*, or *9800pa* in the air pocket. The grid size is *20* x *160* with a time step of 5×10^{-5} s. In the simulation, all the walls in the riser domain are non-slip. The top boundary of the riser is an open boundary. Table 7.1 lists the numerical parameters and initial conditions used in this simulation, labeled as Case 1. Table 7.1 also shows the numerical results in the buoyance-induced air pocket rising simulation.

www.manaraa.com

Table 7. 1 Simulation parameters and results in buoyance effects simulation

Case Name	*Case 1*
Bottom Boundary Condition	*Non-slip wall*
Grid Size	*20x160*
Domain Size *(L x H) (m)*	*0.1 x 4.0*
Time Step Size (*s*)	*5x10-5*
Omega in SOR	*1.92*
Shumann Filter beta Value	*1000*
Water Column Height H_w *(m)*	*1*
Initial Air Void Height H_A *(m)*	*0.5*
Initial Pressure Head within Air Void P_0 *(m)*	*1*
Initial Free Surface Location (*m*)	*1.5*
Time at breakthrough (*s*)	*2.5*
Free Surface Height at break through (*m*) - y_{fs}	*1.51*
Free Surface Displacement at break through (*m*) - D_{fs}	*0.01*
Free Surface Velocity at breakthrough (*m/s*)	*0.4*
Free Surface Height at break through normalized by the initial pressure head - y^*_{fs}	*1.5*
Free Surface Displacement at break through normalized by the initial pressure head - D^*_{fs}	*0*

Figure 7.2 plots snapshots of the interface during the air pocket rising. It can be seen from Fig. 7.2 and Table 7.1 that when the air pocket breaks through the surface, the free surface increment is negligible. The buoyancy leads to a mixture of water and air without significant momentum being generated or exchanged.

As shown in Table 7.1, the speed of the free surface reached *0.4m/s* when the air pocket broke through the surface. This speed has the same magnitude of a Taylor bubble. According to Davies and Taylor (1950), the speed of a rounded nose Taylor bubble in a vertical cylindrical tube has a velocity of

$$v = 0.35\sqrt{(gD)} \tag{7.6}$$

www.manaraa.com

where, g is gravity and D is the diameter of the tube. The speed of a Taylor bubble in this configuration is calculated to be *0.35 m/s*. This speed is fairly low comparing to a typical water air mixture jet speed in a geyser, which is generally in the order of *10 ~ 20 m/s*. This indicates that the momentum generated by buoyance is minor. Buoyancy effects, while adding to geyser strength, are clearly not a dominate influence on geysers.

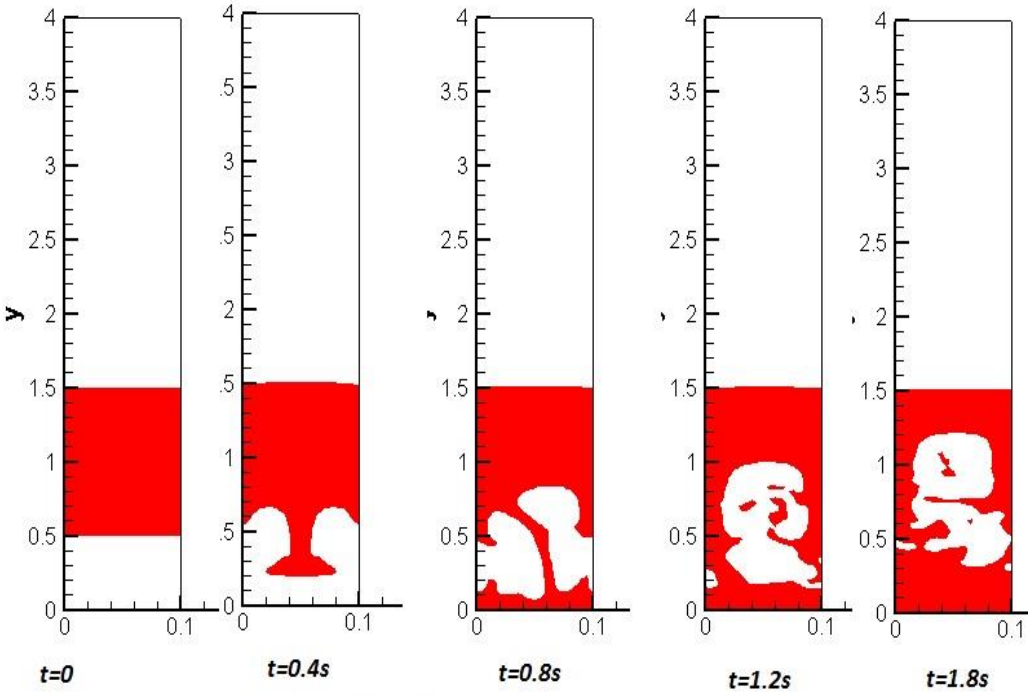

Figure 7. 2 Buoyance effects: evolution of interface of case 1

7.2. Air Compressibility Effects

The second rising motion involves an air pocket that has been compressed by a higher pressure. In this simulation, the domain is the same as in Fig. 7.1 which contains an air pocket initially at rest under a stagnant water column. However, in this case, the air pocket is initially compressed by a pressure that is higher than the hydrostatic pressure from the above water column (in these cases, twice the hydrostatic pressure). In this simulation, the bottom boundary is also a non-slip solid wall. Hence the air pocket is a close system. These two conditions isolate the air rising motion caused by air compressibility from other driven factors.

www.manaraa.com

Two cases are simulated in this section, namely, Case 2.A and 2.B. The two cases have the same domain size, water column depth and initial pressure values within the air pocket. The only difference is the initial air volume. The initial air pocket volume in Case 2.B is twice as large as in Case 2.A. This is to study the relation between free surface rising height and the air pocket volume.

Table 7.2 lists the initial conditions and other numerical parameters such as domain size, grid size and time step size used in the compressibility effects simulations.

Table 7. 2 Simulation parameters and results in compressibility effects simulation

Case Name	*Case 2.A*	*Case 2.B*
Bottom Boundary Condition	*Non-slip wall*	*Non-slip wall*
Grid Size	*20x160*	*20x160*
Domain Size *(L x H) (m)*	*0.1 x 4.0*	*0.1 x 4.0*
Time Step Size (*s*)	$5x10^{-5}$	$5x10^{-5}$
Omega in SOR	*1.92*	*1.92*
Shumann Filter beta Value	*1000*	*1000*
Water Column Height H_w *(m)*	*0.5*	*0.5*
Initial Air Void Height H_A *(m)*	*0.5*	*1*
Initial Pressure Head within Air Void P_0 *(m)*	*1*	*1*
Initial Free Surface Location (*m*)	*1*	*1.5*
Time at breakthrough (*s*)	*1.3*	*1.3*
Free Surface Height at break through (*m*) - y_{fs}	*1.05*	*1.65*
Free Surface Displacement at break through (*m*) - D_{fs}	*0.05*	*0.15*
Free Surface Velocity at breakthrough (*m/s*)	*1.1*	*2.3*
Free Surface Height at break through normalized by the initial pressure head - y^*_{fs}	*1.05*	*1.65*
Free Surface Displacement at break through normalized by the initial pressure head - D^*_{fs}	*0.05*	*0.15*

www.manaraa.com

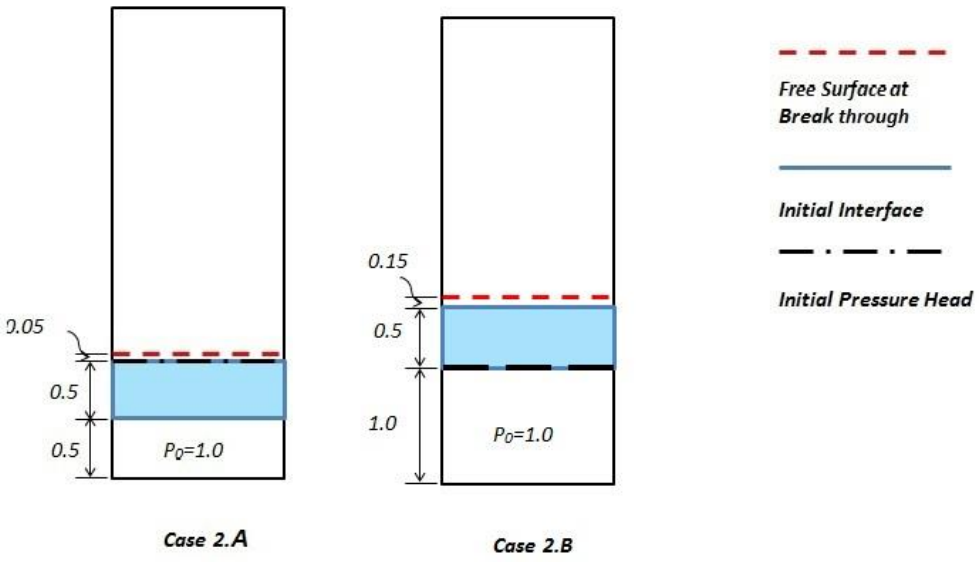

Figure 7. 3 Compressibility effects: Free Surface locations at breakthrough for cases 2.A and 2.B.

Figure 7.2 plots the initial and final free surface locations at times when the air pocket breaks through. Table 7.2 summarizes the numerical results in the buoyance-induced air pocket rising simulation.

It can be seen from Figure 7.3 and Table 7.2 that when the air pocket breaks through the surface, the free surface lifted by the air pocket expansion is still insignificant. In both cases, the free surface is pushed up slightly. The speed of the air pocket front reaches *1.1m/s* in Case 2.A and *2.2m/s* in Case 2.B at time when the air pocket breaks through the surface. Although this speed is still fairly low comparing to a typical geyser jet speed, it is higher than the speed of a Taylor bubble in the buoyance-induced air pocket rising case (Case 1). This indicates that the momentum generated by the air pocket expansion is higher than the buoyancy.

Figure 7.3 also indicates a larger initial air pocket volume induces a higher free surface height and free surface speed, for example, Case 2.B. This is consistent with what we would expect since a larger compressed air pocket "stores" more energy. The relation between geyser strength and air pocket size is further investigated in Section 7.4.

www.manaraa.com

Figure 7.4 plots the pressure within the air pocket as it rises in the water. As expected, the pressure with the air pocket approaches atmosphere pressure as the air pocket approaches the free surface. The sinusoidal variation of pressure head shown in this plot could be related to the transients initiated by the expansion/contraction during the air pocket rising.

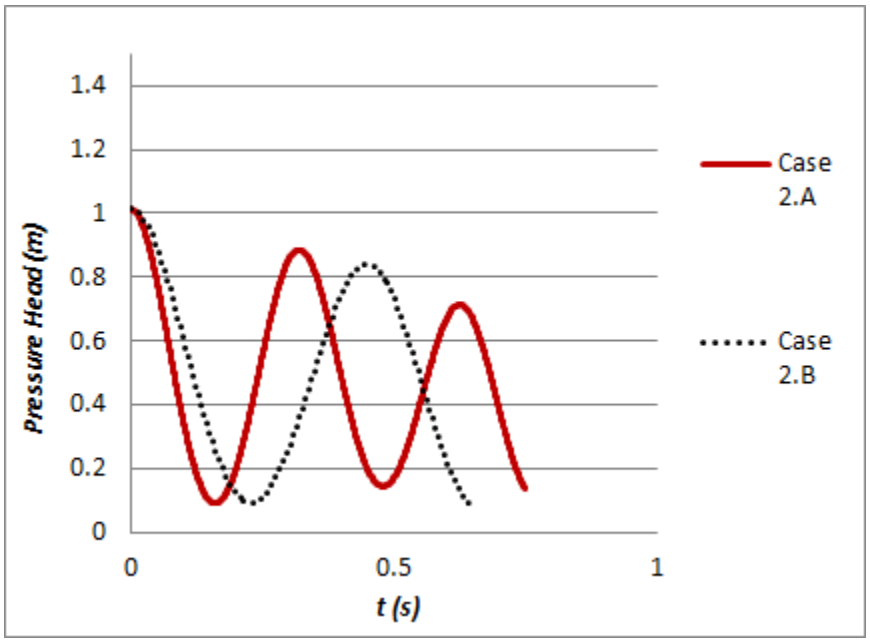

Figure 7. 4 Compressibility effects: pressure head history at riser bottom for case 2.A and case 2.B.

7.3. Inertia Effects

In this section, the air rising motion is induced by inertia that is fed to the vertical riser. In real stormwater system, the source of the inertia is from the main pipe. In this case, the air pocket is initially contained under a water column under hydrostatic pressure. However, the bottom boundary is a velocity inflow boundary with a uniform inflow profile. This configuration is similar to a manhole that has a continuous momentum input from the main pipe through a large air pocket, similar to a plug flow in the main pipe. This scenario occurs when a portion of a air pocket is pushed into the manhole by a pressurization wave front, similar to what is simulated in Chapter 6.

www.manaraa.com

Three cases are simulated in this section. The differences between these cases are in the water column depth and the inflow velocity. Case 3.A is considered to be a base case and is used as a baseline for comparison. Case 3.B is to study the relation between the geyser strength and the initial surcharged state in the riser. Since the initial water column height represents the initial surcharged state within the manhole, this case contains a water column that is twice as tall as in Case 3.A. The taller of the initial water column, the more the system is surcharged. Case 3.C is to study the relation between the geyser strength and the inertia input from the main pipe. The velocity inflow in Case 3.C is *1.5* times higher than in Case 3.A.

Table 7. 3 Simulation parameters and results in momentum inertial effect simulation.

Case Name	*Case 3.A*	*Case 3.B*	*Case 3.C*
Bottom Boundary Condition	*Uniform Velocity Inflow*	*Uniform Velocity Inflow*	*Uniform Velocity Inflow*
Inflow Velocity (*m/s*)	*2.0*	*2.0*	*3.0*
Grid Size	*20x160*	*20x320*	*20x160*
Domain Size *(L x H) (m)*	*0.1 x 4.0*	*0.1 x 8.0*	*0.1 x 4.0*
Time Step Size (*s*)	$5x10^{-5}$	$5x10^{-5}$	$5x10^{-5}$
Omega in SOR	*1.9*	*1.95*	*1.9*
Shumann Filter beta Value	*1000*	*1000*	*1000*
Water Column Height H_w *(m)*	*0.5*	*1.0*	*0.5*
Initial Air Void Height H_A *(m)*	*0.5*	*0.5*	*0.5*
Initial Pressure Head within Air Void P_0 *(m)*	*1.0*	*1.0*	*1.0*
Initial Free Surface Location (*m*)	*1.0*	*1.5*	*1.0*
Time at breakthrough (*s*)	*0.77*	*1.4*	*0.325*
Free Surface Height at break through (*m*) - y_{fs}	*2.6*	*4.3*	*2.4*
Free Surface Displacement at break through (*m*) - D_{fs}	*1.6*	*2.8*	*1.4*
Free Surface Velocity at breakthrough (*m/s*)	*2.0*	*2.0*	*4.8*

www.manaraa.com

Table 7.3 lists the initial conditions and other numerical parameters used in the momentum effect simulations. Table 7.3 also summarizes the numerical results. Figures 7.5 through 7.7 plot the evolution of the interface in Case 3.A through 3.C, respectively.

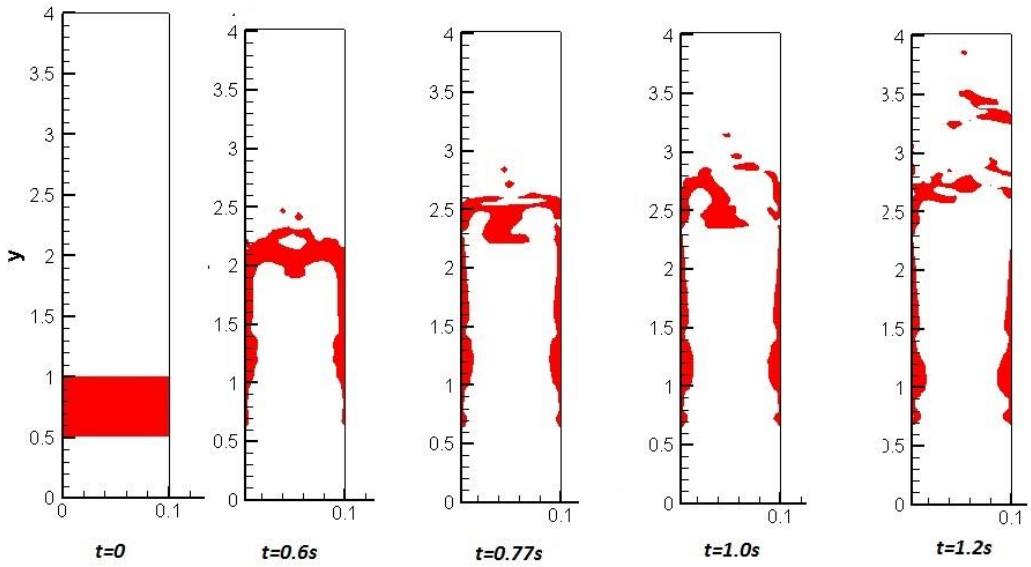

Figure 7. 5 Inertia effects: evolution of interface of case 3.A.

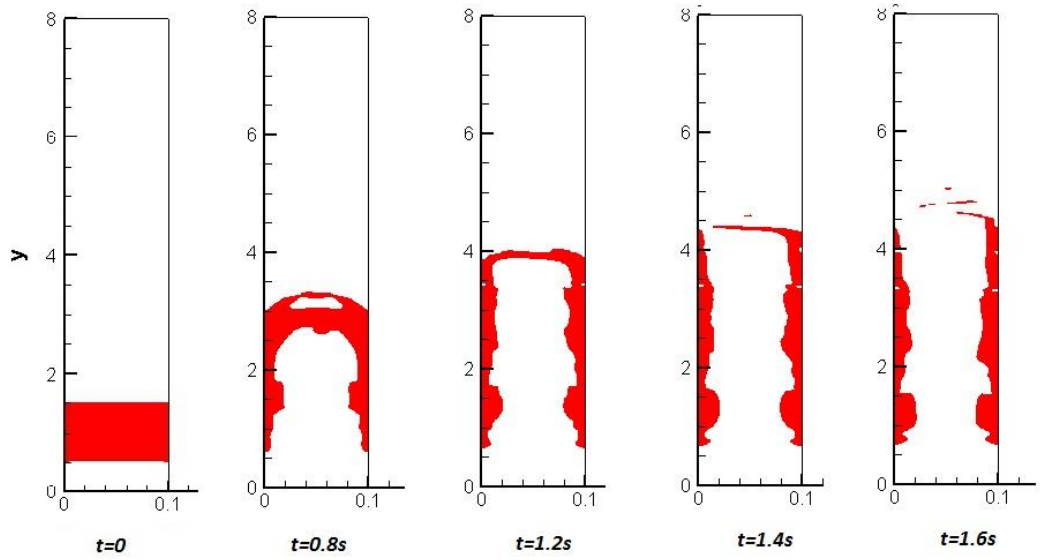

Figure 7. 6 Inertial momentum effects: evolution of interface of case 3.B.

www.manaraa.com

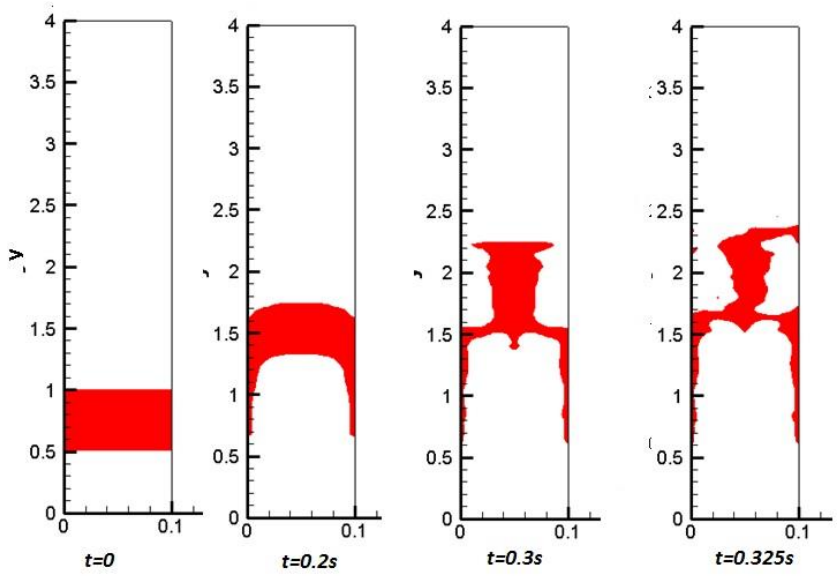

Figure 7. 7 Inertia effects: evolution of interface of case 3.C.

To better compare the numerical results, the initial and final free surface locations at breakthrough are plotted in Fig. 7.8.

It can be seen from Fig. 7.8 that when the air pocket breaks through, the free surface is pushed up to an elevation that is much higher than the previous two sections (Section 7.1 and 7.2). In all cases, the free surfaces go up significantly with a moderate speed. From Table 7.3, it can be seen that the speed of the interface reached 2.0m/s in Case 2.A, 2.2m/s in Case 2.B and 4.8m/s in Case 3.C when the air pocket breaks through the surface. It appears that the speed of the interface is related to the inflow velocity. This is as expected since momentum from the air inflow is transferred to the surrounding water column as the air pocket rising. This speed is still low comparable to a typical geyser jet speed. However, it is higher as compared to the air rising induced by buoyancy (Case 1) and compressibility effects (Case 2.A and B).

This indicates that the momentum transferred from the main pipe could push water to a fairly high elevation with a moderate speed. Hence momentum transferred from the main pipe has an important influence on the geyser strength.

www.manaraa.com

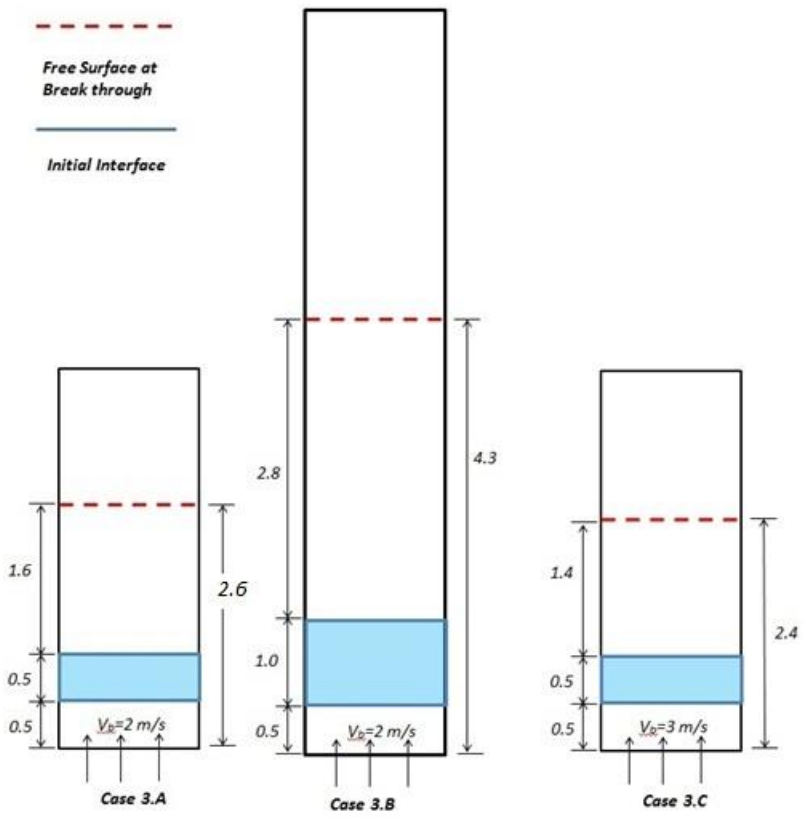

Figure 7. 8 Inertia effects: free surface locations at breakthrough of case 3.A, 3.B and 3.C.

Some factors that determine geyser strength can be observed by comparing Case 3.A and 3.C. Case 3.C contains a higher inflow, symbolizing "more" momentum transported from the main pipe. However, this higher momentum does not lead to a higher free surface elevation at breakthrough, i.e. geyser strength. This is because the time to breakthrough is much less in the higher velocity case. A higher inflow velocity yields a higher relative velocity at the air front (air nose) that penetrates through the water volume. It only takes Case 3.C *0.325sec* to break through the surface, whereas in Case 3.A it takes *0.77sec*. Similarly, a larger initial water column height, such as in Case 3.B, induces a higher (normalized) free surface elevation, as indicated in Fig. 7.8. This is because a larger column height means longer distance for the air pocket to penetrate through. The longer traveling time within the water column also promotes a higher free surface. This shows that the timing at breakthrough is another key factor in the determination of the geyser strength.

www.manaraa.com

Figure 7.9 plots the interface displacement of the air pocket as it rises. As indicated by this figure that the free surface rises with an almost constant speed, which is consistent with the momentum driven mechanism and the plug flow theory. As discussed in the Rigid Column method in Chapter 2, plug flow theory is commonly used as a simplification for analyzing mixed-flows and geysers. This would be consistent if the main driving force in geyser events is moment transfer. But the results are not consistent with what is observed in field studies or experiments, where the frontal velocity is much higher.

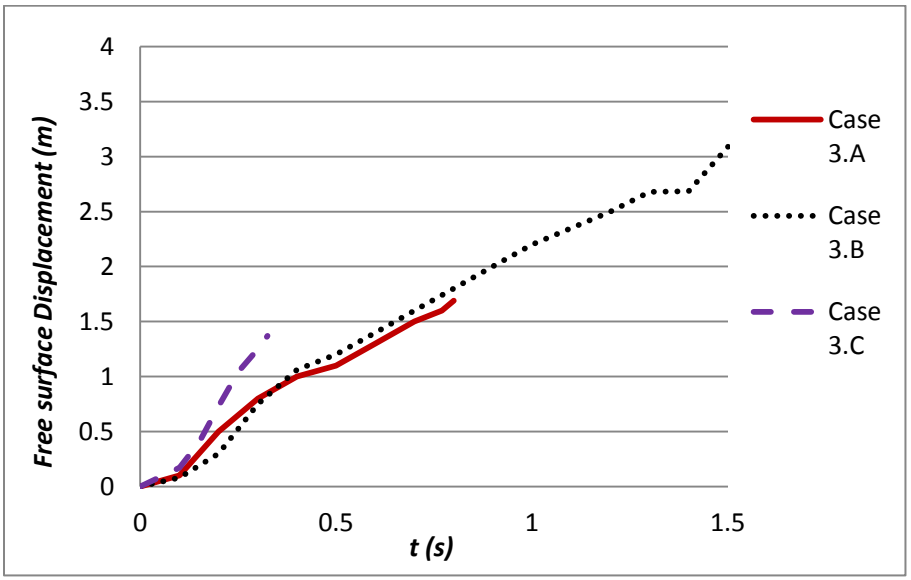

Figure 7. 9 Inertia effects: free surface displacements of case 3.A, 3.B and 3.C

7.4. Air Pocket Size Effects

As indicated in Section 7.2, the size of an air pocket determines the height of the final free surface elevation at breakthrough. In this section, the relations between geyser strength and the size of air pocket are further investigated by studying different scenarios. The air rising motion in this simulation is induced by a compressed air pocket. In this simulation, the domain is the same as in Fig. 7.1. Three scenarios are simulated in this section, including air pockets with infinite volume, small volume and significantly large, but not infinite, volume. Based on Ideal Gas law (Eq. 7.1), an infinite volume leads to a constant pressure within the air pocket as the air pocket expands. Vice versa, a constant pressure indicates an air pocket has an infinite volume. In real world, these

www.manaraa.com

configurations are similar to a manhole that contains continuous air inflow from the main pipe. These scenarios occur when a portion of a large air pocket is pushed into the manhole by a pressurization wave front while the rest of the air pocket, namely, air pocket tail, is still contained in the main pipe.

7.4.1. Infinite Size Air Pocket

The first scenario contains a hypothetical air pocket that has an infinite volume. This scenario is simulated by specifying a fixed (over time) pressure inflow boundary at the bottom boundary, which means a continuous air inflow. Although the air volume is assumed infinite, this configuration is very similar to a pressurized stormwater system with a manhole that initially surcharged. The pressure at the bottom of the manhole (inflow boundary) is controlled by the pressure head in the main pipe. In this case, the main pipe is pressurized with a pressure head higher than the hydrostatic pressure and remains constant.

Three cases are simulated in this section, as shown in Table 7.4. Table 7.4 lists the initial conditions and other numerical parameters used in these simulations.

Case 4.1.A is a base case and used as a baseline for comparison. Case 4.1.B contains a specified pressure value at the inflow boundary that is twice as high as in Case 4.1.A. Case 4.1.B is to study the relation between geyser strength and the initial pressurization state in the main pipe. Case 4.1.C. contains a water column that is twice as tall as in Case 4.1.A. Case 4.1.C is to investigate geyser strength and the initial surcharged state of the manhole, which is represented by the initial water column height.

Table 7.4 summarizes the numerical results in the compressed air pocket with infinite size simulation. Figures 7.10 through 7.12 plot the instantaneous interfaces of all cases. A thin layer of film flow around the rising air pocket can be seen from the interface evolution plots. The film flow results in a reduced water volume above the air. The reduced water column weight further accelerates the air rising. When the free surface breaks up, the air flow mixes with the falling water column and forms a water-air mixture.

www.manaraa.com

Table 7. 4 Simulation parameters and results in infinite size air pocket simulation

Case Name	*Case 4.1.A*	*Case 4.1.B*	*Case 4.1.C*
Bottom Boundary Condition	*Pressure inflow – fixed value*	*Pressure inflow – fixed value*	*Pressure inflow – fixed value*
Grid Size	*20x160*	*20x320*	*20x320*
Domain Size *(L x H) (m)*	*0.1 x 4.0*	*0.1 x 8.0*	*0.1 x 8.0*
Time Step Size (*s*)	$5x10^{-5}$	$5x10^{-5}$	$5x10^{-5}$
Omega in SOR	*1.9*	*1.9*	*1.95*
Shumann Filter beta Value	*1000*	*1000*	*1000*
Water Column Height H_w *(m)*	*0.5*	*0.5*	*1.0*
Initial Air Void Height H_A *(m)*	*0.5*	*0.5*	*0.5*
Initial Pressure Head within Air Void P_0 *(m)*	*1.0*	*2.0*	*2.0*
Initial Free Surface Location (*m*)	*1.0*	*1.0*	*1.5*
Time at breakthrough (*s*)	*0.57*	*0.37*	*0.78*
Free Surface Height at break through (*m*) - y_{fs}	*2.8*	*3.13*	*4.3*
Free Surface Displacement at break through (*m*) - D_{fs}	*1.8*	*2.1*	*3.58*
Free Surface Velocity at breakthrough (*m/s*)	*10.0*	*18.5*	*15.7*
Free Surface Height at break through normalized by the initial pressure head - y^*_{fs}	*2.8*	*1.57*	*2.54*
Free Surface Displacement at break through normalized by the initial pressure head - D^*_{fs}	*1.8*	*1.07*	*1.79*

www.manaraa.com

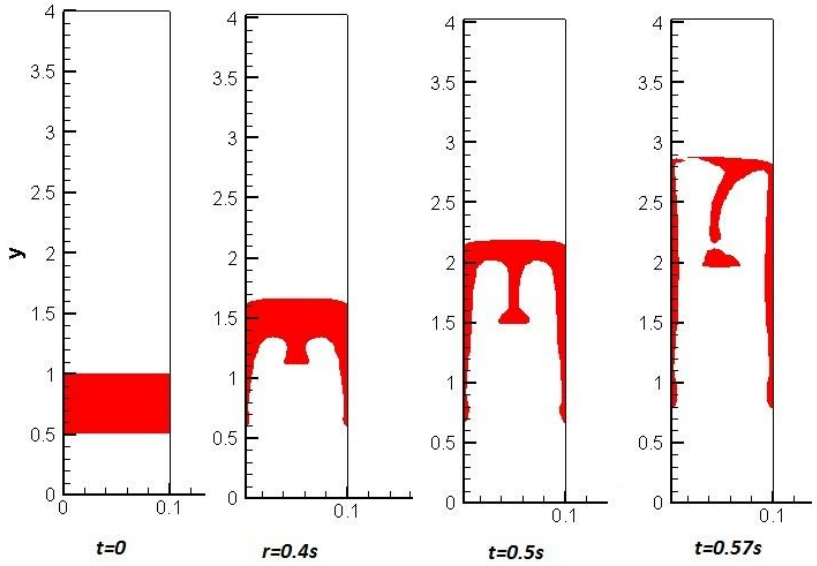

Figure 7. 10 Infinite size air pocket: evolution of interface of case 4.1.A.

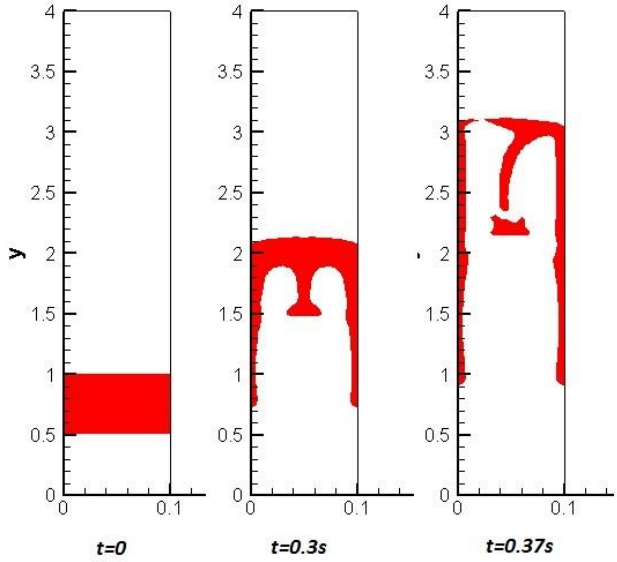

Figure 7. 11 Infinite size air pocket: evolution of interface of case 4.1.B.

www.manaraa.com

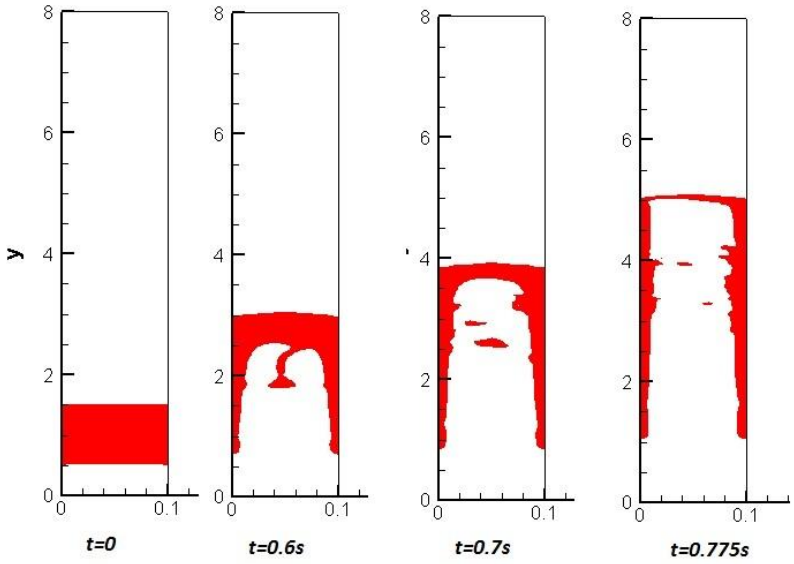

Figure 7. 12 Infinite size air pocket: evolution of interface of case 4.1.C.

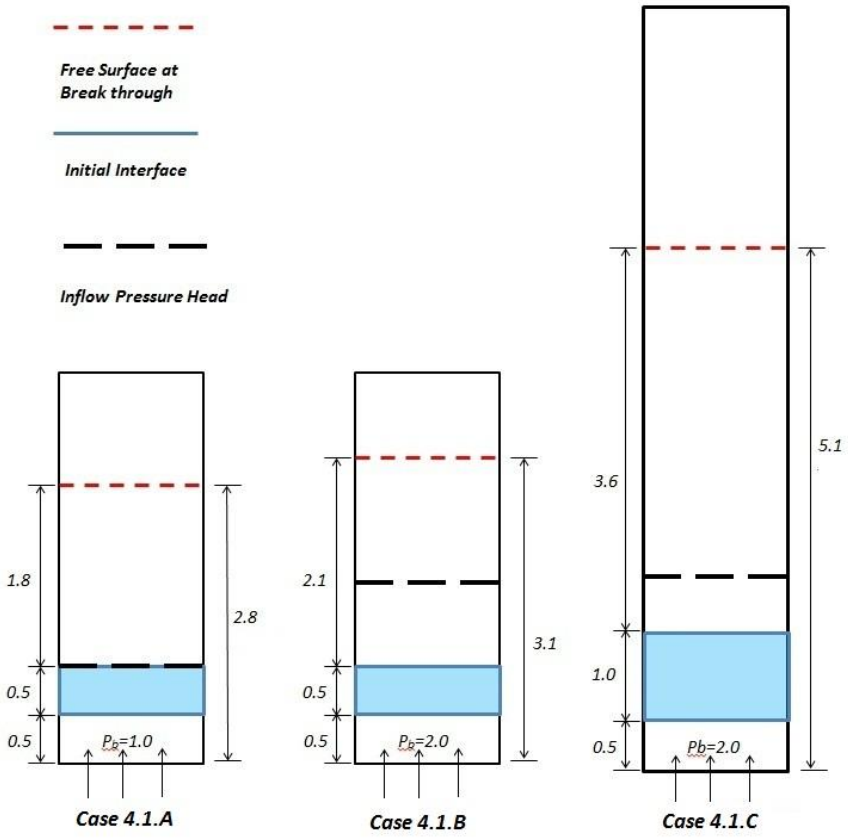

Figure 7. 13 Infinite size air pocket: free surface locations at breakthrough of case 4.1.A, 4.1.B and 4.1.C.

www.manaraa.com

To better compare the numerical results, the initial and final free surface locations at breakthrough are plotted in Fig. 7.13. It can be seen from Fig. 7.13 that when the air pocket breaks through, the free surfaces go up significantly

Flow chaos can be observed in the interface evolution plots in Figs. 7.10 through 7.12 at time of breakthrough. One feature is the extremely high velocity at the air pocket front, as indicated in Table 7.4. The speed of the interface reached *10m/s* in Case 4.2.A, *18m/s* in Case 4.1.B and *16m/s* in Case 4.2.C at the time of breakthrough. These speeds are comparable to a typical geyser jet speed. Comparing to the air pocket rising simulations in section 7.3, which are primarily driven by the momentum inertial, the speed of the surface in this section is significantly higher. This indicates that the momentum generated by a compressed air pocket with an infinite large size is more significant in support of geyser characteristics. This is caused by a significant pressure gradient within the air pocket as it approaches the surface and eventually breaks through. The pressure field at breakthrough in these cases is shown in Figure 7.14.

Because the pressure specified at the inflow boundary represents the pressurization state in the main pipe, a pressure head that is higher than hydrostatic indicates that the main pipe is surcharged. When the air pocket approaches and breaks through the surface, the pressure near the air pocket front drops to atmosphere pressure. This generates a significant pressure gradient between the tail and the nose of the air pocket. Due to the low density and viscosity of the air phase, the pressure gradient results in a huge velocity within the air pocket.

It appears that the momentum transferred by a pressured air pocket with infinite size could lift water column by a significant distance with an extremely high speed. If the breakthrough point is close to the riser opening, the water-air mixture will shoot out of the riser and form a geyser feature.

www.manaraa.com

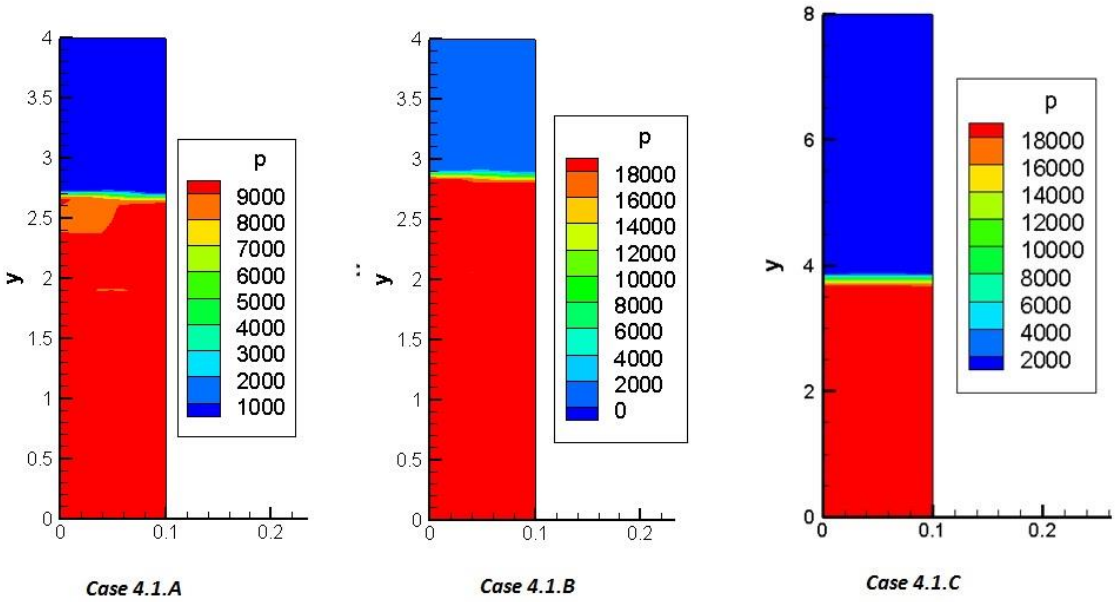

Figure 7. 14 Infinite size air pocket: pressure field at breakthrough.

Figures 7.15 and 7.16 plot the free surface displacement and speed histories. As indicated by these two figures, the free surface rising caused by a compressed air pocket with an infinite size is significant.

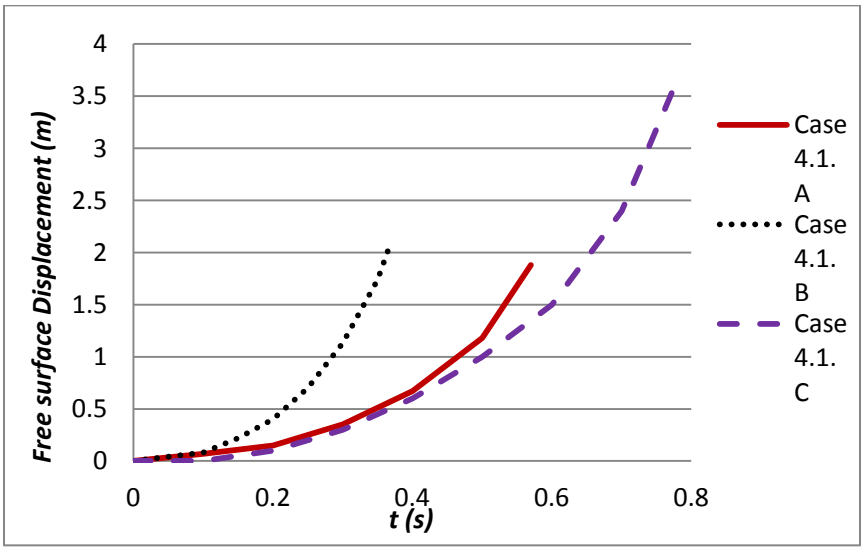

Figure 7. 15 Infinite size air pocket: free surface displacements of case 4.1.A, 4.1.B and 4.1.C.

www.manaraa.com

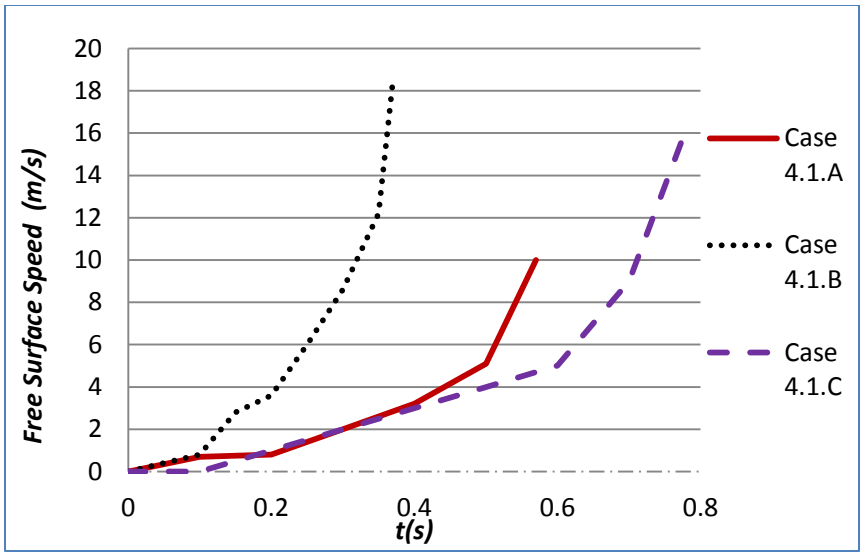

Figure 7. 16 Infinite size air pocket: free surface speeds of case 4.1.A, 4.1.B and 4.1.C

7.4.2. Small Size Air Pocket

The next scenario contains an air pocket with a relatively small volume. The difference between this simulation and the infinite size air pocket simulation in Section 7.4.1 is that, in this section, the pressure value at the inflow boundary changes as the air pocket expands or contracts (due to ideal gas law calculations of Eq. 7.1). This means the pressure at the inflow boundary is not controlled by the main pipe. This is to test the sensitivity of the geyser strength due to different air pocket sizes.

Air compressibility is counted by applying the ideal gas law to solve for a reference pressure. This is done by assuming the tail of the air pocket is still contained in the main pipe (not included in the simulation). The volume of the air pocket initial contained in the main pipe is assumed to be $0.1\ m^3$ in all cases. This volume is twice the size of the air pocket volume in the riser. This symbolizes a very small air pocket because the cross section of a main tunnel is typically much larger than the manhole. The air pocket volume during the rising motion can be calculated from Eq. 7.2. Once the volume is known, a pressure can be calculated based on the ideal gas law (Eq. 7.1). The calculated pressure value is then applied at the pressure inflow boundary and used as a reference pressure. In this way, even though inflow can enter the manhole, the air pocket is still a

www.manaraa.com

close system without extra mass being added. The air pocket volume portion within the manhole can vary based on the pressure values at the inflow boundary.

Three cases are simulated in this section as shown in Table 7.5. Table 7.5 also lists the initial conditions and other numerical parameters used in these simulations.

Table 7. 5 Simulation parameters and results in small size air pocket simulation

Case Name	*Case 4.2.A*	*Case 4.2.B*	*Case 4.2.C*
Bottom Boundary Condition	*Pressure inflow – varied value*	*Pressure inflow – varied value*	*Pressure inflow – varied value*
Grid Size	*20x160*	*20x320*	*20x320*
Domain Size *(L x H) (m)*	*0.1 x 4.0*	*0.1 x 8.0*	*0.1 x 8.0*
Time Step Size (*s*)	$5x10^{-5}$	$5x10^{-5}$	$5x10^{-5}$
Omega in SOR	*1.9*	*1.9*	*1.95*
Shumann Filter beta Value	*1000*	*1000*	*1000*
Water Column Height H_w *(m)*	*0.5*	*0.5*	*1.0*
Initial Air Void Height H_A *(m)*	*0.5*	*0.5*	*0.5*
Initial Air Pocket Volume in Main Pipe (m^3)	0.1	0.1	0.1
Initial Total Air Pocket Volume (m^3)	0.15	0.15	0.15
Initial Pressure Head within Air Void P_0 *(m)*	*1.0*	*2.0*	*2.0*
Initial Free Surface Location (*m*)	*1.0*	*1.0*	*1.5*
Time at breakthrough (s)	*N/A*	*N/A*	*N/A*
Free Surface Height at break through (*m*) - y_{fs} (* Projected)	1.2^*	1.5^*	1.8^*
Free Surface Displacement at break through (*m*) - D_{fs}	*0.2*	*0.5*	*0.3*
Free Surface Velocity at breakthrough (*m/s*)	-	-	-
Free Surface Height at break through normalized by the initial pressure head - y^*_{fs}	*1.2*	*0.75*	*0.9*
Free Surface Displacement at break through normalized by the initial pressure head - D^*_{fs}	*0.2*	*0.25*	*0.15*

www.manaraa.com

Case 4.2.A is considered as the base case used as a comparison baseline. Case 4.2.B contains a initial pressure that is twice as high as in Case 4.2.A. Case 4.2.B is to study the relation between geyser strength and the initial pressurization state in the main pipe, represented by the initial pressure within the air pocket. Case 4.2.C. contains a water column that is twice as tall as in Case 4.2.A. Case 4.2.C is to investigate geyser strength and the initial surcharged state of the manhole, represented the initial water column height.

Table 7.5 summarizes the numerical results in the small size air pocket rising simulations. Figures 7.17 through 7.19 plot the instantaneous interfaces of Case 4.2.A through 4.2.C. It can be seen from the interface plots that the free surface increment are generally minor comparing to the compressed air pocket with an infinite size cases in Section 7.4.1.

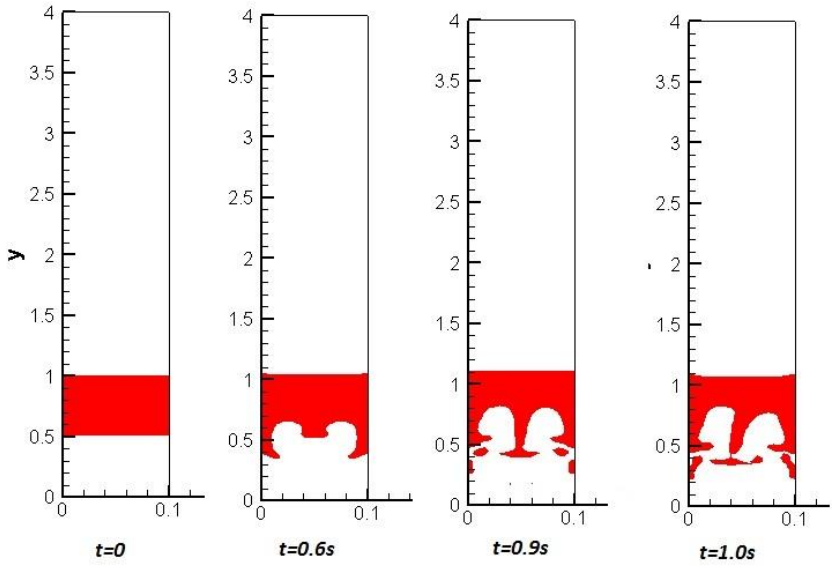

Figure 7. 17 Small size air pocket: evolution of interface of case 4.2.A.

www.manaraa.com

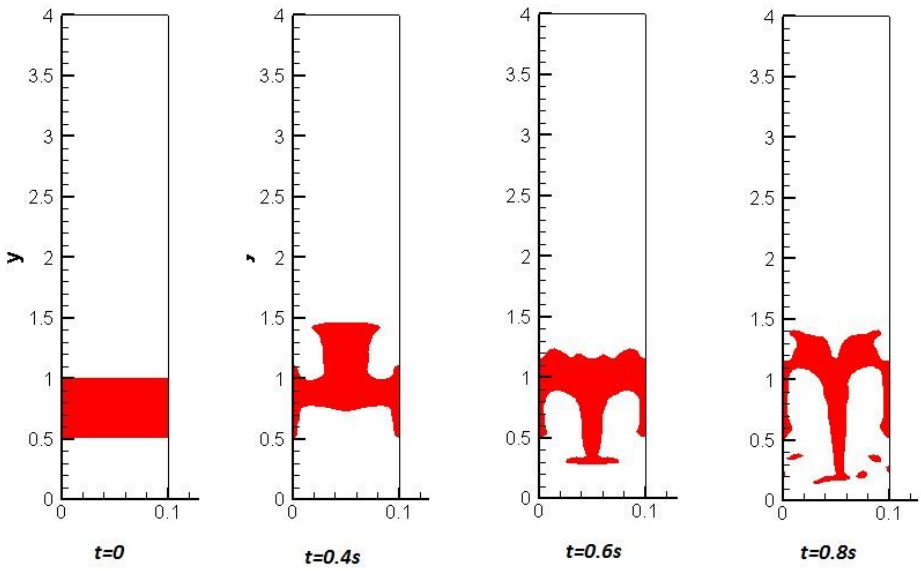

Figure 7. 18 Small size air pocket: evolution of interface of case 4.2.B.

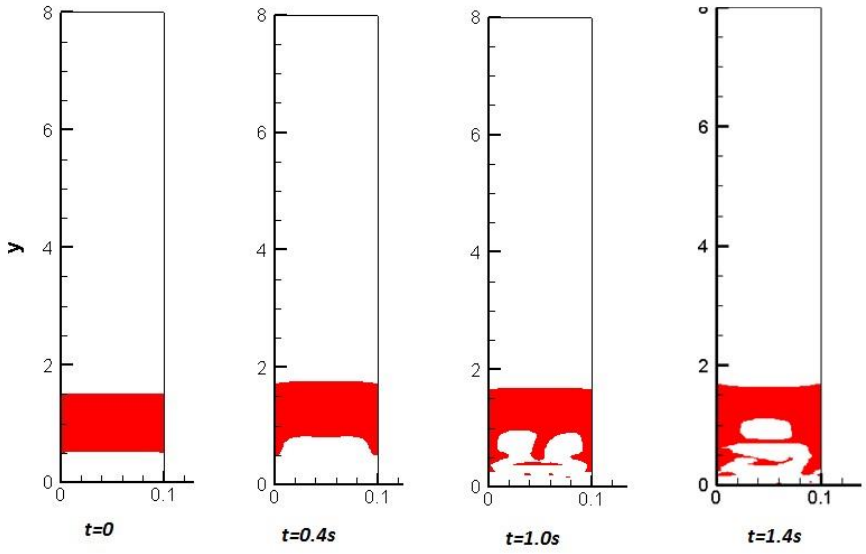

Figure 7. 19 Small size air pocket: evolution of interface of case 4.2.C.

www.manaraa.com

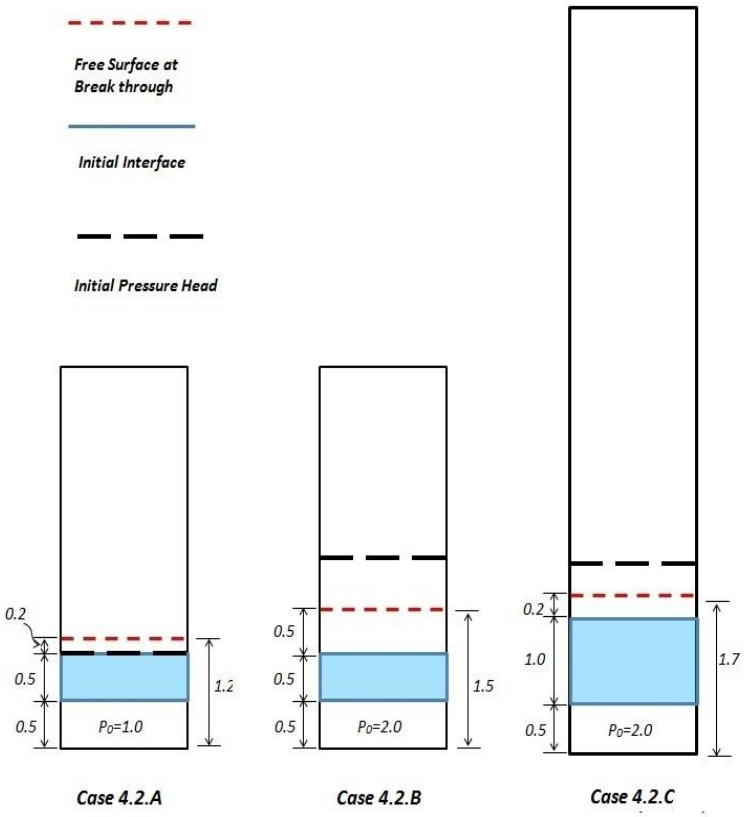

Figure 7. 20 Small size air pocket: free Surface locations at breakthrough of case 4.2.A, 4.2.B and 4.2.C.

Similarly, Fig 7.20 shows the initial and final free surface locations as well as the initial pressure head within the air pocket for comparison purpose.

It can be seen from Table 7.6 and Fig. 7.20 that when the air pocket breaks through, the free surfaces only went up slightly in all cases. This indicates that the momentum transferred by a pressured air pocket of small size might not be sufficient to produce an air water mixture jet with high velocity, as seen in a geyser.

Figure 7.21 plots the free surface displacement of Case 4.2.A through 4.2.C. It can be seen in this figure that the free surface bounces up and down following the air pocket rising. Figure 7.22 plots the pressure history of the domain bottom. It shows that the pressure head keeps dropping in the rising motion. This is as expected because the compressed air pocket acts like an air cushion that absorbs pressure spikes from the pressurized main pipe, releasing them at the manholes.

www.manaraa.com

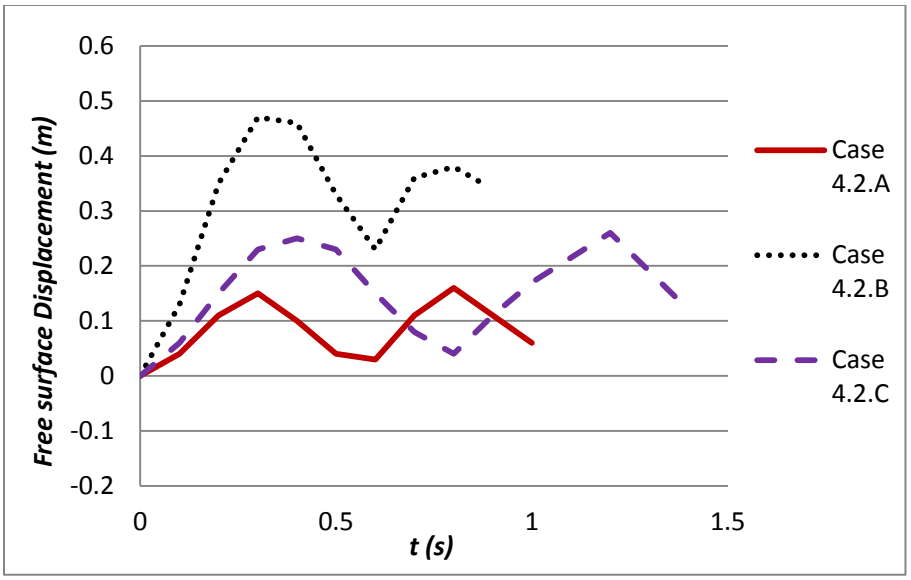

Figure 7. 21 Small size air pocket: free surface displacements of case 4.2.A, 4.2.B and 4.2.C.

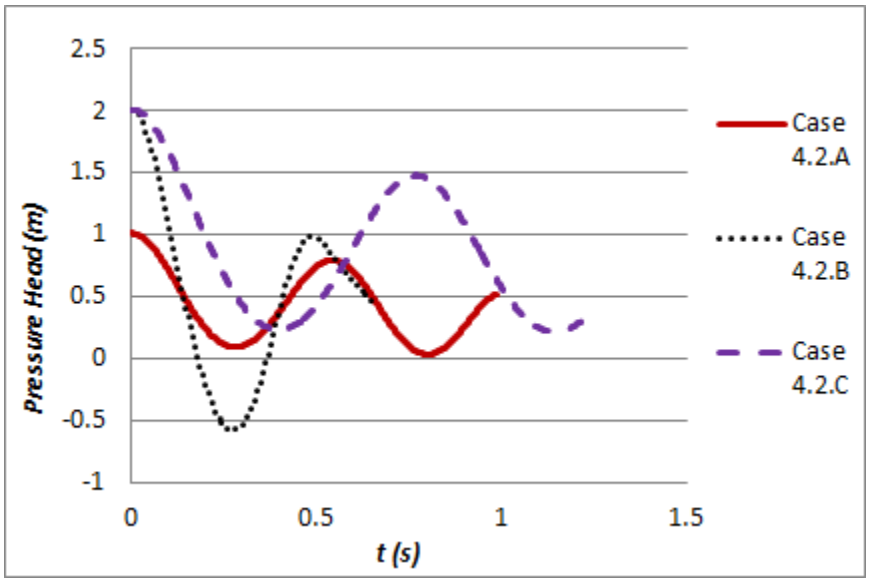

Figure 7. 22 Small size air pocket: pressure head history at riser bottom of case 4.2.A, 4.2.B and 4.2.C.

www.manaraa.com

7.4.3.Large Size Air Pocket

The simulation in this section is along the same line as the small air pocket rising tests in Section 7.4.2, but with a much larger air pocket. The pressure value at the inflow boundary also changes as the air pocket expands or contracts. Air compressibility is also counted by applying the ideal gas law to solve for a reference pressure in the same way as in section 7.4.2.

In this section, it assumes that the tail of the air pocket is still contained in the main pipe. The volume of the air pocket initially contained in the main pipe is assumed to be *1.0* m^3 or *2.0* m^3 depending on the case simulated, which is approximately *20* or *40* times of the air pocket volume in the riser, respectively. The air pocket volume is calculated from Eq. 7.2. A reference pressure is calculated from the ideal gas law (Eq. 7.1). The calculated pressure is then applied at the pressure inflow boundary and used as a reference pressure. In this way, even inflow can enter the manhole; the air pocket is still a close system without extra mass being added. The air pocket volume portion within the manhole can vary based on the pressure values at the inflow boundary.

Four cases are simulated in this section, as shown in Table 7.6. Table 7.6 also lists the initial conditions and other numerical parameters used in these simulations.

The differences between these cases are the initial pressure within the air pocket, total air pocket volume and initial water column depth. Case 4.3.A is the base case used as a baseline for comparison. Case 4.3.B contains an initial pressure that is twice as high as in Case 4.3.A. Case 4.3.B is to study the relation between geyser strength and the initial pressurization state in the main pipe. Case 4.3.C contains a total air pocket volume of *2.0* m^3, which is twice as large as in Case 4.3.A. Case 4.3.C is to more closely investigate the effects of the air pocket size on the geyser strength. Case 4.3.D contains a water column that is twice as tall as in Case 4.3.A. Case 4.3.D is to investigate geyser strength and the initial surcharged state of the manhole.

www.manaraa.com

Table 7. 6 Simulation parameters and results in large size air pocket simulation

Case Name	Case 4.3.A	Case 4.3.B	Case 4.3.C	Case 4.3.D
Boundary condition	*Pressure inflow – varied value*	*Pressure inflow – varied value*	*Pressure inflow – varied value*	*Pressure inflow – varied value*
Grid Size	20x160	20x160	20x160	20x320
Domain Size *(L x H) (m)*	0.1 x 4.0	0.1 x 4.0	0.1 x 4.0	0.1 x 8.0
Time Step Size (*s*)	5x10-5	5x10-5	5x10-5	5x10-5
Omega in SOR	1.9	1.9	1.9	1.95
Shumann Filter beta Value	1000	1000	1000	1000
Water Column Height H_w *(m)*	0.5	0.5	0.5	1
Initial Air Void Height H_A *(m)*	0.5	0.5	0.5	0.5
Initial Air Pocket Volume in Main Pipe (m^3)	1.0	1.0	1.0	1.0
Initial Total Air Pocket Volume (m^3)	1.05	1.05	2.05	1.05
Initial Pressure Head within Air Void P_0 *(m)*	1.0	2.0	1.0	2.0
Initial Free Surface Location (*m*)	1.0	1.0	1.0	1.5
Time at breakthrough (*s*)	0.75	0.425	0.625	1.0
Free Surface Height at break through (*m*) - y_{fs}	2.2	3.2	2.92	4.0
Free Surface Displacement at break through (*m*) - D_{fs}	1.2	2.2	1.92	2.5
Free Surface Velocity at breakthrough (*m/s*)	2.5	10.8	7.2	3.2
Free Surface Height at break through normalized by the initial pressure head - y^*_{fs}	2.2	1.6	2.92	2.0
Free Surface Displacement at break through normalized by the initial pressure head - D^*_{fs}	1.2	1.1	1.92	1.25

Table 7.6 summarizes the numerical results in the large size air pocket rising simulations. Figures 7.23 through 7.26 plot the instantaneous interfaces of Case 4.3.A through 4.3.D.

www.manaraa.com

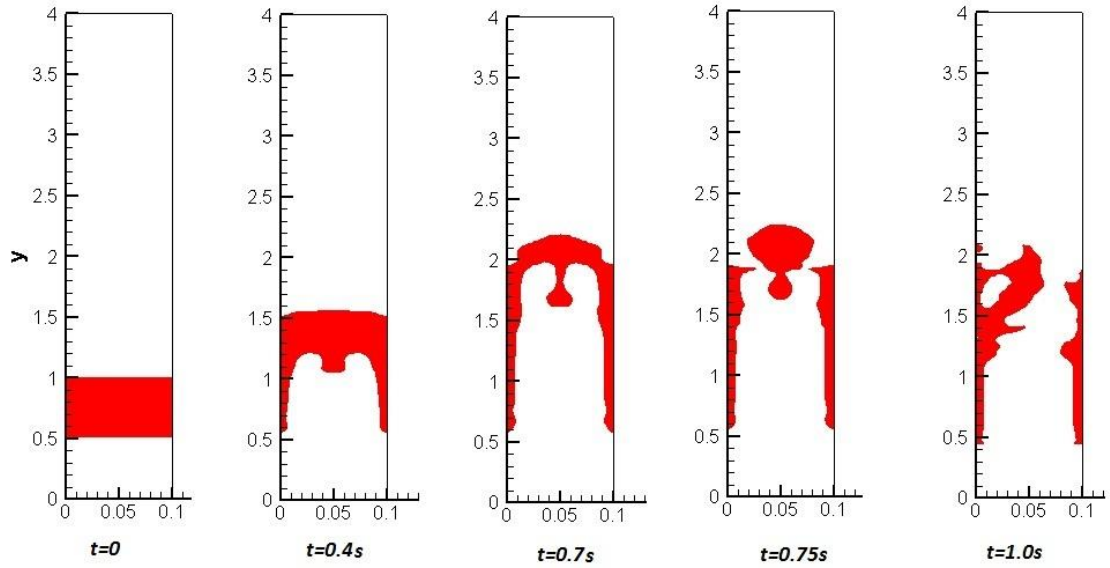

Figure 7. 23 Large size air pocket: evolution of interface of case 4.3.A.

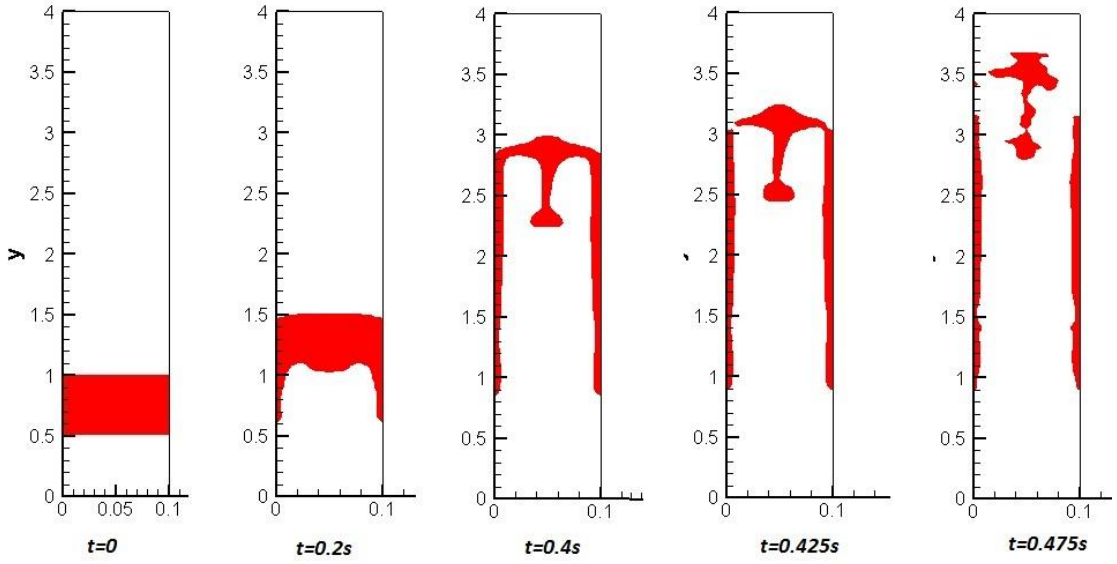

Figure 7. 24 Large size air pocket: evolution of interface of case 4.3.B.

www.manaraa.com

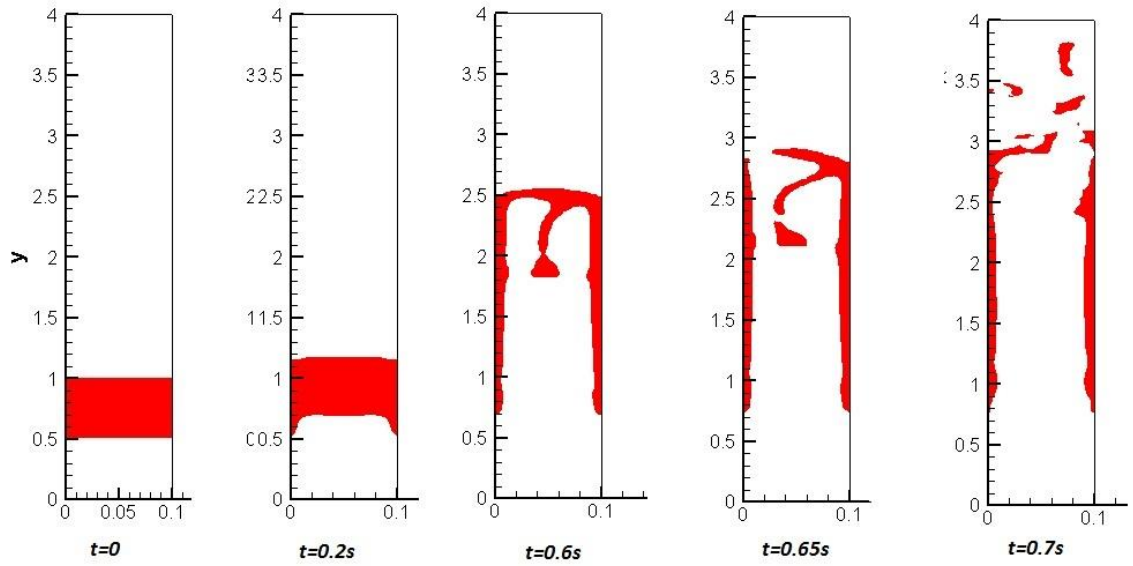

Figure 7. 25 Large size air pocket: evolution of interface of Case 4.3.C.

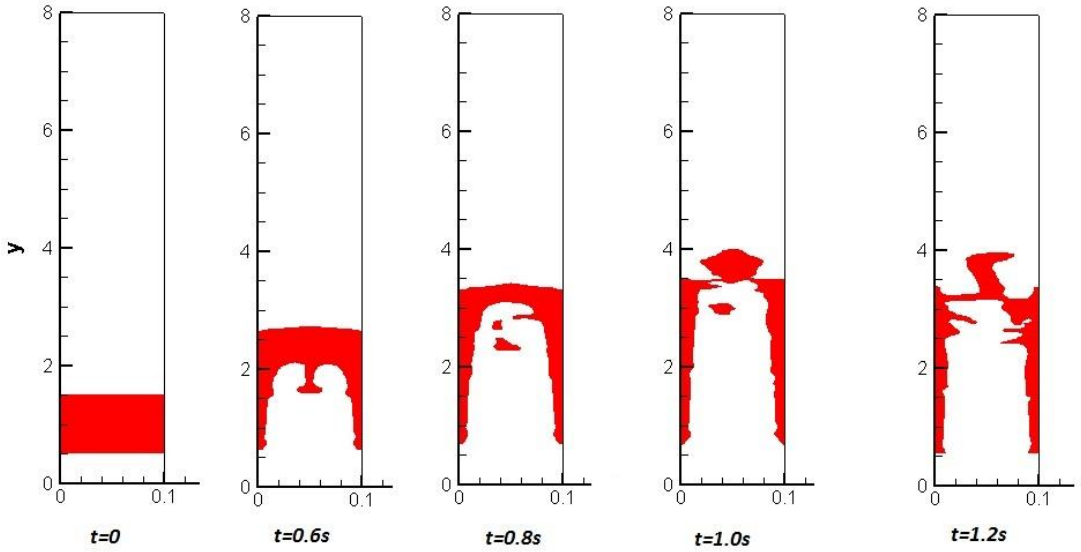

Figure 7. 26 Large size air pocket: evolution of interface of case 4.3.D.

www.manaraa.com

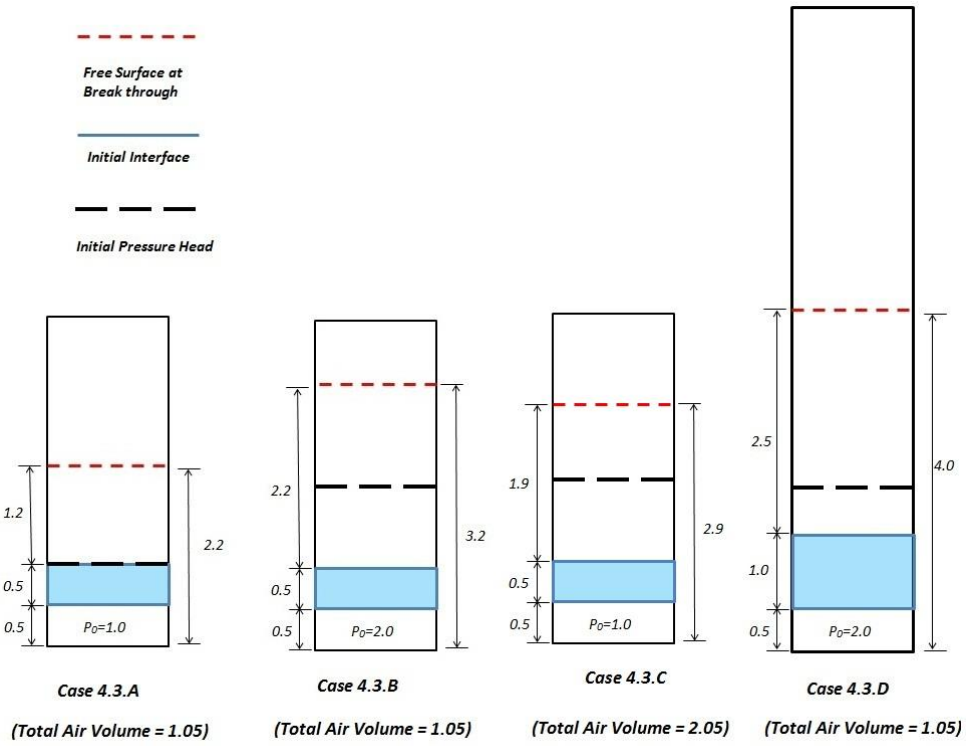

Figure 7. 27 Large size air pocket: free surface locations at breakthrough of case 4.3.A through D.

Similarly, Fig 7.27 to show the initial and final free surface locations as well as the initial pressure head within the air pocket for comparison purpose.

It can be seen from Table 7.6 and Fig. 7.27 that when the air pocket breaks through, the free surface goes up significantly with a moderate to high speed in all cases. The speed of the interface reaches as high as *10 m/s* in Case 4.3.B case when the air pocket breaks through the surface. This speed is comparable to a typical geyser jet speed. This indicates that the momentum transferred by a large size pressured air pocket from the main pipe could generate a high water air mixture jet with a significant speed. The speed of the mixture jet is related to the initial pressure in the air pocket, namely the initial pressurization state in the main pipe, as well as the total air pocket volume, as indicated by the results of Case 4.3.B and Case 4.3.C. The higher initial pressure the compressed air pocket contains; the higher free surface speed it produces. Additionally, an air pocket with a larger volume, such as in Case 4.3.C, produces a higher free surface speed.

www.manaraa.com

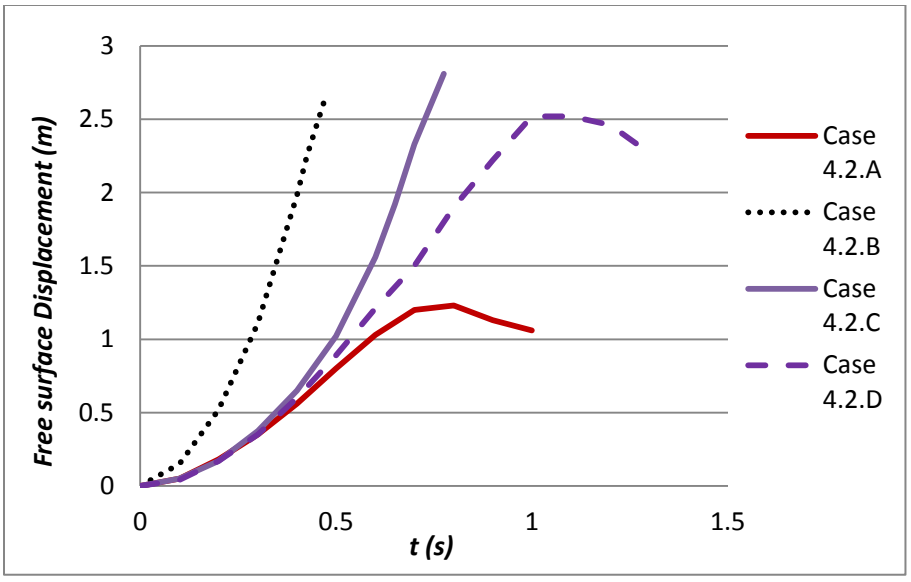

Figure 7. 28 Large size air pocket: free surface displacements of case 4.3.A through D

The geyser strength is affected by all the factors simulated in this section including the total volume of the air pocket, the initial pressure values within the air pocket and the initial water column height.

Figure 7.28 plots the free surface displacement of Case 4.3.A through 4.3.D. It can be seen in this figure that the free surface is accelerating during the whole rising process. It can also be seen from the Fig. 7.23 through 7.26 that as the air rising, there is a thin layer of film flow around the rising air pocket. The reduced water column weight further accelerates the air rising.

Figure 7.29 plots the free surface speed histories. As indicate by this figure, the free surface is accelerating initially until the breakthrough point. After the breakthrough, the free surface rising motion slows down significantly. The free surface starts breaking up and falling.

www.manaraa.com

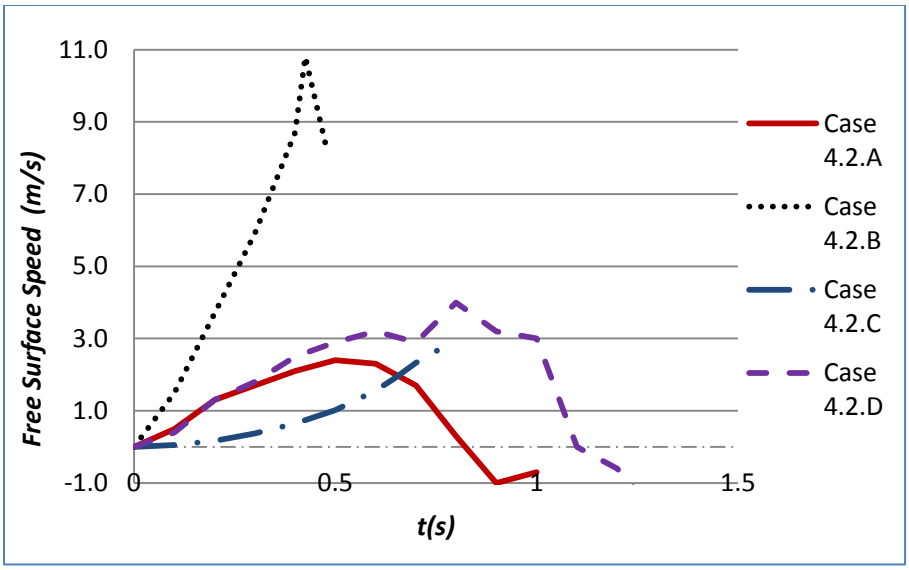

Figure 7. 29 Large size air pocket: free surface speeds of case 4.3.A through D

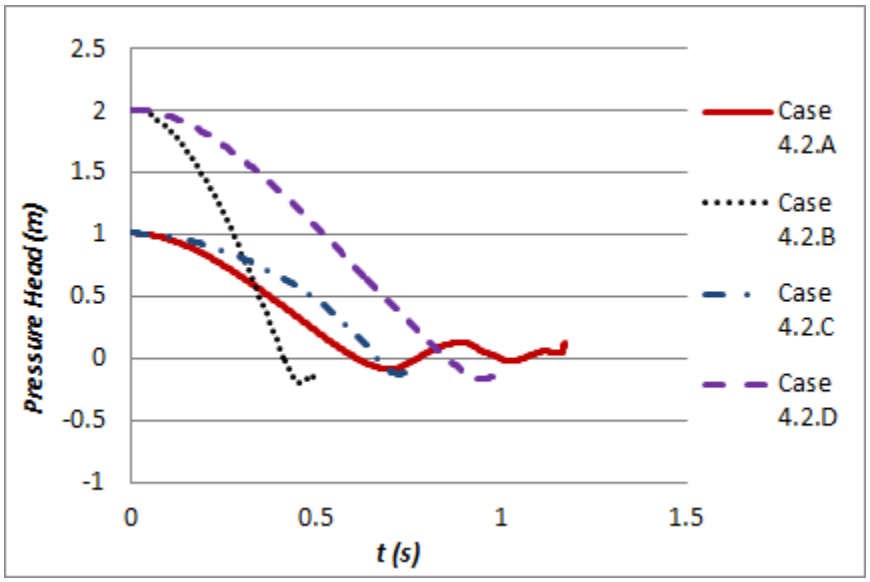

Figure 7. 30 Large size air pocket: pressure head history at riser bottom of case 4.3.A through D

Figure 7.30 plots the pressure history of the domain bottom. It shows that the pressure head keeps dropping in the air pocket rising motion until atmosphere pressure. This is as expected due to the same "air cushion" mechanism discussed in Section 7.4.2. The breakthrough also produces a brief negative pressure zone occurs right after the breakthrough due to the flow dynamics.

www.manaraa.com

7.5. Discussion

Several conclusions can be made from Section 7.1 through 7.4.

i. Buoyancy effect is a driving mechanism in air pocket rising in the vertical riser. However, this force contributes little in geyser formation and hence is not a major cause of geysers.

ii. Inertia from the main pipe system plays an important role in the air pocket rising motion, as shown in Section 7.2. The momentum transferred from the main pipe through an air pocket can lift the water column to a fairly high elevation. However, the free surface velocity in the momentum driven rising air pocket has the same magnitude as the flow velocity that enters the manhole. The free surface speed may not be large enough to form a geyser phenomenon. But if the inflow speed to the riser is extreme, it can support the geyser phenomena.

iii. Air expansion has some influence on free surface rising. However, the impacts of a compressed air pocket greatly depend on the size and the initial pressurization. A compressed air pocket with a large volume has a significant influence on the elevation and speed of the free surface. It could push the free surface to a fairly high elevation with a significantly high speed that is comparable to a geyser event. As demonstrated in Section 7.4.1, the speed of the free surface induced by a compressed air pocket released from a surcharged main pipe is significantly higher than the ones that are primarily driven by the momentum inertial. The high speed is mainly caused by a significant pressure gradient between the tail and the nose of the air pocket prior or at the time of breakthrough. Due to the low density and viscosity of the air phase, the pressure gradient produces a huge velocity near the air pocket front. If the breakthrough point is close to ground surface elevation, the mixture of water and air that poses such a high velocity can form a geyser.

iv. For air pockets with a large or infinite size (Section 7.4.1 and 7.4.3), the final free surface height at the time of breakthrough reaches an elevation that exceeds the pressure head in the main pipe. The normalized free surface height value is above one for all cases and even reached 2.9 in Case 4.3.C, which contains a large size air pocket and a higher initial pressure value. Since the normalized free surface height represents a geyser's strength and the initial pressure head in the air pocket represents the pressure from the "main" pipe. This means a geyser jet could reach a height that is higher than the pressure head in the main pipe provided that compressed air pockets arrive in the manhole. This

www.manaraa.com

observation is consistent with the observations by Lewis (2011) and Wright et al. (2009) in the field data analysis and experimental results. The field data was collected during a geyser event that occurred in Minneapolis, Minnesota on July 11, 2004 (Wright et al. 2009). The field data indicate the hydraulic grade line never approached the ground level during the geyser occurrence. The pressure head recorded by the pressure transducers within the main tunnel indicate that the pressure head within the tunnel is in the range of *5m* to *6m* when the geyser occurred, while the ground level is about *28.6* meters above than the pipe invert. They concluded that the inertial oscillation from a pressurized system is not sufficient to lift a water column above the ground to form a geyser; it is the compressed air pockets that push the water out and produce a geyser. The numerical predictions from this work confirm their observations. As shown in section 7.4.1 and 7.4.3, in which significant free surface rise has been observed, during the air pocket rising process, the air pocket expands significantly. The expanded air pocket volume, with the momentum transfer from the compressed air pocket, is shown to be able to lift the water column to a location that is higher than the pressure head.

v. The strength of the geyser is affected by several factors, including initial pressurization state in the main pipe, total volume of the air pocket and initial surcharged state in the riser. The relations between geyser strength and these factors can be summarized as:

   a. The initial pressurization plays an important role in the geyser strength. In general, a higher initial pressure in the air pocket generates a larger geyser. This trend is as expected since a compressed air pocket with higher pressure behaves like a compressed spring and "stores" more energy. The more compressed an air pocket is, the more potential it has to push the water column to a higher position.
   b. The geyser strength is also related to the initial size of the air pocket. A larger air pocket produces a higher free surface height with higher speed. Generally speaking, with the same initial pressure, the geyser strength increases as the volume of the air pocket goes up. This is consistent to what Lewis (2011) observed in his experimental results when he investigated the rising air in a vertical riser. This is because in larger sized air pockets the pressure drops at a lower rate as compared to a smaller air pocket.
   c. The time for the air pocket to break through is another factor that determines the geyser strength. A shorter breakthrough time results in a lower free surface rise under the same conditions and, consequently, a weaker geyser. This is because

www.manaraa.com

the momentum within the air pocket has not been fully transferred to the surrounding water column at time when it is released to the atmosphere.

d. The initial water column height is an important factor that determines the geyser strength. The initial water column height affects the geyser strength by determining the breakthrough time. A greater water column depth means longer distance for the air pocket to travel. Additionally, a greater water column depth means a higher water volume. As a result, it takes more time for the film flow around the rising air pocket to empty the water column that is on top of the air front. This has been demonstrated in several cases such as Case 3.C, 4.1.C and 4.3.D, which all contain a longer water column. The time at breakthrough in these cases is generally longer than the baseline cases. Consequently, the geyser strength produced by these configurations is generally higher than the ones with a shorter water column. The same timing effects have been reported by Lewis (2011) when he studied the air rising motion experimentally in a vertical riser. He concluded that increasing the reservoir level, namely, the initial water column height, increased the height of water rise.

vi. The pressure history plots in section 7.2 and 7.4 shows that the pressure within the air pocket drops as the air pocket rises and expands through the water column. The pressure drops significantly once the air pocket breakthrough. There are some similarities between the numerical result and the field measurements presented by Wright et al. (2009) when they studied the same geyser event in Minneapolis. In this geyser event, the pressure transducer recorded a pressure drop following each geyser occurrence, as shown in Figure 7.31. The rising limb of the pressure is believed to be caused by the flow transition or pressurization in the main pipe which traps air pocket in the system.

www.manaraa.com

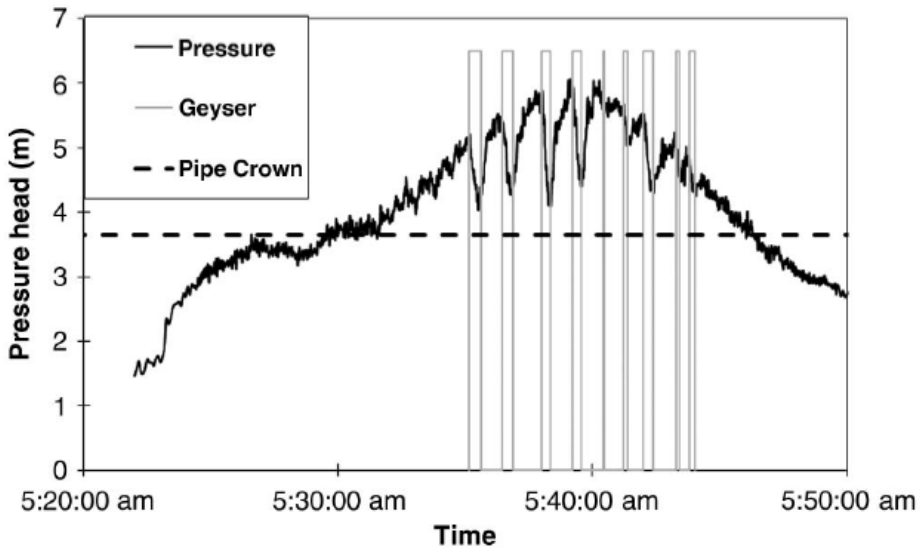

Figure 7. 31 Pressure head relative to tunnel invert in tunnel recorded during geyser events (Wright et. al. 2009)

Traditionally, the two-phase flow within the manhole has been simulated as a slug flow and the air pocket is typically treated as a Taylor bubble. A Taylor bubble has a shape similar to a bullet and almost fills the whole pipe cross section. A steady thin layer of film flow normally surrounds the Taylor bubble. However, discrepancies could arise as the flow pattern gets complicated. With the increase of the flow area and the initial pressure within the air pocket, the flow structure becomes unstable. The flow in the vertical manhole is not a slug flow but more like a churn flow, which is characterized by a mixture of water and air, as indicated by the interface evolution plots presented in this work. Collier and Thome (1951) developed a flow pattern map to describe different two–phase flow regime in a vertical tube. The flow pattern map indicates that slug flow regime only exists in the early stage of the air pocket evolution process. It turns into churn flow or annular flow regime as the air pocket rises, especially when the air breaks through the surface.

Based on the numerical observations presented in the chapter, and previous experimental findings (Vasconcelos, 2005; Wright et al. 2009 and Lewis 2011), it can be concluded that compressed air pockets with large initial volumes that are released from a surcharged main pipe is the dominant factor in a geyser formation. Other factors, such as the momentum inertial from the main pipe, also have important influence on geyser formation, but are not the dominant feature. The size of the air pocket, pressurization state in the main pipe as well as the surcharged state in the manhole can all contribute to the geyser strength.

www.manaraa.com

CHAPTER 8 CONCLUSIONS AND FUTURE WORK

8.1. Conclusions

Air pockets trapped in the stormwater system are concerns when the flow transitions from open channel flow to a pressurized flow. When the trapped air pockets are released at venting locations, such as a manhole or a dropshaft, they can cause significant instability to the system. Under the extreme conditions it could leads to a geyser, characterized by a mixture of air and water shooting out of manholes. Recent research has uncovered key factors that trigger geysers including trapped air and compressed air pockets.

The existing numerical models used to study geyser were originally developed to simulate mixed flows. The existing mixed flow models typically solve the two-dimensional Shallow Water Equation in combination with one-dimensional lumped–mass continuity and momentum equations. There are significant limitations in the existing numerical models. These limitations become more prominent when it comes to simulating the complex interactions between water and air in geyser events.

Additionally, simulation of air escape in the vertical dropshaft is greatly simplified or completely ignored in the existing models. Only a few attempts simulating the upward air pocket rising motion have been reported. However, they are fairly primitive and greatly simplify the physics since they are typically based on a one-dimensional lumped-mass conservation law.

This study attempts to bridge the gap between experimental studies and the existing mixed flow numerical models with trapped air effects. This study investigated the mechanism of geysers by numerically simulating the effects of air pockets in geyser formation, and by capturing key dynamics of the geyser features.

This research resulted in a fully dynamic two-phase flow model that is more appropriate for simulating mixed flows and geyser features. By solving the fully dynamic Navier-Stokes equations, this model is capable of handling complicated flow patterns and hydrodynamic pressures. With the implementation of an advanced two-phase flow model, Volume of Fluid, this model is capable of handling complex free surface evolution.

www.manaraa.com

The fully dynamic two-phase model developed in this work has been extensively validated from different perspectives using bench mark problems. The Navier-Stokes solver is validated in the benchmark lid-driven cavity problem. The two-phase VOF model is validated by static two-phase problems such as simple object advection, rigid object rotation test and shear flow interface deformation tests. The VOF model has been proved to be capable of tracking interface accurately as well as handling complex interface deformations. The two-phase VOF model is then tested in a dynamic environment with the velocity field being solved by the Navier-Stokes solver. This model has been validated with complicated two-phase flow problems that involve significant interface topology changes, air entrainment and violent free surface motion. The numerical results were compared with experimental data and theoretical solutions. The comparisons consistently show good performance from the model.

The numerical model is then applied to a typical stormwater system to simulate open channel flows and mixed flows. The numerical model successfully predicts the flow profile in a sloped channel. In the simulation of unsteady transient flows, the numerical model successfully predicts the location and the height of open channel bores and pressurization waves.

The two-phase model is then applied to simulate air pocket rising and release motion, key mechanisms in a geyser event. The numerical simulations explore the primary geyser driving mechanism including buoyancy, air compressibility, inertia and pressure. The numerical model demonstrates the key factors that promote a geyser feature. The numerical results show that compressed air pockets with large volume released from a surcharged main pipe are the dominant factor in a geyser formation. Other factors, such as the momentum inertial from the main pipe, also have important influence on geyser formation. The numerical model also demonstrates the key factors that contribute to geyser strength including the size of the air pocket, pressurization state in the main pipe as well as the surcharged state in the manhole. The numerical model successfully predicts the relation between the geyser strength and the key factors.

The achievement of the numerical model developed in this work can be summarized as below.

1. Simulated the violent air-water mixture flow and the complex air-water interactions in the vertical manhole using a fully dynamic two-phase model.

2. Predicted the air pocket rising and air escaping phenomenon in the vertical manhole, which are the key mechanism in a geyser occurrence.

www.manaraa.com

3. Captured the key mechanisms of the two-phase flow in the vertical manhole that has been shown experimentally, and numerically confirmed, relating the geyser strength to the dominant contributing factors in geysers.

4. Successfully simulated the mixed flows in stormwater system that involves both open channel flow and pressurized flow regimes.

8.2. Future Research

This study lays the ground work for future research when it comes to fill the gap between the existing numerical simulation and experimental understandings of geyser features. The abilities of this model can be extended or further advanced in the following ways:

1. Implement a robust turbulence model.

2. Expand to three-dimensions and/or cylindrical coordinate system to better represent the typical circular pipes in the stormwater system.

3. Use more accurate interface reconstruction approaches such as second-order least-square curve fitting.

4. Include surface tension in the Volume of Fluid two-phase model. A lot of research has been performed on including surface tension in the VOF method (Brackbill and Kothe 1996; LaFaurie et al. 1994).

5. Implement a more flexible outflow boundary condition strategy, such as the approaches used by Ziaei et al. (2007). This might make it is possible to simulate the shooting stage in geyser.

6. Create a more accurate and efficient book keeping in tracking discrete air pockets within the system to reproduce more local affects due to large air pockets separating.

www.manaraa.com

REFERENCES

Akyildiz, H E. and Unal, N. (2006). "Sloshing in a three-dimensional rectangular tank: Numerical simulation and experimental validation." Ocean Engineering, 33(16), 2135-2149.

Albertson, M. L., Andrews, J.S. (1971). "Transients caused by air release." Control of flow in closed conduits, J.P. Tullis, Ed., Colorado State Univ., Fort Collins, Colo., 315-340.

flows." J. Comput. Phys., 130, 1, 25–40.

Apittoda and Alm, Lucas (2011). "storm sewer geyser" apittoda's photostream, <http://www.flickr.com/photos/apittoda/5958358136/in/photostream>, (Jan 5, 2013).

Arai, K; Yamamoto, K.(2003). "Transient analysis of mixed free-surface-pressurized flows with modified slot model (part 1: Computational model and experiment." Proc. the 4th ASME/JSME Joint Fluids Engineering Conference, Honolulu, Hawaii, v 2, part D, 2907-2913.

Arora, M., and Roe, P. L. (1997). "On postshock oscillations due to shock capturing schemes in unsteady

Baines, W. D. (1991) "Air cavities as gravity currents on slope." J. Hydraul. Eng.,117(12),1600-1615

Batchelor, G. K. (1967). Introduction to fluid dynamics, Cambridge University Press, Cambridge, UK.

Baumbach, V., Hopfinger, E. J., and Cartellier, A. (2005). "The transient behavior of a large bubble in a vertical tube." J. Fluid Mech., 524, 131–142.

Benson, D. J. (2002). "Volume of fluid interface reconstruction methods for multi-material problems." Appl Mech Rev, 55(2), 151-165.

Book, L.D.; Boris, J.P.; Hain, K. (1975). "Flux-corrected transport II: Generalizations of the method", J. Comp. Phys., 18, 248–278.

Boris, J.P. and Book, L.D. (1973). "Flux-corrected transport I: SHASTA, a fluid transport algorithm that works." J. Comp. Phys., 11, 38–69.

www.manaraa.com

Brackbill, J.U. and Kothe, D.B. (1996). "Dynamical modeling of surface tension." NASA Conference Publication, n 3338, 693-698.

Bradford, S. and Sanders, B. (2002). "Finite-Volume Model for Shallow-Water Flooding of Arbitrary Topography." J. Hydraul Eng., 128(3), 289-298.

Braschi and Gallati (1992). "A conservative flux prediction algorithm for the explicit computation of transcritical flow in natural stream." Proc. Hydrosoft'92, Hydraulic engineering software IV: Fluid flow modeling, Computational mechanics publications, Elsevier applied science, 381-395.

Bugg, J.D., Mack, K., Rezkallah, K.S. (1998). "A numerical model of Taylor bubbles rising through stagnant liquids in vertical tubes." Int. J. Multiphase Flow 24, 271-281.

Bugg, J.D., Saad, G.A. (2002). "The velocity field around a Taylor bubble rising in a stagnant viscous fluid: numerical and experimental results." Int. J. Multiphase Flow 28, 791-803.

Capart, H. ; Sillen, X.; Zech, Y. (1997). "Numerical and experimental water transients in sewer pipes." J. Hydraul. Research, 35(5), 659-672

Cardle, J.A. and Song, C.C.S (1988). "Mathematical modeling of unsteady flow in storm sewers." Int. J. Eng. Fluid Mech., 1(4), 495-518.

Cardle, J.A., Song, C. C. S. and Yuan, M. (1989) Measurement of mixed transient flows." J. Hydraul Eng., 115 (2), 169-182

Carvalho, R.F.; Lemos, C.M.; Ramos, C.M. (2008). "Numerical computation of the flow in hydraulic jump stilling basins." J. Hydraul. Research, 46(6), 739-752

CBC News (2011). "video: Sewer geyser blasts car in Montreal storm." <http://www.cbc.ca/news/offbeat/story/2011/07/19/video-of-car-damaged-in-montreal-storm.html>, (Jan 5, 2013).

Chaiko, M.A.1 and Brinckman, K.W. (2002). "Models for analysis of water hammer in piping with entrapped air." J. Fluids Engineering, Transactions of the ASME, 124(1), 194-204.

Chaudhry, M. H. (1993). "Open channel flow." Prentice-hall, Inc., Englewood Cliffs, New Jersey, 269-276.

www.manaraa.com

Chen, S.; Johnson, D.B.; Raad, P.E.; Fadda, D. (1997). "The surface marker and micro cell method." Int. J. Numer. Meth. Fluids, 25(7), 749-778

Chorin, A. J. (1966). "Numerical Study of Thermal Convection in a Fluid Heated from Below." Ph.D. Dissertation, Department of Mathematics, New York University.

Chorin, A. J. (1967). "A Numerical Method for Solving Incompressible Viscous Flow Problems." J. Comput. Phys. 2, 12–26.

Collier, J. G. and Thome, J. R. (1996) "Convective Boiling and Condensation." Clarendon Press, Oxford, Third Edition, 11 and 16.

Cunge, J.A.; Wegner, M. (1964). "Integration numerique des equations d'ecoulement de barre de saint-venant par un schema implicite de differences finies (Numerical integration of Barre de Saint-Venant's flow equations by means of implicit scheme of finite differences)." Houille Blanche, 19(1), 33-39

Davies, R. M., and Taylor, G. I. (1950). "The mechanics of large bubbles rising through extended liquids and through liquids in tubes." Proc. R. Soc. London, Ser. A, 200(1062), 375–390.

De Martino, G.; Fontana, N.; Giugni, M. (2008). "Transient flow caused by air expulsion through an orifice." J. Hydraul. Eng., 134 (9),1395-1399.

de Sampaio, P. ; Faccini, J.L.H.; Su, J. (2008). "Modeling of stratified gas-liquid two-phase flow in horizontal circular pipes." Int. J. Heat and Mass Transfer, 51(11-12), 2752-2761

Drikakis, D. and Rider, W. (2005). "High-Resolution Methods for Incompressible and Low-Speed Flows." Springer Berlin Heidelberg , NY.

Evstigneev, N. (2008). "Integration of 3D incompressible free surface Navier-Stokes equations on unstructured tetrahedral grid using distributed computation on TCP/IP networks." WIT Transactions on Engineering Sciences, Advances in Fluid Mechanics VII, v 59, 65-77.

Fernandez-Feria, R.; Sanmiguel-Rojas, E. (2004). "An explicit projection method for solving incompressible flows driven by a pressure difference." Computers and Fluids, 33(3), 463-483.

Ferreri, G. B.; Freni, G.; Tomaselli P. (2010). "Ability of Preissmann slot scheme to simulate smooth pressurisation transient in sewers." Water Science and Technology, 62(8), 1848-1858.

www.manaraa.com

Ferziger, J.H. and Peric, M. (2001). "Computational Methods for Fluid Dynamics." Berlin, Springer; 3rd rev. edition.

Foias, C.; Manley, O.; Rosa R. and Temam, R. (2001). "Navier–Stokes Equations and Turbulence." Cambridge University Press, Cambridge.

Fuamba, M. (2002). "Contribution on transient flow modeling in storm sewers." J. Hydraul. Research, 40(6), 685-693

Fureby, C. and Grinstein, F.F. (1999). "Monotonically integrated large eddy simulation of free shear flows." AIAA, 37, 544.

Fureby, C. and Grinstein, F.F. (2002). "Large eddy simulation of high-Reynolds-number free and wall-bounded flows." J. Comput. Phys., 181, 68.

Garcia-Navarro, P.; Priestley, A.; Alcrudo, F. (1994). "Implicit method for water flow modelling in channels and pipes." J. Hydraul. Research, 32(5), 721-742

Ghia, U.; Ghia,K.N.; Shin, C.T.(1982). "High-Re Solutions for Incompressible Flow Using the Navier-Stokes Equations and a Multigrid Method." J. Comput. Phys., 48, 387–411.

Greaves, D. (2004). "Simulation of interface and free surface flows in a viscousfluid using adapting quadtree grids." Int. J. Numer. Meth. Fluids, 44, 1093–1117.

Gresho, P.M. (1991) "Some current CFD issues relevant to the incompressible Navier-Stokes equations." Computer Methods in Applied Mechanics and Engineering, 87(2-3), 201-252

Grinstein, F.F.; Guirguis R.H. (1992) "Effective viscosity in the simulation of spatially evolving shear flows with monotonic FCT models." J. Comput. Phys. 101, 165-175

Gueyffier,D; Li,J.; Nadim,A.;Scardovelli,R.;Zaleski, S. (1999). "Volume-of-Fluid Interface Tracking with Smoothed Surface Stress Methods for Three-Dimensional Flows" J. Comput. Phys. 152, 423–456.

Guignard, S; Marcer, R.; Rey, V; Kharif c.C.; Fraunié, P. (2001). "Solitary wave breaking on sloping beaches: 2-D two phase flow numerical simulation by SL-VOF method." Eur. J. Mech. B - Fluids 20, 57–74.

www.manaraa.com

Guo, Q., and Song, C. S. S. (1990). “Surging in urban storm drainage systems.” J. Hydraul. Eng., 116(12), 1523–1537.

Guo, Q., and Song, C. S. S. (1991). “Dropshaft hydrodynamics under transient conditions.” J. Hydraul. Eng., 117(8), 1042–1055.

Hamam, M. A., and McCorquodale, J. A. (1982). “Transient conditions in the transition from gravity to surcharged sewer flow.” Can. J. Civ. Eng., 9, 189–196.

Harlow F. H. and Welch, J. E. (1965). “Numerical calculation of time-dependent viscous incompressible flow of fluid with free surface.” Phys. Fluid, 8, 2182-2189

Harten, A. (1983). “High-resolution schemes for hyperbolic conservation laws.” J. Comp. Phys., 49, 357–393.

Harvie, D.J. E.; Fletcher David F., (2000). “A New Volume of Fluid Advection Algorithm: The Stream Scheme.” J. Comput. Phys., 162, 1–32.

Heywood JG, Rannacher R, Turek S. (1996). “Artificial boundaries and flux and pressure conditions for the incompressible Navier–Stokes equations.” Int J. Numer. Meth. Fluids,22, 325–52.

Hieu,P.D.; Katsutoshi, T; Ca, V.T, (2004). “Numerical simulation of breaking waves using a two-phase flow model.” Appl. Math. Modelling, 28, 983–1005

Hirt, C.W. ; Nichols, B.D.(1981). “Volume of Fluid (VOF). method for the dynamics of free boundaries.” J. Comput. Phys., 39, 201–225.

Holley, E.R. (1969). “Surging in laboratory pipeline with steady inflow ,Journal of the Hydraulics Division.” J. Hydraul. Div., 95, 961-980

Ji Zhong (1998). “General hydrodynamic model for sewer/channel network systems.” J. Hydraul. Eng., 124(3), 307-315

Jun , B.H. (1985). “Dynamic wave simulation of unsteady open channel and surcharge flows in sewer networks.” PhD. Thesis, University of Illinois at Urbana Champion, Urbana, Illinois.

Kaliakatsos, C. and Tsangaris, S., (2000). “Motion of deformable drops in pipes and channels using Navier–Stokes equations.” Int. J. Numer. Meth. Fluids, 34, 609–626.

www.manaraa.com

Kim, J. and Moin. P. (1985). “Application of a fractional step method to incompressible Navier–Stokes equations.” J. Comput. Phys., 59, 308–323.

Kioni, P. N., (2002). “Detailed flow field structure in rapid valve closure.” JSME Int. J. Series B: Fluids and Thermal Engineering, 45(3), 704-711.

Koshizuka S, Tamako H, Oka Y.(1995). “A particle method for incompressible viscous flow with fluid fragmentation.” Computational Fluid Dynamics Journal, 113,134–147.

Kothe, D.B.; Mjolsness, R.C; and Torrey, M.D. (1991). “RIPPLE: A Computer Program for Incompressible Flows with Free Surface.” Technical Report LA-12007-MS, Los Alamos National Laboratory, Los Alamos, NM.

Kothe, D.B.; Mjolsness, R.C. (1992). “RIPPLE: a new model for incompressible flows with free surfaces.” AIAA. 30 (11), 2694– 2700.

Kothe, D.B.; Rider, W.J.; Mosso, S.J. and J.S. Brock. (1996). “Volume Tracking of Interfaces Having Surface Tension in Two and Three Dimensions” AIAA Report 96-0859, Los Alamos National Laboratory, Los Alamos, NM.

LaFaurie, B.; Nardone, C.; Scardovelli, R.; Zaleski, S.; Zanetti, G., (1994). “Modeling merging and fragmentation in multiphase flows with surfer.” J. Comput. Phys., 113, 134–147.

León, Arturo S.: Ghidaoui, Mohamed S.; Schmidt, Arthur R.; García, Marcelo H. (2008) “Efficient second-order accurate shock-capturing scheme for modeling one- and two-phase water hammer flows,” J. Hydraul Eng., 134(7), 970-983,

León, Arturo S.; Ghidaoui, Mohamed S.; Schmidt, Arthur R.; García, Marcelo H. (2009) “Application of Godunov-type schemes to transient mixed flows.” J. Hydraul Eng., 47(2), 147-156

León, A. S.; Liu, X. ; Ghidaoui, M. S.; Schmidt, A ; García, M, (2010). “Junction and drop-shaft boundary conditions for modeling free-surface, pressurized, and mixed free-surface pressurized transient flows.” J. Hydraul Eng., 136(10), 705-715.

Lewis, J. W. (2011) “A Physical Investigation of Air/Water Interactions Leading to Geyser Events in Rapid Filling Pipelines.” PhD Dissertation, Department of Civil Engineering, University of Michigan.

www.manaraa.com

Li, C.W.; Zeng, C., (2010). "Flow division at a channel crossing with subcritical or supercritical flow." Int. J. Numer. Meth. Fluids; 62, 56–73.

Li, J. and McCorquodale, A. (1999). "Modeling Mixed Flow in Storm Sewers." J. Hydraul. Eng., 125(11), 1170-1180.

Lin, C.; Lee, H.; Lee, T.; Weber, L.J., (2005). "A level set characteristic Galerkin finite element method for free surface flows." Int J. Numer. Meth. Fluids, 49(5), 521-547.

Liovic, P.; Rudman, M.; Liow, J.L. (2002). "Numerical modeling of free surface flows in metallurgical vessels." Applied Mathematical Modeling, 26(2), 113-140.

Liu, X.-D., Osher, S., and Chan, T. (1994). "Weighted essentially non-oscillatory schemes." J. Comput. Phys. 115, 200.

Liu, D.; Zhou, L.; Karney, B.; Zhang, Q.; Ou, C. (2011). "Rigid-plug elastic-water model for transient pipe flow with entrapped air pocket." J. Hydraulic Research, 49(6), 799-803.

Löhner, R. ; Yang, C ; Oñate, E, (2006). "On the simulation of flows with violent free surface motion." Computer Methods in Applied Mechanics and Engineering, 195(41-43), 5597-5620.

Löhner, R. ; Yang, C ; Oñate, E. (2007). "Simulation of flows with violent free surface motion and moving objects using unstructured grids." Int J. Numer. Meth. Fluids, 53(8), 1315-1338.

Lu, W. Z.; Zhang,W. S.; Cui,C. Z.; Leung, A. Y. T. (2004). "A numerical analysis of free-surface flow in curved open channel with velocity–pressure-free-surface correction." Computational Mechanics 33, 215–224.

Lv, X.; Zou, Q.; Reeve, D. (2011). "Numerical simulation of overflow at vertical weirs using a hybrid level set/VOF method." Advances in Water Resources, 34(10), 1320-1334.

Martin J.C, Moyce W.J.(1952). "Part IV: An experimental study of the collapse of liquid columns on a rigid horizontal plane." Philosophical Transactions of the Royal Society of London; A244, 312–324.

Martin, C. S. (1976). "Entrapped air in pipelines." Proc., 2nd Int. Conf. on Pressure Surges, British Hydromechanics Research Assoc., 15-28.

www.manaraa.com

Martinez, J.-M.; Chesneau, X.; Zeghmati, B. (2006). "A new curvature technique calculation for surface tension contribution in PLIC-VOF method." Computational Mechanics, 37(2), 182-193.

Mashayek, F.; Ashgriz, N1, (1993). "Height-flux method for simulating free surface flows and interfaces." Int. J. Numer. Meth. Fluids, 17(12), 1035-1054.

McDonough, J.M. (2007). "Lectures in Computational Fluid Dynamics of Incompressible Flow: Mathematics, Algorithms and Implementations." Lecture Notes, Department of Mechanical Engineering, University of Kentucky, Lexington, KY.

McDonough, J.M. (2008). "Lectures in Computational Numerical Analysis of Partial Differential Equations." Lecture Notes, Department of Mechanical Engineering, University of Kentucky, Lexington, KY.

Meier, M.; Yadigaroglu, G.;Smith, B.L. (2002). "A novel technique for including surface tension in PLIC-VOF method." European Journal of Mechanics, B/Fluids, 21(1), 61-73

Ming, P.J.; Duan, W.Y. (2010). "Numerical simulation of sloshing in rectangular tank with VOF based on unstructured grids." J. Hydrodynamics, 22(6), 856-864

Miyashiro, H.; Yoda, H. (1983). "Analysis of hydraulic transients in tunnels with concurrent open-channel and pressurized flow." ASME, Fluids Engineering Division, 4, 73-75

Noh, W. F.; Woodward, P. (1976). "SLIC (simple line interface calculation)." Lecture Notes in Physics, Vol. 59, Springer, New York, 330–340.

Ohta, M.; Hashimoto, K.; Naito, K.; Matsuo, Y.; Sussman, M., (2012). "Numerical analysis of gas-liquid bubble flow in a horizontal rectangular channel." J. Chemical Engineering of Japan, 45(2), 102-106.

Osher, S.; Sethian, J.A. (1988). "Fronts propagating with curvature-dependent speed: algorithms based on Hamilton–Jacobi formulations." J. Comput. Phys. 79 (1), 12–49.

Queutey, P., Visonneau, M. (2007). "An interface capturing method for free-surface hydrodynamic flows." Computers & Fluids 36, 1481–1510.

Panton, R. L. (2005). "Incompressible Flow." 3rd Edition, John Wiley&Sons, Inc.

www.manaraa.com

Park, I. R.; Kim, K. S.; Kim J.; Van,S. H.(2009). "A volume-of-fluid method for incompressible free surface flows." Int. J. Numer. Meth. Fluids, 61, 1331–1362.

Pezzinga, G. (1994). "Velocity Distribution in Compound Channel Flows By Numerical Modeling." J. Hydraul Eng, 120(10), 1176-1198.

Pilliod, Jr. J.E. and Puckett, E.G. (2004). "Second-order accurate volume-of-fluid algorithms for tracking material interfaces." J. of Comp. Physics 199, 465–502.

Politano, M.; Odgaard, A. Jacob; Klecan, W. (2007). "Case study: Numerical evaluation of hydraulic transients in a combined sewer overflow tunnel system Journal of Hydraulic Engineering." 133(10), 1103-1110

Popinet, S.; Zaleski, S., (1999). "A front-tracking algorithm for accurate representation of surface tension." Int. J. for Numerical Methods in Fluids, 30(6), 775-793.

Preissmann, A. and Cunge, J.A. (1961) "Calcul du mascaret sur machine electronique (Tidal bore calculation on electronic computer)." Houille Blanche, 16(5), 588-596

Puckett, E.G.; Almgren, A.S.; Bell, J.B.; Marcus, D.L.; Rider, W.J., (1997). "A high-order projection method for tracking fluid interfaces in variable density incompressible flows." J. Comput. Phys. 130 (2), 269–282.

Rider, W.J.; Kothe, D.B. (1998). "Reconstructing volume tracking." J. Comput. Phys. 141 (2), 112–152.

Rider, W.J.; Margolin, L.G. (2003). "From numerical analysis to implicit subgrid turbulence modeling." AIAA-2003-4101, Proc.16th AIAA CFD, Orlando, FL.

Rudman, M. (1997). "Volume-Tracking Methods For Interfacial Flow Calculations." Int J. Numer. Meth. Fluids, v 24, 671–691.

Rudman, M., (1998). "A volume-tracking method for incompressible multifluid flows with large density variations." Int J. Numer. Meth. Fluids, 28(2), 357-378.

Sani, Robert L.; Shen, J.; Pironneau, O.; Gresho, P.M. (2006). "Pressure boundary condition for the time-dependent incompressible Navier-Stokes equations." Int. J. Numer. Meth. Fluids, 50(6), 673-682

www.manaraa.com

Schwarz, H. A. (1870). “Vierteljahrsschrift Naturforsch.” Ges. Zurich 15, 272- 286,

Scardovelli, R.; Zaleski, S. (2003). “Interface reconstruction with least-square fit and split Eulerian–Lagrangian advection.” Int. J. Numer. Meth. Fluids, 41,251–274

Sekavcnik, M.; Ogorevc, T.; Škerget, L. (2006). “CFD analysis of the dynamic behaviour of a pipe system.” Forschung im Ingenieurwesen/Engineering Research, 70(3), 139-144,

Shuman, F. G. (1957). “Numerical method in weather prediction: smoothing and filtering.” Mon. Weath. Rev. 85, 357–361.

Shu, C.W. and Osher,S. (1988). “Efficient implementation of essentially non-oscillatory shock capturing schemes.” J. Comp. Phys., 77, 439–471.

Shulgin, V.V. (1975). “Hydraulic shock when air is present in pipes.” Russian Engineering Journal (English translation of Vestnik Mashinostroeniya) , 55(8), 8-11.

Song, C. C.S.; Cardle, J. A.; Kim S.L. (1983). “Transient mixed-flow models for storm sewers.” J. Hydraul. Eng., 109(11),1487-1504

Stockstill, R. L. and Berger, R. C. (2009). “A Three-dimensional numerical model for flow in a lock filling system.” Proc. World Environmental and Water Resources Congress 2009, Great Rivers, 342, 2737-2746.

Sussman, M.; Smereka, P.; Osher, S. (1994). “A level set approach for computing solutions to incompressible two-phase flow.” J. Comput. Phys. 114 (1), 146-159.

Sussman, M. and Puckett, E.G. (2000). “A coupled level set and volume of fluid method for computing 3d and axisymmetric incompressible two-phase flows.” J. Comput. Phys., 162, 301–337.

Sussman, M., (2003). “A second order coupled level set and volume of fluid method for computing growth and collapse of vapor bubbles.” J. Comput. Phys. 187, 110–136.

Sussman, M.; Puckett, E.G. (2000). “A coupled level set and volume of fluid method for computing 3d and axisymmetric incompressible two-phase flows.” J. Comput. Phys. 162, 301–337.

www.manaraa.com

Tai, C.F. and Chung, J.N. (2011). “A direct numerical simulation of axisymmetric liquid-gas two-phase laminar flows in a pipe.” Int J. Numer. Meth. Fluids, 66(1), 97-122.

Ubbink O. (1997). “Numerical prediction of two fluid systems with sharp interfaces.” Ph.D. Thesis, Imperial College of Science, Technology and Medicine, London.

Valentin, F. (1981). “Continuous discharge measurement for the transition between partly filled and pressurized conduit flow in sewerage systems.” Water Sci. and Technol., 13(8), 81-97.

Vasconcelos, J. G. and Wright, S. J. (2003a). “Laboratory investigation of surges formed during rapid filling of stormwater storage tunnels.” Proc., 30th IAHR Congress, IAHR, Thessaloniki, Greece.

Vasconcelos, J. G. and Wright, S. J. (2003b). “Surges associated with air expulsion in near-horizontal pipelines”, Proc., the 4th ASME/JSME Joint Fluids Engineering Conference, Honolulu, Hawaii, USA.

Vasconcelos, J. G. (2005) “Dynamic Approach to the Description of Flow Regimes Transition in Stormwater Systems”, PhD Dissertation, Department of Civil Engineering, University of Michigan.

Vasconcelos, J. G.; S. J. Wright and P. L. Roe (2006). "Improved simulation of flow regime transition in sewers: Two-component pressure approach.” J. Hydraul. Eng., 132(6): 553-562.

Vasconcelos, J. G.; Wright, S. J.; Roe, P. L. (2009). “Numerical oscillations in pipe-filling bore predictions by shock-capturing models.” J. Hydraul. Eng., 135(4), 296-305

Wallis, G. B. (1969). “One-dimensional two-phase flow.” McGraw-Hill, New York.

Wang, K. H.; Shen, Q. and Zhang, B. X. (2003). “Modeling propagation of pressure surges with the formation of an air pocket in pipelines.”, Comput. Fluids, 32(9), 1179-1194.

Wang, C. Y.; Teng, J.T.; Huang, G. P.G. (2011). “ Numerical simulation of sloshing motion inside a two dimensional rectangular tank by level set method.” Int J. Numer. Meth. Fluids, 21(1), 5-31.

Wiggert, D. C. (1972). “Transient flow in free-surface, pressurized systems.” J. Hydraul. Div., 98(1), 11–27

www.manaraa.com

Wright, S.J. , Lewis, J.W. and Vasconcelos, J.G.,(2009). "Physical processes resulting in geyser formation in rapidly filling stormwater tunnels", Proc. of World Environmental and Water Resources Congress, ASCE, Great Rivers, 342, 5380-5389

Wright, S. J.; Lewis, J. W.;Vasconcelos, J. G. (2011a). "Physical Processes Resulting in Geysers in Rapidly Filling Storm-Water Tunnels. " J. Irrigation and Drainage Eng., 137(3), 199-202.

Wright, S. J.; Lewis, J. W.;Vasconcelos, J. G. (2011b). "Geysering in Rapidly Filling Storm-Water Tunnels. " J. Hydraul. Eng., 137(1), 112-115.

Yamada, F.; Takikawa, K. (1999). "Improving the accuracy of free-surface recognition and conservation of mass for the volume of fluid method." Proc. International Offshore and Polar Engineering Conference, 3, 643-650.

Yevjevich, V. (1975). "storm-drain network." Unsteady flow in open channel, Water Resources Publications, Littleton, Co, 669-703.

Yen, B.C. (1978). "Hydraulic instabilities of Storm sewer flows." Proc., Int. Conf. on Urban Drainage, University of Southhampton, Southhampton, U.K., 283-293.

Youngs, D.L. (1982). "Time-dependent multi-material flow with large fluid distortion." Numerical Methods for Fluid Dynamics, Academic Press, NY.

Yost, S.A. and Rao, P. (2000). "A moving boundary approach for one-dimensional free surface flows." Advances in Water Resources, 23 (4), 373-382.

Yue, W.; Lin, C. L.; Patel, V. C. (2003). "Numerical simulation of unsteady multidimensional free surface motions by level set method." Int J. Numer. Meth. Fluids, 42(8), 853-884.

Zalesak, S.T. (1979). "Fully multidimensional flux-corrected transport algorithms for fluids." J. Comput. Phys., 31, 335–362.

Zhang, Y. and Vairavamoorthy, K. (2006 a). "Transient flow in rapidly filling air-entrapped pipelines with moving boundaries" Tsinghua Science and Technology, 11(3), 313-323.

Zhang, Y. and Vairavamoorthy, K. (2006 b). "Application of method-of-lines to charging-up process in pipelines with entrapped air" Tsinghua Science and Technology, 11(3), 324-331.

www.manaraa.com

Zhang, Y.; Zou, Q.; Greaves, D. (2010). "Numerical simulation of free-surface flow using the level-set method with global mass correction." Int J. Numer. Meth. Fluids, 63(6), 651-680.

Zhou, F.; Hicks, F.E.; Steffler, P.M. (2002). "Observations of air-water interaction in a rapidly filling horizontal pipe." J. Hydraul. Eng., 128(6), 635-639

Ziaei, A. N.; McDonough, J. M.; Emdad, H. and Keshavarzi, A. R. (2007). "Using vorticity to define conditions at multiple open boundaries for simulating flow in a simplified vortex settling basin." Int. J. Numer. Meth. Fluids 54, 1–28.

www.manaraa.com

VITA

Zhiyu Shannon Shao

Zhiyu Shannon Shao was born in Guang An, Sichuan, China.

Education

M.S., Civil Engineering – University of Kentucky, Lexington, Kentucky, USA, December 2004

M.S., Municipal Engineering – Tongji University, Shanghai. China, May 2001

B.S., Water Supply and Drainage Engineering – Huazhong University of Science and Technology, Wuhan, Hubei, China, June 1992

Professional Positions

Graduate Research Assistant: University of Kentucky.

Lexington, Kentucky, USA, June 2010 – March 2013

Water Resources Engineer: Stantec Consulting Services Inc.

Lexington, Kentucky, USA, Jan. 2005 - June 2010

Graduate Research Assistant: University of Kentucky.

Lexington, Kentucky, USA, Sept. 2001 – Jan. 2004

Graduate Research Assistant: Tongji University.

Shanghai, China, Sept. 1998 - April 2001

www.manaraa.com

Project Engineer: Chengdu Municipal Engineering Design & Research Institute, Inc.

Chengdu, Sichuan, China, July 1996 – August 1998

Publications

Shao, Zhiyu; Yost, Scott, "Development of a Fully Dynamic Two-phase Numerical Model to simulate Mixed Flows in Stormwater System", Journal of Engineering Mechanics, ASCE, (in Review)

Shao, Zhiyu; Yost, Scott, "Using a Multiphase Flow Numerical Model to Simulate Geysers in Stormwater Systems," 2013 World Environmental and Water Resources Congress, ASCE, Cincinnati, OH, 20-22 May 2013.

Shao, Zhiyu; Yost, Scott, "Development of a Two-phase Numerical Model to simulate Transient Flow in Stormwater System", Journal of Hydraulic Engineering, ASCE, 2012, (In review)

Shao, Zhiyu; Yost, Scott, "Using a Multiphase Flow Numerical Model to Simulate Geysers in Stormwater Systems", Proc., World Environmental & Water Resources Congress (EWRI) ,ASCE, Cincinnati, OH, May, 2013

Long, W., Kirby, J.T., Shao, Zhiyu. , "A numerical scheme for morphological bed level calculations", Coastal Engineering, ASCE, volume 55 (2), 2008, pp. 167 – 180

Shao, Zhiyu; Yost, Scott A.; "Toward Using a 3D Numerical Model for Simulating Hydrodynamics near a Dam", Proceedings of Kentucky Water Resources Research Institute (KWRRI) Water Resources Symposium, Mar 26, 2007 Lexington, Kentucky

Shao, Zhiyu; Yost, Scott, "A High Order WENO scheme for flows with shocks and discontinuities", Proceedings of the McMat 2005 Mechanics and Materials Conference, ASCE/ASME/SES Conference on Mechanics and Materials, Barton Rouge, Louisiana, June 1-5, 2005

Shao, Zhiyu; Yost, Scott A.; Chen, Chunfang, "Parallelization of a 3-D Coast Circulation model – QUODDY", Proceedings of 2005 World Water and Environmental Resources Congress, ASCE EWRI, Anchorage, Alaska, May 15-19, 2005.

Shao, Zhiyu; Kim, Songjia; Yost, Scott, "A Portable Numerical Method for Flow with Discontinuities and Shocks", Proceedings of the 17th ASCE Engineering Mechanics Conference, Newark, Delaware, June 13-16, 2004.

Shao, Zhiyu; Yost, Scott A., "A Parallel Strategy Applied into Modified MAC to Simulate Free Surface Flow", Proceedings of 8th International Conference on International Conference of Estuarine and Coastal Modeling, ASCE, Monterey, CA, Nov 2-4, 2003.

Chen, Chunfang; Yost, Scott. A.; Shao, Zhiyu, "High Performance Programming of the 3-D Finite Element Hydrodynamic Model – QUODDY", Proceedings of the 8th International Conference of Estuarine and Coastal Modeling, ASCE, Monterey, CA, Nov 2-4, 2003

www.manaraa.com

Shao, Zhiyu; Yost, Scott A., "A Portable Numerical Method for Simulating 2D Unsteady Free-surface Flow", Proceedings of 16th ASCE Engineering Mechanics Conference, Seattle, WA, July16-18, 2003.

www.manaraa.com